Polymeric Nanoparticles for Antigen Delivery to Dendritic Cells

Dissertation to obtain the Degree of Doctor of Natural Sciences

(Dr. rer. nat.)

From the Faculty of Chemistry and Pharmacy

University of Regensburg

Presented by

Monika Stahl

from Weiden i. d. Opf.

August 2022

Monika Stahl

Polymeric Nanoparticles for Antigen Delivery to Dendritic Cells

Polymeric Nanoparticles for Antigen Delivery to Dendritic Cells

Dissertation to obtain the Degree of Doctor of Natural Sciences
(Dr. rer. nat.)
From the Faculty of Chemistry and Pharmacy
University of Regensburg

Presented by

Monika Stahl

from Weiden i. d. Opf.

August 2022

This work was carried out from January 2018 until August 2022 at the Department of Pharmaceutical Technology of the University of Regensburg.

The thesis was prepared under supervision of Prof. Dr. Achim Göpferich.

To my dear ones

Der traurigste Aspekt derzeit ist, dass die Wissenschaft schneller Wissen sammelt, als die Gesellschaft Weisheit.

Isaac Asimov (1920–1992)

Table of contents

Chapter 1

General Introduction

1 Nanoparticles as vaccine carriers
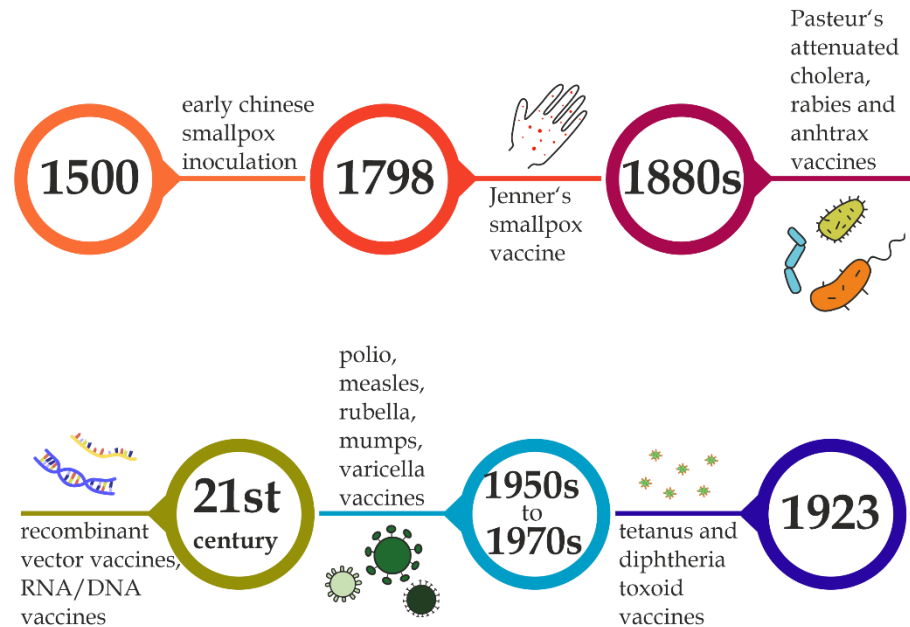
1.1 Vaccines – from then to now

Figure 1. History of vaccines [5–8].

Vaccines and vaccination have a long history. As outlined in Figure 1, a form of vaccination was practiced in China as early as around 1500 [1]. However, the breakthrough in vaccination came in the late 18th century with Jenner's discovery that cowpox could be used to vaccinate against smallpox [2]. A second milestone in vaccine history was Louis Pasteur's success in inactivating various pathogens [3, 4]. Since then, there have been many further advances and discoveries in the field of vaccination, with the main achievements shown in Figure 1 [5–8].

Vaccines are defined as 'a biological product that can be used to safely induce an immune response that confers protection against infection and/or disease on subsequent exposure to the pathogen' [7] or, more simply, 'a biological preparation that improves immunity to a particular disease' [9].

Although nowadays vaccination is taken for granted and is part of our daily life, we must not forget the many benefits that vaccines bring and have brought us. The most important ones are the health benefits. First, morbidity and mortality related to infectious diseases can be controlled and reduced [9]. For example, the incidences of measles, mumps, rubella or polio which were the main causes of morbidity and

mortality in the early 20th century, decreased by over 90% from before vaccination to 2017 [10]. Additionally, vaccination prevent 6 million deaths per year [11]. Second, with inoculation, smallpox has been eradicated [8], polio has been nearly eradicated [12], and many other diseases like measles, rubella, mumps and maternal and neonatal tetanus have been regionally eliminated or nearly eliminated [13–18]. The third important point is the generation of herd immunity, which means that by vaccinating a sufficiently high number of people, the transmission of a pathogen can be stopped. Thereby, high-risk individuals who cannot be vaccinated because they are too young, too vulnerable, or immunosuppressed can be protected [8]. Prevention of cancer and antibiotic resistance are also health benefits of vaccination. For example, the human papilloma virus (HPV) vaccine protects against infection with HPV, which can cause cervical cancer [8]. Other vaccines against bacteria prevent people from bacterial infections in the first instance, thus eliminating the need for antibiotics and the associated risk of antibiotic resistance [19, 20].

In addition to health benefits, vaccination offers economic benefits. For example, healthcare costs are lower [21], because fewer medical tests, procedures and treatments are required [22]. Furthermore, productivity gains can be achieved as workers take fewer sick days and more children reach adulthood, resulting in a larger workforce [23]. Moreover, workers or their children who must be cared for in case of illness are no longer ill or not for as long, resulting in less loss of pay for the workers [8].

Finally, we come to the social benefits of vaccination. In developing countries, for example, vaccination programs are often the initiator for the development of a social care infrastructure [24]. Additionally, people in these countries are more affected by infectious diseases due to worse access to health care compared to industrialized countries. Here, vaccines can indirectly reduce this inequity in health system by reducing the diseases [25]. Moreover, vaccination affects our life opportunities since pretravel vaccinations enable us to travel around the world without the risk of infection with a foreign pathogen [26]. It also increases our quality of life as poverty, illness and mortality are no longer life determinants [8].

To date, only vaccinations against various pathogens have been approved. However, there is also the possibility of vaccinating against cancer and autoimmune diseases. A majority of current vaccine researchers are working on this topic and developments are progressing rapidly. This field offers incredible potential in the fight against these two devastating disease areas. [6, 27]

Vaccines can be classified in different types (Table 2). It can be distinguished between live and non-live vaccines. Live vaccines contain an attenuated but replicating pathogen and non-live vaccines contain the killed or inactivated pathogen or components of it. The live attenuated microorganisms belong to the live vaccines, while killed whole organism and subunit vaccines are attributed to the non-live vaccines. Vector vaccines and nucleic acid vaccines can be categorized between live and non-live vaccines because on the one hand they are apathogenic but on the other hand some of the vector vaccines can replicate in the body and the nucleic acid vaccines contain replicating parts such as DNA/RNA. [7, 9, 28]

Live attenuated microorganism	
Killed whole organism	
Subunit	
Inactivated toxins	
(Recombinant) proteins and peptides	
Polysaccharides and Protein-polysaccharide conjugates	
Virus-like particles	
Nanoparticles	
Outer membrane vesicles	
(Recombinant) vector	
Nucleic acid (DNA/RNA)	
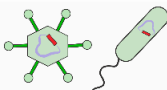
Figure 2. Types of vaccines [7, 9, 28].

Chapter 1: General Introduction

Generally, vaccines consist of two components: the antigen, which can be a protein, peptide, polysaccharide or DNA/RNA encoding for the antigen, and the adjuvant, which can be materials such as alum or nanoparticles (NPs), parts of the outer membrane of pathogens, small molecules or even DNA/RNA [29]. The antigens and adjuvants can be either naturally present in the microorganism as in live-attenuated microorganisms or killed whole organisms, or synthetically combined, as in subunit, vector or nucleic acid vaccines [30].

Adjuvants are used in vaccines to enhance the immune response against the antigen [31]. The greatest benefits of adjuvants are the ability to use lower antigen doses [32], overcoming immune senescence in elderly [33] and allowing a reduced number of vaccine doses to achieve adequate immunization [34]. Currently only alum, oil-in-water emulsions, monophosphoryl lipid A (MPL), CpG oligonucleotides and virosomes are approved as adjuvants. However, many others like nanoparticles, liposomes and various pattern recognition receptor (PRR) agonists such as toll like receptor (TLR) agonists are under development or in clinical trials [30, 35]. Several mechanisms of action of adjuvants are known: 1) formation of a depot, 2) upregulation of chemokines and cytokines, 3) targeting of antigens to antigen presenting cells (APCs), 4) enhancement of antigen uptake in APCs, 5) induction of APC maturation and 6) activation of inflammasomes [36, 37]. However, most adjuvants do not act by one specific mechanism but rather by a combination of multiple mechanisms [36]. Adjuvants can be classified into first generation adjuvants, such as alum or oil-in-water emulsions [27], which act mainly *via* their particulate character, and new generation adjuvants which are mostly immunomodulatory molecules like PRR agonists or a combination of particulate formulation and immunomodulatory molecule such as NPs and liposomes with integrated PRR agonists [30].

Most of the currently used vaccines typically induce a B cell response with a supportive CD4$^+$ T helper cell response, leading to the production of antibodies, that, somewhat simplified, are responsible for preventing infection [7]. Some vaccines such as vector vaccines and nucleic acid vaccines can induce a CD4$^+$ and CD8$^+$ T cell response [6]. To put it simply again, cytotoxic CD8$^+$ T cells are required to control and clear an established infection [7]. Additionally, most vaccines induce immune memory, which enables the immune system to react more quickly and more robustly to reinfection with the pathogen [7].

1.2   Advantages of NP vaccines over classic vaccines

The majority of the classic und most commonly used vaccines are killed whole organisms, live attenuated microorganisms, or subunit vaccines such as split vaccines and (recombinant) proteins [38–41]. Although they are well established, approved, considered safe and have been used for a long time, they provide several disadvantages shown in Table 1.

Table 1. Disadvantages of classic vaccines.

Type of vaccine	Disadvantage	Ref.
Live attenuated microorganism	Risk of uncontrolled replication in immunocompromised people → side effects	[7]
	Complex pathogenic components → poorly characterized	[21]
	Limited applicability → too high virulence of some pathogens	[42]
Killed whole organism	Incomplete inactivation → field outbreaks	[28]
	Low immunogenicity	[43]
	Foreign proteins from generation process (in eggs, tissue culture, culture medium) → side effects	[28]
	Complex pathogenic components → poorly characterized	[21]
	Induction of antibody and T helper cell response → lack of cytotoxic T cell response	[44]
Subunit vaccines (split vaccines, (recombinant) proteins)	Low immunogenicity and short immune responses → need for adjuvants	[45]
	Problems with approved adjuvants: - Non-degradable and toxic paraffin oil in Freund's adjuvant - Local inflammation with alum	[46]
	Induction of antibody and T helper cell response → lack of cytotoxic T cell response	[44]
	Degradation of antigen before reaching target site	[47]

In contrast, NPs offer many advantages compared to traditional vaccines.

While the author is aware that actually all vaccines fall under the term 'nanoparticles' due to their size, in this work, the term 'nanoparticles' refers to synthetically produced nanoparticles. It is also known that synthetically produced nanoparticles such as lipid nanoparticles are often used as carrier systems for nucleic acid vaccines. Here the author's classification is based on the part that is responsible for the immunization. If the RNA/DNA encodes the antigen, they are assigned to the nucleic acids vaccines, if RNA/DNA is implemented as an adjuvant in a nanoparticle, they are assigned to the nanoparticles.

A decisive advantage of NPs over classic vaccines is that they can evoke both cellular and humoral immune responses [48, 49]. For induction of a humoral immune response with antibody production, NPs can directly interact with and activate B cells [50]. This direct NP-B cell interaction is promoted by various NP properties. First, antigens are usually attached to NP surface in a highly repetitive manner leading to cross-linking of B cell receptors and thus to a strong B cell activation signal [45]. In addition, the repetitive antigen structure can activate complement with subsequent engagement of CD19-21 complex, further facilitating B cell activation [51, 52]. Second, small NPs can directly reach subcapsular areas in the lymph nodes (LNs) where B cells reside, allowing B cells to interact with NP antigens in their native configuration [5]. Finally, TLR agonists can be integrated into NPs to directly activate TLRs on B cells [50].

On the other hand, NPs can also be taken up by dendritic cells (DCs), which are the most potent inducers of T cells, resulting in a cellular immune response [50]. Again, NPs offer specific characteristics that are beneficial for DC targeting. First, virus-sized NPs (< 200nm) are favored for uptake in DCs [53], and internalization can be additionally enhanced with certain targeting ligands [54]. When NPs are internalized *via* endocytosis, they end up in endo-lysosomes of DCs, which are typical major histocompatibility complex-II (MHC-II) compartments [29]. Antigens degraded in these organelles are loaded onto MHC-II molecules and presented to CD4^{+} T helper cells, thereby activating them [5]. However, NPs can also reach the so-called cross-presentation pathway, in which antigens are loaded onto MHC-I molecules, leading to the activation of cytotoxic CD8^{+} T cells. Here size, NP material and type of antigen conjugation are the defining characteristics [47, 50].

Further major advantages of NPs compared to current vaccines are that NPs protect antigens from premature degradation and increase the immunogenicity of the

antigens [27]. Antigen decomposition can be prevented by encapsulating the antigens in NPs [29]. The increase in immunogenicity can be achieved either by incorporating an adjuvant into the NPs or by the NPs acting as self-adjuvants [45]. The adjuvant properties of NPs arise from depot formation by NPs and the resulting prolonged antigen exposure to the immune system [55] and from enhanced antigen uptake in APCs which can be influenced by size, shape, surface properties such as charge and hydrophilicity/hydrophobicity, and implementation of targeting ligands [29].

Moreover, in contrast to traditional vaccines such as live-attenuated microorganisms or killed whole organisms, NPs are simple in design and therefore have a good safety profile and high production reproducibility, as well as reduced production costs [27]. Finally, the highly versatile structure of NPs offers a multitude of possibilities [48]. On the one hand, the immune response can be controlled by NP design, allowing the induction of a wide range of immune responses [55]. On the other hand, NP-based vaccines can be developed against cancer [56], autoimmune diseases [50] or drugs of abuse [27] by simply using other antigens.

1.3 Nanoparticle-based vaccines

Due to the advantages mentioned above, nanotechnology has received increased attention in vaccine research and development in recent years. As shown in Figure 3, NPs offer a wide variety of design strategies, all affecting their interaction with the immune system.
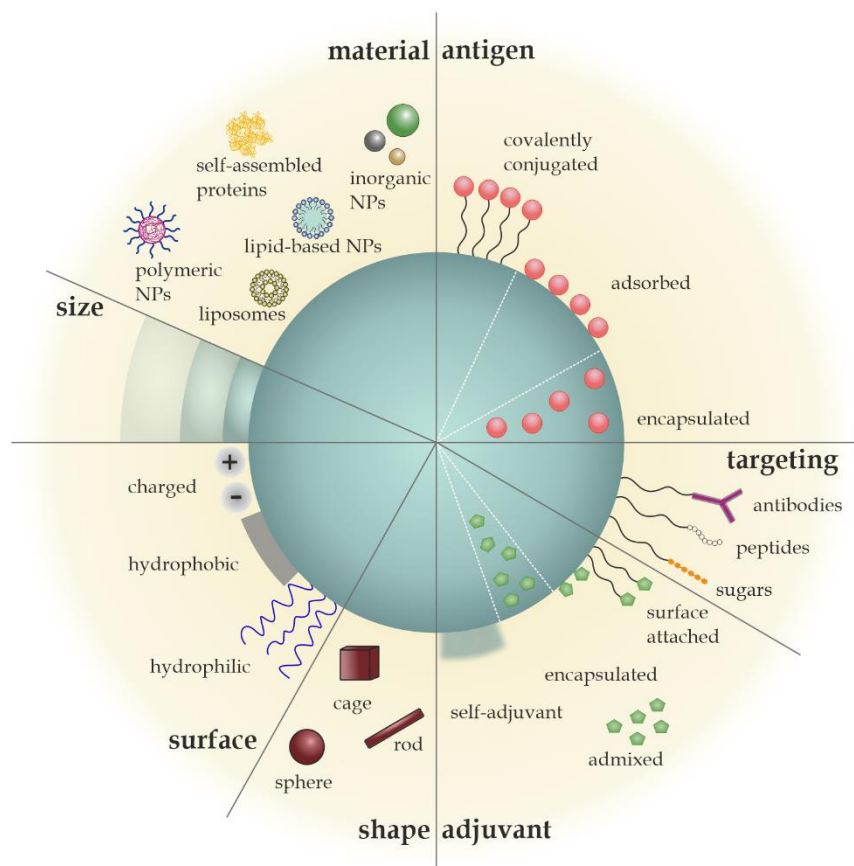
Figure 3. Design strategies of nanoparticle-based vaccines.

The types of NPs used for vaccines range from polymeric and inorganic NPs to liposomes and lipid-based NPs, each with their own pros and cons [49].

Polymeric NPs are prepared from natural polymers like alginate, inulin, pullulan, chitosan, and hyaluronic acid (HA) or synthetic polymers such as poly(lactic-co-glycolic acid) (PLGA), polylactic acid (PLA), polyglycolic acid (PGA), polyethylene glycol (PEG), polystyrene (PS), polypropylene sulfide (PPS), polyethyleneimine (PEI) and acrylic acid (AA) [46, 56]. The ease of preparation, their safety, biodegradability, biocompatibility and low cytotoxicity make the polymeric NPs very attractive for antigen delivery systems [57]. Their structure is very flexible and antigens or adjuvants can either be attached to the surface or encapsulated in the core [58]. Additionally, certain polymers offer special properties. For example, PLGA, PEI and derivatives of AA are known to enhance the cross-presentation of antigens [59–61]. Polysaccharides such as alginate, inulin, pullulan and chitosan can act as highly potent adjuvants [62]. Finally, HA and chitosan are well suited for mucosal antigen delivery as they are mucoadhesive [63, 64].

Inorganic NPs are made, among others, of gold, carbon, or silica [65]. They are not biodegradable but are very safe, biocompatible and non-toxic and have low production costs [47, 50]. Antigens and adjuvants can only be attached to the NP surface, and the structure of inorganic NPs is quite rigid [49, 56].

Finally, liposomes and lipid-based NPs are popular materials for antigen delivery platforms as they are biodegradable, biocompatible, safe, non-toxic and easy to manufacture [45, 50]. They offer a flexible structure and antigens and adjuvants can be encapsulated in the core or attached to the surface [66]. Furthermore, liposomes are able to incorporate both hydrophilic and lipophilic compounds [67].

Another point that strongly influences the immune response is the mode of antigen implementation into the NPs.

Covalent conjugation to the NP surface *via* chemical bonds or adsorption *via* charge or hydrophobicity allows binding of antigens to surface receptors on APCs [68]. Additionally, direct interaction of antigens with B cells is possible. The highly repetitive structure of antigens on the NP surface on the one hand leads to cross-linking of B cell receptors, enabling B cell activation without the need for T cell help [50], and on the other hand activates complement with engagement of CD19-21 complex further facilitating B cell activation [51, 52]. Furthermore, the repetitive antigen structure enhances NP internalization by immune cells as immunoglobulin M (IgM) binds to the surface, which activates the classical complement pathway leading to opsonization of the NPs and thus increased uptake [49, 69]. Adsorption is a relatively weak interaction between NP and antigen, where undesired desorption can occur before interaction with the immune system [47]. Covalent conjugation, in turn, represents a strong interaction since the antigen is not released until the chemical bond is degraded [56]. However, the chemical linkage can also be designed to control the immune response, as Hirosue *et al.* did by using a disulfide bond to enhance cross-presentation [70, 71].

When antigens are encapsulated within the NPs, they are protected from premature degradation by enzymes or hydrolysis, and both antigen activity and integrity are preserved [46, 47]. Encapsulation is a strong NP-antigen interaction since the antigen can only be released after degradation of the NP material [56]. This is exploited for some materials to form depots, which in turn give them adjuvant properties [72]. The mechanism is known, for example, from PLGA, where the slow degradation rate leads to sustained antigen release with subsequent enhanced immune stimulation due to prolonged antigen exposure [73].

As already mentioned in section 1.1, adjuvants are an important part of vaccines that enhance the immune response against the antigen. In the case of nanoparticulate vaccines, adjuvants can be implemented either by adsorption, covalent conjugation or encapsulation [49], the NPs can act as self-adjuvants [74], or the adjuvants can simply be admixed to the NPs [75]. Adjuvants adsorbed or covalently conjugated to the NP surface can directly interact with PRRs on the cell surface of APCs or B cells, thereby activating them [5, 29]. Encapsulated adjuvants, on the other hand, can interact with endosomal PRRs [50] and potential side effects are also reduced [49]. The self-adjuvant properties of NPs are based on depot formation, specific material properties, size-related targeting of antigens to APCs, and enhancement of antigen uptake into APCs [74].

Furthermore, targeting ligands can be integrated into the NPs. Targeting vaccines to APCs, particularly dendritic cells, is a promising tool for T cell inducing vaccines since DCs are the direct activators of T cells [50], which will be discussed in more detail in later sections of this chapter. Mannose, peptides or receptor specific antibodies against for example CD40, DEC-205 or the mannose receptor can be used to target DCs [76]. A more general targeting can be achieved with sugars that address receptors that are abundantly expressed on all APCs [45] or with immunoglobulins G (IgGs) that are recognized by macrophages [77].

The size of NPs also plays a very important role regarding the interaction of NP-based vaccines with the immune system. First, it determines, how the particles reach the LNs, which are the target organs for vaccines because B and T cells are located there [56]. NPs smaller than 200 nm can drain freely to the LNs within hours after injection and subsequently interact with the LN-resident DCs and the B cells in the B cell areas [78]. Particles larger than 200 nm are too big for direct lymphatic drainage and must therefore be internalized by local DCs, which then migrate to the lymph nodes [78]. Second, NP size affects uptake into immune cells. Generally, smaller nano-sized NPs are better internalized by APCs than lager micron-sized NPs [79]. Regarding DCs, LN-resident DCs prefer virus-sized particles between 20-200 nm, whereas the local migratory DCs can also take up lager ones (up to 2000 nm) [47].

Besides the size, the shape of NPs also influences cellular uptake. For large particles (~ 1 μm) a spherical shape was found to be better [80], while for smaller ones (~ 40 nm), rods were internalized more efficiently than spheres or cubes [81]. Furthermore, the shape of NPs can determine their intracellular localization. For example, rods are more

transported to the nucleus whereas nanosheets remain in the cytoplasm [47]. Moreover, spherical NPs induce a more potent immune response than cubes and rods [81].

Finally, surface properties such as charge and hydrophilicity/hydrophobicity can strongly impact NP interaction with the immune system. A cationic surface, for example, enhances particle uptake in APCs, likely due to interaction with the negatively charged cell membrane [82]. Additionally, cationic NPs have been shown to activate immune cells better than negative or neutral particles [47].

Compared to a hydrophilic surface, a hydrophobic one can induce a stronger immune response [83] and, similar to bacterial hydrophobic membrane domains (lipopolysaccharide (LPS) and fimbriae), can interact with TLRs, thereby activating innate immune cells [84, 85]. Hydrophobic surfaces also facilitate opsonization with immunoglobulins and lead to pentraxin binding with subsequent complement activation, both resulting in enhanced internalization by immune cells [5, 47]. On the other hand, a hydrophilic surface is attractive due to the prevention of serum protein adsorption, the faster and higher accumulation of the NPs in the lymph nodes, and the ability to induce the alternative complement pathway leading to increased cellular uptake [86–88].

Overall, the extreme versatility in structure of NPs allows for the activation of a wide variety of immunological pathways in a highly specific manner. It can be controlled whether a B cell or T cell response is induced or whether CD4^{+} or CD8^{+} T cells are activated. This tool is very important because different diseases have different protection requirements [29]. Some pathogens such as diphtheria or hepatitis B virus (HBV) simply require a strong antibody response, while others like polio and influenza need the induction of antibodies and CD8^{+} T cells to prevent the disease. Cancer, in turn, requires a combination of T helper and cytotoxic T cell response [29]. The rational design of NP-based vaccines gives us the opportunity to fill many of the gaps left by currently used vaccines.

2 Dendritic cell targeting vaccines

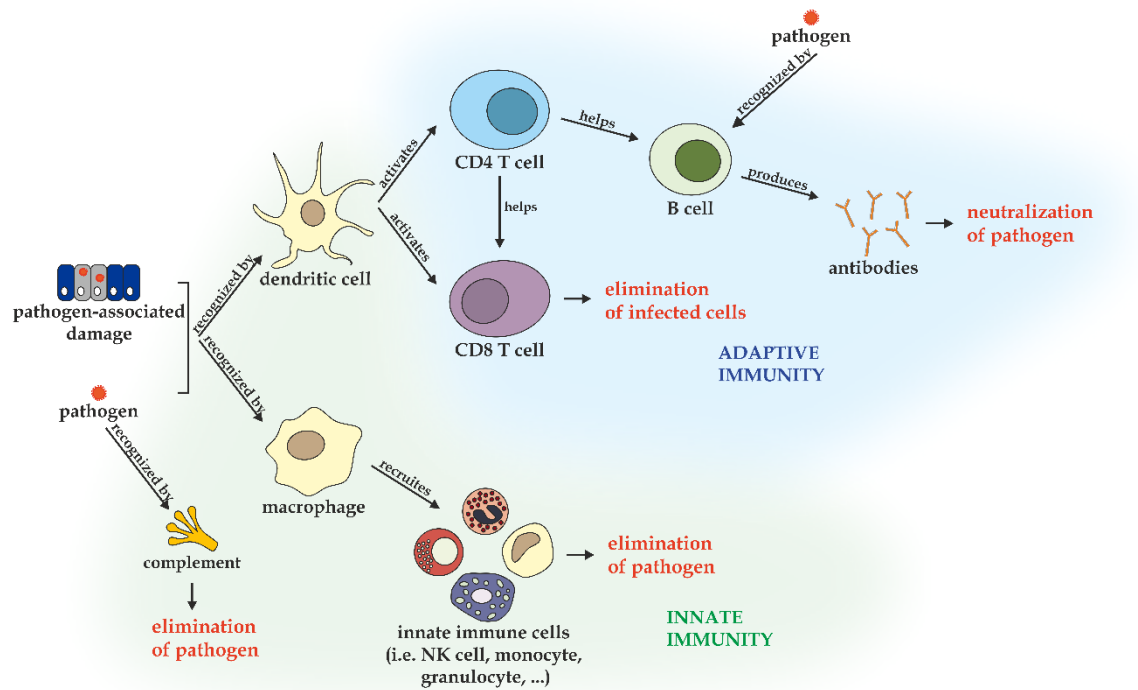## 2.1 Generation of an immune response

Figure 4. Generation of an immune response.

Our immune system is mainly responsible for protecting us against all the pathogens surrounding us. In addition, it fights cancer cells and, moreover, the proper regulation of the immune system is crucial to avoid the development of autoimmune diseases. In principle, the immune system consists of two main parts, the innate and the adaptive immune system, each comprising a variety of cells and systems responsible for different tasks. The innate immune system provides a relatively harsh and non-specific immune response against any foreign substance that enters the body. This first-line host defense includes physical barriers like skin and mucosa, cytokines, the complement system and phagocytes such as macrophages, dendritic cells, monocytes and granulocytes. The adaptive immune system, in turn, provides an acquired and specific immune response against any particular antigen that has entered the body. It enables a stronger, more specific and, through the generation of an immune memory, a faster immune response in the event of reinfection. B cells and T cells are part of the adaptive immune system. Both arms of the immune system are essential for host defense. [89–91]

Figure 4 roughly outlines what happens when a pathogen invades the body. On the one hand, the complement system recognizes the pathogen as "foreign", is thereby activated and subsequently induces various mechanisms that lead to pathogen elimination. On the other hand, macrophages and dendritic cells detect the pathogen-associated damage and the pathogen. The macrophages internalize the microorganisms or damaged cells, become activated, and then recruit other innate immune cells that kill the pathogen. Dendritic cells capture the pathogen after detecting it, migrate to the lymph nodes, and present the processed antigen to T cells, thereby activating them. Depending on their type, the activated T cells differentiate into either cytotoxic T cells or T helper cells. Cytotoxic T cells are responsible for eliminating infected cells, and T helper cells help either CD8^{+} T cells to differentiate into effector cells, or B cells, which can directly recognize and interact with free pathogens, to differentiate into antibody producing plasma cells. Antibodies bind to pathogens and thus neutralize them. [92–94]

Thus, DCs are the crucial cells that link the innate and adaptive immune system [95]. Due to their role as sentinels in the periphery, they are constantly taking up pathogens [96] through macropinocytosis, phagocytosis or endocytosis [97]. Antigen uptake leads to DC activation and initiates their migration to the lymph nodes [98]. Additionally, upon activation, DCs undergo a process called maturation. During maturation, DCs process and load the antigen onto MHC molecules, up-regulate co-stimulatory molecules, and produce cytokines. The maturation process results in presentation of antigens to T cells, thereby activating them [99]. DCs are the most effective APCs that can activate T cells and thus induce a protective and durable cellular immune response [100]. Most currently approved vaccines only induce antibody responses, resulting in a deficiency of T-cell inducing vaccines. Addressing vaccines to dendritic cells and thereby generating T-cell immunity makes it possible to close this gap [50, 101].

2.2 Potential of DC targeting vaccines

Targeting DCs greatly enhances the immunostimulatory properties of vaccines [76]. Targeted vaccines elicit an increased cellular and humoral immune response compared to non-targeted vaccines [96]. As a result, targeting allows for a reduction in the required antigen and adjuvant doses [102, 103]. The increase in immune response is mainly due to enhanced uptake of the targeted vaccines in DCs [54]. It is shown that vaccines with targeting ligands are internalized much better by the addressed cells than non-targeted

vaccines [76]. Additionally, targeting reduces the proportion of vaccine dose that ends up in other non-target cells, thereby decreasing adverse effect such as autoimmunity or cytokine release syndrome [102, 104]. Furthermore, different targeting strategies help to drive the immune response [98] as they can influence the intracellular routing of vaccines [104]. Targeted vaccines are taken up *via* receptor-mediated endocytosis, resulting in another intracellular trafficking than after uptake *via* phagocytosis or macropinocytosis. Depending on the type of internalization, the antigens end up in distinct intracellular organelles [97]. For example, pinocytosed antigens are exclusively transported to lysosomes, leading to MHC-II presentation of the antigen [105]. In contrast, phagocytosed antigens end up in phagosomes, which initially maintain a mildly acidic pH for several hours, allowing antigen export to the cytosol and subsequent cross-presentation on MHC-I molecules. After some time, the phagosomes acidify, leading to antigen degradation in the phagosomes and subsequent loading onto MHC-II. The type of presentation of phagocytosed antigens is therefore time-dependent [97, 106]. In turn, for targeted antigens that are internalized by endocytosis, the intracellular routing depends on the type of receptor being addressed. Most receptors like scavenger receptor (SR), dendritic cell-specific intercellular adhesion molecule-3-grabbing nonintegrin (DC-SIGN) and macrophage galactose-type lectin (MGL) are routed to late endosomes and lysosomes where the antigen is rapidly degraded and loaded onto MHC-II molecules [105, 107, 108]. However, other receptors such as mannose receptor (MR) and langerin route the antigen to (stable) early endosomes resulting in cross-presentation [105, 109]. Some receptors, like DEC-205 and Fc-receptor can introduce the antigen into both MHC-I and MHC-II organelles [110–112]. Thus, endocytosed antigens, like pinocytosed ones, are presented in a localization-dependent manner [97]. In addition to receptor type, the type of targeting ligand can affect intracellular trafficking. Various oxidation states of the ligand or ligands addressing different receptor binding regions can lead to distinct antigen presentation [113, 114]. Finally, since certain receptors are specifically expressed by different DC types, targeting can be used to address certain DC subsets [115]. For example, the langerin-receptor can be used to target Langerhans cells [116], whereas dendritic cell natural killer lectin group receptor-1 (DNGR-1) and X-C motif chemokine receptor 1 (XCR1) are relatively specific for murine CD8^{+} DCs, which are known to be superior in cross-presentation [117, 118]. Taken together, targeting DCs is a great tool for vaccines because of its many benefits, such as strengthening the immune response, reducing vaccine dose, decreasing side effects, and the ability to tailor the immune response.

2.3   Targeting strategies

Nanoparticles can be either actively or passively targeted to DCs. For active targeting a targeting moiety like antibody, ligand or peptide is introduced, while passive targeting can be influenced by NP size, shape and charge, or administration route [54, 102, 119]. To actively target NP vaccines to dendritic cells, mainly C-type lectin receptors (CLRs) are used as address labels [98]. Furthermore, TLRs are attractive targeting receptors, offering the advantage that the DCs are activated simultaneously to targeting, which has been shown to be crucial for inducing a robust immune response, since the lack of an activation signal during antigen delivery induces tolerance [102, 104].

Examples of CLRs popular for DC targeting are MR, DC-SIGN, langerin, DEC-205 and DNGR-1 [54]. Carbohydrates such as mannose, fucose, glucose or maltose and specific antibodies directed against the receptors are used as ligands for these receptors [76]. Using carbohydrates for targeting is attractive because they show fewer side effects and, moreover, their synthesis is based on organic chemistry, so the risk of impurities is low [76]. Antibodies, in turn, induce more effective immune responses [120]. CLRs are endocytic receptor, leading to the internalization of the targeted substances [121]. The targeting receptors are differently attractive, depending on which DC subset is to be addressed or which immune response is to be induced. The MR, also known as CD206, is expressed by DCs and macrophages but also by many other cells in the body [122]. MR has been shown to deliver the targeted antigens into stable early endosomes, resulting in cross-presentation to $CD8^+$ T cells [105]. DC-SIGN (other names: CD209, CLEC4L) was found on immature DCs, macrophages and other non-immunogenic cells such as vascular endothelial cells and atherosclerotic plaques [76]. DC-SIGN-targeting is attractive for inducing $CD4^+$ T cell responses as the antigens end up in lysosomes leading to MHC-II presentation [107]. Langerin, also known as CD207 or CLEC4K, is expressed by Langerhans cells, $CD103^+$ and $CD8^+$ DCs and [123], similar to MR, routes antigens to stable early endosomes, resulting in increased cross-presentation [109]. DEC-205 (CD205), found on DCs as well as on thymic epithelial cells [124], can be used to enhance cellular and humoral immune responses [125]. Finally, DNGR-1 (or CLEC9A) is a specific targeting receptor for murine $CD8^+$ DCs, known for their enhanced cross-priming capacity [126].

Aside from active targeting through ligand integration, NPs can also be passively targeted to specific DC types by tuning the particle size [115]. NPs smaller than 200 nm can drain directly to LNs, thereby targeting LN-resident DCs, while larger particles

(> 200 nm) remain at the injection site, thus targeting migratory DCs [78]. Moreover, administration route can be used for passive targeting [102]. After subcutaneous injection NPs either can be taken up by migratory DCs or, after drainage to the LNs, by resident DCs. Intradermal injection targets the NPs to skin DCs, and intramuscular administration results in internalization by DC subsets in skeletal muscles. Pulmonary DCs are addressed by intranasal administration while intravenous injection directs the NPs to tissue-resident DCs in spleen and lymph nodes. After intranodal application NP vaccine is captured by LN-resident DCs [102].

3 Nanoparticle design and intracellular trafficking in dendritic cells for controlling the immune response

Most of the currently approved vaccines have been developed empirically [127]. Although they protect us against many diseases, such fundamental aspects as the desired and required immune response or vaccine design were not considered during their development. Most vaccines currently in use induce the production of antibodies [128]. However, it is known that many diseases require the induction of another or an additional immune response [29]. For example, cancer requires a CD4$^+$ and CD8$^+$ T cell response, whereas HPV and diphtheria only require the induction of an antibody response for effective protection. Influenza, in turn, requires a combination of antibody response and cytotoxic T cell response [29]. These immune responses needed for protection could explain why the current vaccines help against many diseases, but not all. In particular, those requiring T cell responses are not well covered by current vaccines [129]. Here, rationally designed vaccines offer great potential for future vaccines. They allow us to control the induced immune response by exploiting the correlation between vaccine design and elicited immunity. First, vaccines can be designed to induce T cell responses [130]. Second, it is possible to create highly specialized vaccines against any disease that only induce immune responses correlating with protection and avoid unnecessary immune activation and side effects [129]. Additionally, we can prepare vaccines mimicking the immune response of a natural infection [131]. Finally, it is possible to develop vaccines against autoimmune diseases as they can also be designed to elicit an immunosuppressive and anti-inflammatory response [132].

3.1 NP design strategies

In the case of NP vaccines, a variety of design strategies have been developed to date to tailor the immune response by controlling their intracellular trafficking in DCs. First, uptake into DCs, which is the initial crucial step dictating the intracellular fate of the NPs [133, 134], can be influenced and controlled. As described above, different internalization modes lead to distinct intracellular routing. To recap, pinocytosed antigens are routed to lysosomes and thus loaded onto MHC-II molecules [105], while for phagocytosed antigens the timing matters. Early after internalization the antigens can still escape from the endosome into the cytosol und thus be loaded on MHC-I molecules. However, after phagosomal acidification, they remain in the phagosome and are presented on MHC-II to CD4^{+} T cells [97]. For endocytosed antigens, the type of receptor addressed is crucial. Some receptors end up in stable early endosomes, leading to cross-presentation, while others are routed to late endosomes or lysosomes, resulting in MHC-II presentation [104]. Overall, the uptake mechanism of the particles can therefore predetermine their intracellular trafficking [97]. Thus, by controlling the internalization mode, the intracellular routing and subsequently the immune response can be influenced. The intracellular vesicles after endocytosis are about 100-500 nm in size, while vesicles after pinocytosis and phagocytosis are in the micrometer range [133]. Therefore, by scaling the size of the NPs, the internalization mode can be influenced. Additionally, targeting ligands can be used to control the uptake pathway of the particles [104].
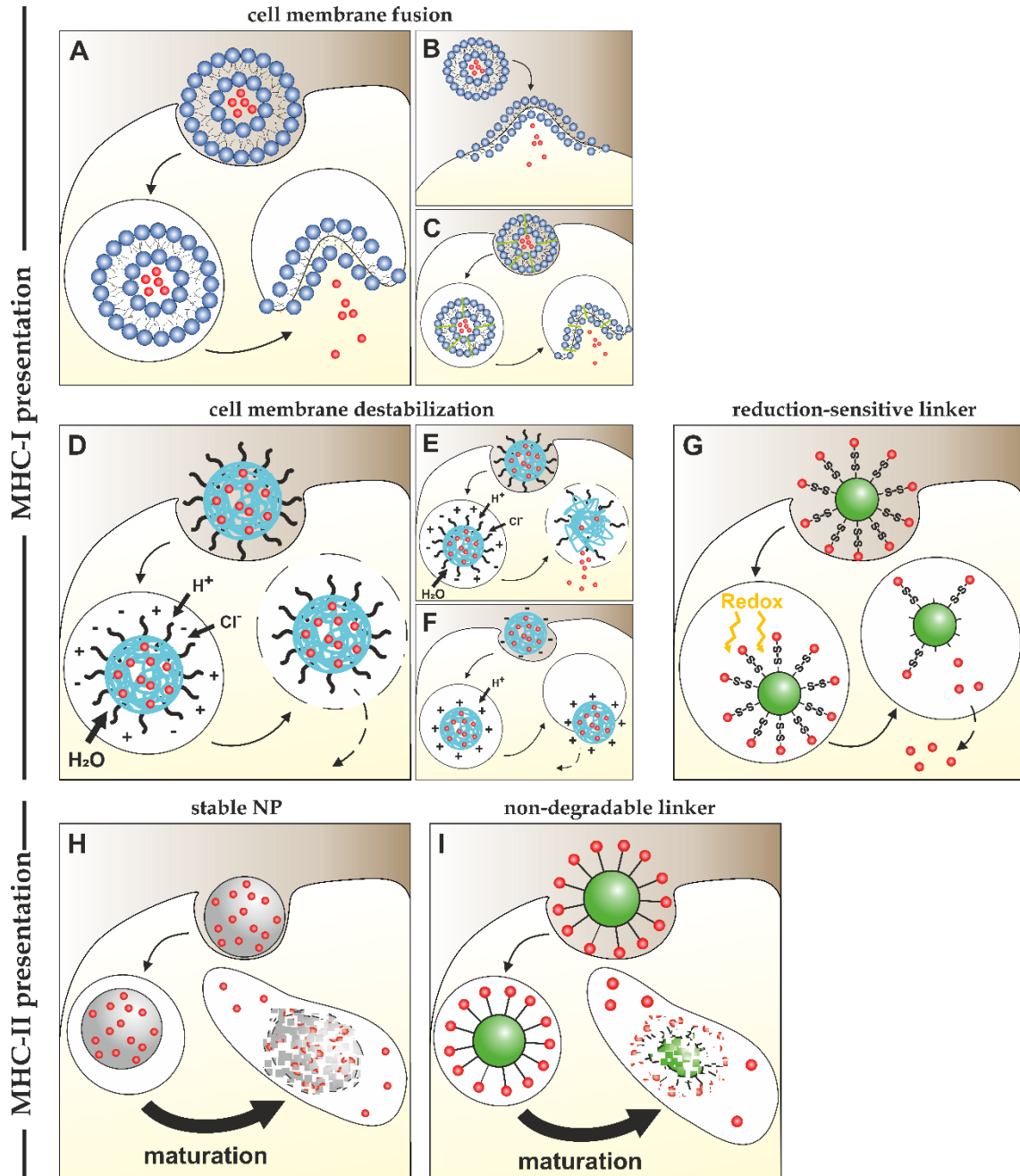
Figure 5. Controlling intracellular trafficking using different design strategies.

Furthermore, various design strategies are known that directly affect the intracellular fate of the NPs (Figure 5). They can be divided into systems leading to cross-presentation and approaches resulting in MHC-II presentation to CD4$^+$ T cells. Antigen presentation on MHC-I molecules can be achieved by inducing cell membrane fusion or cell membrane destabilization, or by using reduction-sensitive linkers for antigen coupling. Cell membrane fusion is a known mechanism for liposomes and lipid-based NPs. The

cationic lipid membrane of the particles either fuses with the anionic endosomal membrane after internalization (Figure 5A) [135] or with the anionic cell membrane during uptake (Figure 5B) [136]. Both lead to antigen release in the cytosol and subsequent processing by the proteasome, resulting in cross-presentation. Additionally, liposomes can be modified with fusogenic polymer [137] or cell-penetrating peptide [138], both of which further facilitate membrane fusion, resulting in an increased MHC-I pathway (Figure 5C). The so-called proton sponge effect is the best-known mechanism for membrane destabilization. It is known for pH responsive materials like PLGA and PEI [60, 139, 140]. These substances are negatively charged at physiological pH. This enables them to buffer the endosomal acidification by taking up the influxing protons. The counterions pumped into the endosome increase the osmotic pressure, leading to the influx of water, which in turn results in the rupture of endosomal membrane and the release of the contents into the cytoplasm (Figure 5D) [141, 142]. For polymer NPs it is known that the dissolution of the NPs into polymer chains further enhances the osmotic pressure (Figure 5E) [143]. The same is known for acid-degradable materials where the degradation products increase osmotic pressure [144, 145]. For PLGA NPs an additional mechanism is reported: protonation during endosomal acidification can result in a reversal of the particle charge from negative to positive. This in turn allows interaction with the negative endosomal membrane and thus endosomal escape (Figure 5F) [146]. NPs based on endosomolytic polymers composed of acrylic acid derivatives conjugated with cationic polyacrylates show a kind of hybrid mechanism of endosomal fusion and proton sponge. The acrylic acid moiety is negatively charged at physiological pH. During endosomal acidification, it is protonated, leading to the polymer changing from a hydrophilic polyampholyte to a hydrophobic polycation that can fuse with the endosomal membrane [147–149]. Finally, antigen conjugation *via* a reduction-sensitive bond can allow endosomal escape of the antigen. That has been shown for OVA coupled to PPS NPs *via* a disulfide bond. The antigen was released by disulfide reduction in the early endosome. Since substances with molecular weight below 50 kDa are easily exported from the endosome [100], OVA could escape into the cytoplasm (Figure 5G), be subsequently degraded by the proteasome and finally cross-presented to CD8^{+} T cells [70, 150, 151].

For MHC-II presentation to CD4^{+} T cells, the antigen can either be encapsulated in stable NPs or conjugated to the particle surface *via* a non-degradable linker. Antigens encapsulated in acid-resistant NPs are protected from release in the early endosome with subsequent endosomal escape because the particles cannot be degraded. The NPs are

therefore routed to late endosomes and lysosomes having a harsh microenvironment. NPs are degraded within the organelles, the antigens are released (Figure 5H), processed, and finally loaded onto MHC-II molecules [150–153]. Antigen conjugation to the particle surface *via* a non-degradable linker also prevents antigen release in the early endosome. The NPs end up in lysosomes (Figure 5I) where the antigen is processed, resulting in MHC-II presentation [70].

3.2   Exploitation of protease cathepsin S to control the immune response

As described above, many strategies are known that exploit the microenvironments of endosomes or lysosomes to control the intracellular trafficking of NP vaccines in DCs and hence their immune response. Besides the endosomal acidification or the reductive environment, there are also many enzymes in the subcellular DC organelles that can be used to control the intracellular fate of vaccines. For example esterases, reductases such as lysosomal thiol reductase and proteases like various cathepsins or asparagine endopeptidase were found in DCs [100]. Especially in endosomes, however, only certain enzymes can be active since the pH is maintained at 7-7.5 for at least 3 h after internalization due to low V-ATPase levels and high activity of NADPH oxidase [100, 154, 155]. One of them is cathepsin S (CatS). CatS has its best activity at pH 7.5 and is therefore the major protease active in the early endosomes/phagosomes of DCs [100, 155, 156]. In addition, CatS also plays an important role in the TAP-independent vacuolar cross-presentation pathway, as it can generate the correct class-I-presented peptides, along with few other enzymes [156]. Additionally, CatS contributes to MHC-II presentation as it controls the degradation of the invariant chain (Ii) [100, 157].

Due to its unique role as one of the few enzymes active in the early endosome, exploiting CatS activity offers a great tool to control the intracellular fate of NP vaccines. Molecules smaller than 50 kDa can be exported well from the early endosomes [100]. Therefore, in NP vaccines, antigens must be released from the NPs in order to escape the endosome and enter the cytosolic cross-presentation pathway. Here, for example, NPs could be designed to exploit the enzymatic activity of CatS in the early endosome to release the antigens, e.g. through particle degradation or linker cleavage, thus enabling cross-presentation. In turn, if a CatS-resistant antigen-NP connection is generated, the particles may end up in lysosomes and thus present the antigen on MHC-II.

4 Conclusion

In summary, NPs hold enormous potential as vaccine carriers. They can overcome all the disadvantages of current vaccines. Additionally, targeting vaccines to DCs enables the production of T cell inducing vaccines, which are poorly represented among currently approved vaccines. Rational vaccine design, in which vaccines are designed to elicit precisely predicted immune responses, is becoming increasingly important. Here, the NPs with their highly versatile structure, offer an incredible toolbox that can be used to control their fate in the body and in the cells and thus the immune response.

References

1. Needham J, ed. *Science and Civilisation in China: Volume 6, Biology and Biological Technology, Part 6, Medicine*. 3rd ed. Cambridge: Cambridge Univ. Press; 2008.

2. Weltgesundheitsorganisation. *Smallpox and its eradication*. Geneva; 1988.

3. Pasteur L. De l'atténuation du virus du choléra des poules. *Comptes Rendus De l'académie des sciences*. 1880: 673–680.

4. Pasteur L, Chamberland C, Roux E. Sur la vaccination charbonneuse. *Comptes Rendus De l'académie des sciences*. 1881: 1378–1383.

5. Bachmann MF, Jennings GT. Vaccine delivery: A matter of size, geometry, kinetics and molecular patterns. *Nat Rev Immunol*. 2010; 10: 787–796.

6. Plotkin SA. Vaccines: past, present and future. *Nat Med*. 2005; 11: S5-11.

7. Pollard AJ, Bijker EM. A guide to vaccinology: from basic principles to new developments. *Nat Rev Immunol*. 2021; 21: 83–100.

8. Rodrigues CMC, Plotkin SA. Impact of Vaccines; Health, Economic and Social Perspectives. *Front Microbiol*. 2020; 11: 1526.

9. Donnelly RF. Vaccine delivery systems. *Hum Vaccin Immunother*. 2017; 13: 17–18.

10. Roush SW, Murphy TV. Historical comparisons of morbidity and mortality for vaccine-preventable diseases in the United States. *JAMA*. 2007; 298: 2155–2163.

11. Ehreth J. The global value of vaccination. *Vaccine*. 2003; 21: 596–600.

12. Morales M, Tangermann RH, Wassilak SGF. Progress Toward Polio Eradication - Worldwide, 2015-2016. *MMWR Morb Mortal Wkly Rep*. 2016; 65: 470–473.

13. Shamila Sharma. Maldives, Sri Lanka eliminate measles and rubella, ahead of 2023 target. Available at https://www.who.int/southeastasia/news/detail/08-07-2020-maldives-sri-lanka-eliminate-measles-and-rubella-ahead-of-2023-target.

14. Finnish institute for health and welfare. MMR, or measles, mumps and rubella vaccine. Available at https://thl.fi/en/web/infectious-diseases-and-vaccinations/vaccines-a-to-z/mmr-or-measles-mumps-and-rubella-vaccine.

15. Peltola H, Davidkin I, Paunio M, Valle M, Leinikki P, Heinonen OP. Mumps and rubella eliminated from Finland. *JAMA*. 2000; 284: 2643–2647.

16. Cherian T, Mantel C. Nationale Impfprogramme. *Bundesgesundheitsblatt Gesundheitsforschung Gesundheitsschutz*. 2020; 63: 16–24.

17. Njuguna HN, Yusuf N, Raza AA, Ahmed B, Tohme RA. Progress Toward Maternal and Neonatal Tetanus Elimination - Worldwide, 2000-2018. *MMWR Morb Mortal Wkly Rep*. 2020; 69: 515–520.

18. World Health Organization. Eliminating measles and rubella. Available at https://www.who.int/westernpacific/activities/eliminating-measles-and-rubella.

19. Palmu AA, Jokinen J, Nieminen H, et al. Effect of pneumococcal Haemophilus influenzae protein D conjugate vaccine (PHiD-CV10) on outpatient antimicrobial purchases: a double-blind, cluster randomised phase 3–4 trial. *The Lancet Infectious Diseases*. 2014; 14: 205–212.

20. Kyaw MH, Lynfield R, Schaffner W, et al. Effect of introduction of the pneumococcal conjugate vaccine on drug-resistant Streptococcus pneumoniae. *N Engl J Med*. 2006; 354: 1455–1463.

21. Mao HH, Chao S. Advances in Vaccines. *Adv Biochem Eng Biotechnol*. 2020; 171: 155–188.

22. Largeron N, Lévy P, Wasem J, Bresse X. Role of vaccination in the sustainability of healthcare systems. *J Mark Access Health Policy*. 2015; 3.

23. Bloom DE, Canning D, Weston M. The value of vaccination. *World Economics Journal*. 2005: 15–39.

24. Shearley AE. The societal value of vaccination in developing countries. *Vaccine*. 1999; 17: S109-S112.

25. Deogaonkar R, Hutubessy R, van der Putten I, Evers S, Jit M. Systematic review of studies evaluating the broader economic impact of vaccination in low and middle income countries. *BMC Public Health*. 2012; 12: 878.

26. Andre FE, Booy R, Bock HL, et al. Vaccination greatly reduces disease, disability, death and inequity worldwide. *Bull World Health Organ*. 2008; 86: 140–146.

27. Brisse M, Vrba SM, Kirk N, Liang Y, Ly H. Emerging Concepts and Technologies in Vaccine Development. *Front Immunol*. 2020; 11: 583077.

28. Francis MJ. Recent Advances in Vaccine Technologies. *Vet Clin North Am Small Anim Pract*. 2018; 48: 231–241.

29. Lung P, Yang J, Li Q. Nanoparticle formulated vaccines: opportunities and challenges. *Nanoscale*. 2020; 12: 5746–5763.

30. Reed SG, Orr MT, Fox CB. Key roles of adjuvants in modern vaccines. *Nat Med*. 2013; 19: 1597–1608.

31. Pulendran B, S Arunachalam P, O'Hagan DT. Emerging concepts in the science of vaccine adjuvants. *Nat Rev Drug Discov*. 2021; 20: 454–475.

32. Pogostin BH, McHugh KJ. Novel Vaccine Adjuvants as Key Tools for Improving Pandemic Preparedness. *Bioengineering (Basel)*. 2021; 8.

33. Bulut O, Kilic G, Domínguez-Andrés J, Netea MG. Overcoming immune dysfunction in the elderly: trained immunity as a novel approach. *Int Immunol*. 2020; 32: 741–753.

34. Apostólico JdS, Lunardelli VAS, Coirada FC, Boscardin SB, Rosa DS. Adjuvants: Classification, Modus Operandi, and Licensing. *J Immunol Res*. 2016; 2016: 1459394.

35. Wagner R, Hildt E. Zusammensetzung und Wirkmechanismen von Adjuvanzien in zugelassenen viralen Impfstoffen. *Bundesgesundheitsblatt Gesundheitsforschung Gesundheitsschutz*. 2019; 62: 462–471.

36. Awate S, Babiuk LA, Mutwiri G. Mechanisms of action of adjuvants. *Front Immunol*. 2013; 4: 114.

37. Gregorio E de, Caproni E, Ulmer JB. Vaccine adjuvants: Mode of action. *Front Immunol*. 2013; 4: 214.

38. Kaufmann SHE. *Impfen: Grundlagen, Wirkung, Risiken*. 1st ed. München: C.H. Beck; 2021.

39. LeBlanc Z, Waterhouse P, Bally J. Plant-Based Vaccines: The Way Ahead? *Viruses*. 2020; 13.

40. U.S. Food and Drug Administration. Vaccines Licensed for Use in the United States. Available at https://www.fda.gov/vaccines-blood-biologics/vaccines/vaccines-licensed-use-united-states.

41. Paul-Ehrlich-Institut. Impfstoffe für Menschen. Available at https://www.pei.de/DE/arzneimittel/impfstoffe/impfstoffe-node.html.

42. Liu MA. Immunologic basis of vaccine vectors. *Immunity*. 2010; 33: 504–515.

43. Sanders B, Koldijk M, Schuitemaker H. Inactivated Viral Vaccines. In: Nunnally BK, Turula VE, Sitrin RD, eds. *Vaccine Analysis: Strategies, Principles, and Control*. Berlin, Heidelberg: Springer Berlin Heidelberg; 2015: 45–80.

44. Plotkin SA. Immunologic correlates of protection induced by vaccination. *Pediatr Infect Dis J*. 2001; 20: 63–75.

45. Sahdev P, Ochyl LJ, Moon JJ. Biomaterials for nanoparticle vaccine delivery systems. *Pharm Res*. 2014; 31: 2563–2582.

46. Guo S, Fu D, Utupova A, et al. Applications of polymer-based nanoparticles in vaccine field. *Nanotechnology Reviews*. 2019; 8: 143–155.

47. Pati R, Shevtsov M, Sonawane A. Nanoparticle Vaccines Against Infectious Diseases. *Front Immunol*. 2018; 9: 2224.

48. Zaheer T, Pal K, Zaheer I. Topical review on nano-vaccinology: Biochemical promises and key challenges. *Process Biochem*. 2021; 100: 237–244.

49. Chattopadhyay S, Chen J-Y, Chen H-W, Hu C-MJ. Nanoparticle Vaccines Adopting Virus-like Features for Enhanced Immune Potentiation. *Nanotheranostics*. 2017; 1: 244–260.

50. Gomes AC, Mohsen M, Bachmann MF. Harnessing Nanoparticles for Immunomodulation and Vaccines. *Vaccines (Basel)*. 2017; 5.

51. Dempsey PW, Allison ME, Akkaraju S, Goodnow CC, Fearon DT. C3d of complement as a molecular adjuvant: bridging innate and acquired immunity. *Science*. 1996; 271: 348–350.

52. Carter RH, Fearon DT. CD19: lowering the threshold for antigen receptor stimulation of B lymphocytes. *Science*. 1992; 256: 105–107.

53. Xiang SD, Scholzen A, Minigo G, et al. Pathogen recognition and development of particulate vaccines: does size matter? *Methods*. 2006; 40: 1–9.

54. Cruz LJ, Tacken PJ, Rueda F, Domingo JC, Albericio F, Figdor CG. Targeting nanoparticles to dendritic cells for immunotherapy. *Methods Enzymol*. 2012; 509: 143–163.

55. Fries CN, Curvino EJ, Chen J-L, Permar SR, Fouda GG, Collier JH. Advances in nanomaterial vaccine strategies to address infectious diseases impacting global health. *Nat Nanotechnol*. 2021; 16: 1–14.

56. Zhao L, Seth A, Wibowo N, et al. Nanoparticle vaccines. *Vaccine*. 2014; 32: 327–337.

57. Han J, Zhao D, Li D, Wang X, Jin Z, Zhao K. Polymer-Based Nanomaterials and Applications for Vaccines and Drugs. *Polymers (Basel)*. 2018; 10.

58. Pippa N, Gazouli M, Pispas S. Recent Advances and Future Perspectives in Polymer-Based Nanovaccines. *Vaccines (Basel)*. 2021; 9.

59. Shen H, Ackerman AL, Cody V, et al. Enhanced and prolonged cross-presentation following endosomal escape of exogenous antigens encapsulated in biodegradable nanoparticles. *Immunology*. 2006; 117: 78–88.

60. Chen J, Li Z, Huang H, et al. Improved antigen cross-presentation by polyethyleneimine-based nanoparticles. *Int J Nanomedicine*. 2011; 6: 77–84.

61. Flanary S, Hoffman AS, Stayton PS. Antigen delivery with poly(propylacrylic acid) conjugation enhances MHC-1 presentation and T-cell activation. *Bioconjug Chem*. 2009; 20: 241–248.

62. Garcia-Vello P, Speciale I, Chiodo F, Molinaro A, Castro C de. Carbohydrate-based adjuvants. *Drug Discov Today Technol*. 2020; 35-36: 57–68.

63. Dedloff MR, Effler CS, Holban AM, Gestal MC. Use of Biopolymers in Mucosally-Administered Vaccinations for Respiratory Disease. *Materials (Basel)*. 2019; 12.

64. Islam MA, Firdous J, Choi Y-J, Yun C-H, Cho C-S. Design and application of chitosan microspheres as oral and nasal vaccine carriers: an updated review. *Int J Nanomedicine*. 2012; 7: 6077–6093.

65. Hess KL, Medintz IL, Jewell CM. Designing inorganic nanomaterials for vaccines and immunotherapies. *Nano Today*. 2019; 27: 73–98.

66. Chatzikleanthous D, O'Hagan DT, Adamo R. Lipid-Based Nanoparticles for Delivery of Vaccine Adjuvants and Antigens: Toward Multicomponent Vaccines. *Mol Pharm*. 2021; 18: 2867–2888.

67. Mitchell MJ, Billingsley MM, Haley RM, Wechsler ME, Peppas NA, Langer R. Engineering precision nanoparticles for drug delivery. *Nat Rev Drug Discov*. 2021; 20: 101–124.

68. Taki A, Smooker P. Small Wonders-The Use of Nanoparticles for Delivering Antigen. *Vaccines (Basel)*. 2015; 3: 638–661.

69. Bottazzi B, Doni A, Garlanda C, Mantovani A. An integrated view of humoral innate immunity: pentraxins as a paradigm. *Annu Rev Immunol*. 2010; 28: 157–183.

70. Hirosue S, Kourtis IC, van der Vlies AJ, Hubbell JA, Swartz MA. Antigen delivery to dendritic cells by poly(propylene sulfide) nanoparticles with disulfide conjugated peptides: Cross-presentation and T cell activation. *Vaccine*. 2010; 28: 7897–7906.

71. van der Vlies AJ, O'Neil CP, Hasegawa U, Hammond N, Hubbell JA. Synthesis of pyridyl disulfide-functionalized nanoparticles for conjugating thiol-containing small molecules, peptides, and proteins. *Bioconjug Chem*. 2010; 21: 653–662.

72. Luzuriaga MA, Shahrivarkevishahi A, Herbert FC, Wijesundara YH, Gassensmith JJ. Biomaterials and nanomaterials for sustained release vaccine delivery. *Wiley Interdiscip Rev Nanomed Nanobiotechnol*. 2021; 13: e1735.

73. Danhier F, Ansorena E, Silva JM, Coco R, Le Breton A, Préat V. PLGA-based nanoparticles: an overview of biomedical applications. *J Control Release*. 2012; 161: 505–522.

74. Zhu M, Wang R, Nie G. Applications of nanomaterials as vaccine adjuvants. *Hum Vaccin Immunother*. 2014; 10: 2761–2774.

75. Démoulins T, Bassi I, Thomann-Harwood L, et al. Alginate-coated chitosan nanogel capacity to modulate the effect of TLR ligands on blood dendritic cells. *Nanomedicine*. 2013; 9: 806–817.

76. Apostolopoulos V, Thalhammer T, Tzakos AG, Stojanovska L. Targeting antigens to dendritic cell receptors for vaccine development. *J Drug Deliv*. 2013; 2013: 869718.

77. Beduneau A, Ma Z, Grotepas CB, et al. Facilitated monocyte-macrophage uptake and tissue distribution of superparmagnetic iron-oxide nanoparticles. *PLoS ONE*. 2009; 4: e4343.

78. Manolova V, Flace A, Bauer M, Schwarz K, Saudan P, Bachmann MF. Nanoparticles target distinct dendritic cell populations according to their size. *Eur J Immunol*. 2008; 38: 1404–1413.

79. Joshi VB, Geary SM, Salem AK. Biodegradable particles as vaccine delivery systems: size matters. *AAPS J*. 2013; 15: 85–94.

80. Champion JA, Mitragotri S. Shape induced inhibition of phagocytosis of polymer particles. *Pharm Res*. 2009; 26: 244–249.

81. Niikura K, Matsunaga T, Suzuki T, et al. Gold nanoparticles as a vaccine platform: influence of size and shape on immunological responses in vitro and in vivo. *ACS Nano*. 2013; 7: 3926–3938.

82. Foged C, Brodin B, Frokjaer S, Sundblad A. Particle size and surface charge affect particle uptake by human dendritic cells in an in vitro model. *Int J Pharm*. 2005; 298: 315–322.

83. Raghuvanshi RS, Katare YK, Lalwani K, Ali MM, Singh O, Panda AK. Improved immune response from biodegradable polymer particles entrapping tetanus toxoid by use of different immunization protocol and adjuvants. *Int J Pharm*. 2002; 245: 109–121.

84. Muhammad Q, Jang Y, Kang SH, Moon J, Kim WJ, Park H. Modulation of immune responses with nanoparticles and reduction of their immunotoxicity. *Biomater Sci*. 2020; 8: 1490–1501.

85. Liu Y, Hardie J, Zhang X, Rotello VM. Effects of engineered nanoparticles on the innate immune system. *Semin Immunol*. 2017; 34: 25–32.

86. Singh I, Swami R, Khan W, Sistla R. Delivery Systems for Lymphatic Targeting. In: Domb AJ, Khan W, eds. *Focal Controlled Drug Delivery*. Boston, MA: Springer US; 2014: 429–458.

87. Reddy ST, van der Vlies AJ, Simeoni E, et al. Exploiting lymphatic transport and complement activation in nanoparticle vaccines. *Nat Biotechnol*. 2007; 25: 1159–1164.

88. Alberg I, Kramer S, Schinnerer M, et al. Polymeric Nanoparticles with Neglectable Protein Corona. *Small*. 2020; 16: e1907574.

89. Chaplin DD. Overview of the immune response. *J Allergy Clin Immunol*. 2010; 125: S3-23.

90. Parkin J, Cohen B. An overview of the immune system. *The Lancet*. 2001; 357: 1777–1789.

91. Tomar N, De RK. A brief outline of the immune system. *Methods Mol Biol*. 2014; 1184: 3–12.

92. Soares MP, Teixeira L, Moita LF. Disease tolerance and immunity in host protection against infection. *Nat Rev Immunol*. 2017; 17: 83–96.

93. Ademokun AA, Dunn-Walters D. Immune Responses: Primary and Secondary. In: John Wiley & Sons L, ed. *eLS*. Wiley; 2001.

94. Dunkelberger JR, Song W-C. Complement and its role in innate and adaptive immune responses. *Cell Res*. 2010; 20: 34–50.

95. Palucka K, Banchereau J. Dendritic cells: a link between innate and adaptive immunity. *J Clin Immunol*. 1999; 19: 12–25.

96. Macri C, Dumont C, Johnston AP, Mintern JD. Targeting dendritic cells: A promising strategy to improve vaccine effectiveness. *Clin Transl Immunology*. 2016; 5: e66.

97. Burgdorf S, Kurts C. Endocytosis mechanisms and the cell biology of antigen presentation. *Current Opinion in Immunology*. 2008; 20: 89–95.

98. Chen P, Liu X, Sun Y, Zhou P, Wang Y, Zhang Y. Dendritic cell targeted vaccines: Recent progresses and challenges. *Hum Vaccin Immunother*. 2016; 12: 612–622.

99. Théry C, Amigorena S. The cell biology of antigen presentation in dendritic cells. *Current Opinion in Immunology*. 2001; 13: 45–51.

100. Savina A, Amigorena S. Phagocytosis and antigen presentation in dendritic cells. *Immunol Rev*. 2007; 219: 143–156.

101. Griffiths KL, Khader SA. Novel vaccine approaches for protection against intracellular pathogens. *Current Opinion in Immunology*. 2014; 28: 58–63.

102. Kreutz M, Tacken PJ, Figdor CG. Targeting dendritic cells--why bother? *Blood*. 2013; 121: 2836–2844.

103. Tacken PJ, Zeelenberg IS, Cruz LJ, et al. Targeted delivery of TLR ligands to human and mouse dendritic cells strongly enhances adjuvanticity. *Blood*. 2011; 118: 6836–6844.

104. Kastenmüller W, Kastenmüller K, Kurts C, Seder RA. Dendritic cell-targeted vaccines--hope or hype? *Nat Rev Immunol*. 2014; 14: 705–711.

105. Burgdorf S, Kautz A, Böhnert V, Knolle PA, Kurts C. Distinct pathways of antigen uptake and intracellular routing in CD4 and CD8 T cell activation. *Science*. 2007; 316: 612–616.

106. Mantegazza AR, Magalhaes JG, Amigorena S, Marks MS. Presentation of phagocytosed antigens by MHC class I and II. *Traffic*. 2013; 14: 135–152.

107. Engering A, Geijtenbeek TBH, van Vliet SJ, et al. The dendritic cell-specific adhesion receptor DC-SIGN internalizes antigen for presentation to T cells. *J Immunol*. 2002; 168: 2118–2126.

108. van Vliet SJ, Aarnoudse CA, Broks-van den Berg VCM, Boks M, Geijtenbeek TBH, van Kooyk Y. MGL-mediated internalization and antigen presentation by dendritic cells: a role for tyrosine-5. *Eur J Immunol*. 2007; 37: 2075–2081.

109. Yan M, Peng J, Jabbar IA, et al. Despite differences between dendritic cells and Langerhans cells in the mechanism of papillomavirus-like particle antigen uptake, both cells cross-prime T cells. *Virology*. 2004; 324: 297–310.

110. Bonifaz LC, Bonnyay DP, Charalambous A, et al. In vivo targeting of antigens to maturing dendritic cells via the DEC-205 receptor improves T cell vaccination. *J Exp Med*. 2004; 199: 815–824.

111. Birkholz K, Schwenkert M, Kellner C, et al. Targeting of DEC-205 on human dendritic cells results in efficient MHC class II-restricted antigen presentation. *Blood*. 2010; 116: 2277–2285.

112. Berlyn KA, Schultes B, Leveugle B, Noujaim AA, Alexander RB, Mann DL. Generation of CD4(+) and CD8(+) T lymphocyte responses by dendritic cells armed with PSA/anti-PSA (antigen/antibody) complexes. *Clin Immunol*. 2001; 101: 276–283.

113. Apostolopoulos V, Pietersz GA, Gordon S, Martinez-Pomares L, McKenzie IFC. Aldehyde-mannan antigen complexes target the MHC class I antigen-presentation pathway. *Eur J Immunol*. 2000; 30: 1714–1723.

114. Tacken PJ, Ginter W, Berod L, et al. Targeting DC-SIGN via its neck region leads to prolonged antigen residence in early endosomes, delayed lysosomal degradation, and cross-presentation. *Blood*. 2011; 118: 4111–4119.

115. Cifuentes-Rius A, Desai A, Yuen D, Johnston APR, Voelcker NH. Inducing immune tolerance with dendritic cell-targeting nanomedicines. *Nat Nanotechnol*. 2021; 16: 37–46.

116. Merad M, Ginhoux F, Collin M. Origin, homeostasis and function of Langerhans cells and other langerin-expressing dendritic cells. *Nat Rev Immunol*. 2008; 8: 935–947.

117. Caminschi I, Proietto AI, Ahmet F, et al. The dendritic cell subtype-restricted C-type lectin Clec9A is a target for vaccine enhancement. *Blood*. 2008; 112: 3264–3273.

118. Bachem A, Güttler S, Hartung E, et al. Superior antigen cross-presentation and XCR1 expression define human CD11c+CD141+ cells as homologues of mouse CD8+ dendritic cells. *J Exp Med*. 2010; 207: 1273–1281.

119. Clemons TD, Singh R, Sorolla A, Chaudhari N, Hubbard A, Iyer KS. Distinction Between Active and Passive Targeting of Nanoparticles Dictate Their Overall Therapeutic Efficacy. *Langmuir*. 2018; 34: 15343–15349.

120. Cruz LJ, Tacken PJ, Pots JM, Torensma R, Buschow SI, Figdor CG. Comparison of antibodies and carbohydrates to target vaccines to human dendritic cells via DC-SIGN. *Biomaterials*. 2012; 33: 4229–4239.

121. Figdor CG, van Kooyk Y, Adema GJ. C-type lectin receptors on dendritic cells and Langerhans cells. *Nat Rev Immunol*. 2002; 2: 77–84.

122. Martinez-Pomares L. The mannose receptor. *J Leukoc Biol*. 2012; 92: 1177–1186.

123. Backer RA, Diener N, Clausen BE. Langerin+CD8+ Dendritic Cells in the Splenic Marginal Zone: Not So Marginal After All. *Front Immunol*. 2019; 10: 741.

124. Inaba K, Swiggard WJ, Inaba M, et al. Tissue distribution of the DEC-205 protein that is detected by the monoclonal antibody NLDC-145. I. Expression on dendritic cells and other subsets of mouse leukocytes. *Cell Immunol*. 1995; 163: 148–156.

125. Lahoud MH, Ahmet F, Kitsoulis S, et al. Targeting antigen to mouse dendritic cells via Clec9A induces potent CD4 T cell responses biased toward a follicular helper phenotype. *J Immunol*. 2011; 187: 842–850.

126. Shortman K, Heath WR. The CD8+ dendritic cell subset. *Immunol Rev*. 2010; 234: 18–31.

127. Rueckert C, Guzmán CA. Vaccines: from empirical development to rational design. *PLoS Pathog*. 2012; 8: e1003001.

128. Amanna IJ, Slifka MK. Contributions of humoral and cellular immunity to vaccine-induced protection in humans. *Virology*. 2011; 411: 206–215.

129. Schijns V, Majhen D, van der Ley P, et al. Rational Vaccine Design in Times of Emerging Diseases: The Critical Choices of Immunological Correlates of Protection, Vaccine Antigen and Immunomodulation. *Pharmaceutics*. 2021; 13.

130. Gilbert SC. T-cell-inducing vaccines - what's the future. *Immunology*. 2012; 135: 19–26.

131. Barman S, Soni D, Brook B, Nanishi E, Dowling DJ. Precision Vaccine Development: Cues From Natural Immunity. *Front Immunol*. 2021; 12: 662218.

132. Ilinskaya AN, Dobrovolskaia MA. Immunosuppressive and anti-inflammatory properties of engineered nanomaterials. *Br J Pharmacol*. 2014; 171: 3988–4000.

133. Donahue ND, Acar H, Wilhelm S. Concepts of nanoparticle cellular uptake, intracellular trafficking, and kinetics in nanomedicine. *Adv Drug Deliv Rev*. 2019; 143: 68–96.

134. Foroozandeh P, Aziz AA. Insight into Cellular Uptake and Intracellular Trafficking of Nanoparticles. *Nanoscale Res Lett*. 2018; 13: 339.

135. Rietwyk S, Peer D. Next-Generation Lipids in RNA Interference Therapeutics. *ACS Nano*. 2017; 11: 7572–7586.

136. Kube S, Hersch N, Naumovska E, et al. Fusogenic Liposomes as Nanocarriers for the Delivery of Intracellular Proteins. *Langmuir*. 2017; 33: 1051–1059.

137. Yuba E, Harada A, Sakanishi Y, Watarai S, Kono K. A liposome-based antigen delivery system using pH-sensitive fusogenic polymers for cancer immunotherapy. *Biomaterials*. 2013; 34: 3042–3052.

138. Nakamura T, Moriguchi R, Kogure K, Shastri N, Harashima H. Efficient MHC class I presentation by controlled intracellular trafficking of antigens in octaarginine-modified liposomes. *Mol Ther*. 2008; 16: 1507–1514.

139. Hamdy S, Haddadi A, Hung RW, Lavasanifar A. Targeting dendritic cells with nano-particulate PLGA cancer vaccine formulations. *Adv Drug Deliv Rev*. 2011; 63: 943–955.

140. Koerner J, Horvath D, Groettrup M. Harnessing Dendritic Cells for Poly (D,L-lactide-co-glycolide) Microspheres (PLGA MS)—Mediated Anti-tumor Therapy. *Front Immunol*. 2019; 10: 707.

141. Pack DW, Hoffman AS, Pun S, Stayton PS. Design and development of polymers for gene delivery. *Nat Rev Drug Discov*. 2005; 4: 581–593.

142. Benjaminsen RV, Mattebjerg MA, Henriksen JR, Moghimi SM, Andresen TL. The possible "proton sponge " effect of polyethylenimine (PEI) does not include change in lysosomal pH. *Mol Ther*. 2013; 21: 149–157.

143. Su X, Fricke J, Kavanagh DG, Irvine DJ. In vitro and in vivo mRNA delivery using lipid-enveloped pH-responsive polymer nanoparticles. *Mol Pharm*. 2011; 8: 774–787.

144. Krishnamachari Y, Geary SM, Lemke CD, Salem AK. Nanoparticle delivery systems in cancer vaccines. *Pharm Res*. 2011; 28: 215–236.

145. Standley SM, Kwon YJ, Murthy N, et al. Acid-degradable particles for protein-based vaccines: enhanced survival rate for tumor-challenged mice using ovalbumin model. *Bioconjug Chem*. 2004; 15: 1281–1288.

146. Panyam J, Zhou W-Z, Prabha S, Sahoo SK, Labhasetwar V. Rapid endo-lysosomal escape of poly(DL-lactide-co-glycolide) nanoparticles: implications for drug and gene delivery. *FASEB J*. 2002; 16: 1217–1226.

147. Foster S, Duvall CL, Crownover EF, Hoffman AS, Stayton PS. Intracellular delivery of a protein antigen with an endosomal-releasing polymer enhances CD8 T-cell production and prophylactic vaccine efficacy. *Bioconjug Chem*. 2010; 21: 2205–2212.

148. Convertine AJ, Benoit DSW, Duvall CL, Hoffman AS, Stayton PS. Development of a novel endosomolytic diblock copolymer for siRNA delivery. *J Control Release*. 2009; 133: 221–229.

149. Wilson JT, Keller S, Manganiello MJ, et al. pH-Responsive nanoparticle vaccines for dual-delivery of antigens and immunostimulatory oligonucleotides. *ACS Nano*. 2013; 7: 3912–3925.

150. Rincon-Restrepo M, Mayer A, Hauert S, et al. Vaccine nanocarriers: Coupling intracellular pathways and cellular biodistribution to control CD4 vs CD8 T cell responses. *Biomaterials*. 2017; 132: 48–58.

151. Stano A, Scott EA, Dane KY, Swartz MA, Hubbell JA. Tunable T cell immunity towards a protein antigen using polymersomes vs. solid-core nanoparticles. *Biomaterials*. 2013; 34: 4339–4346.

152. Harding CV, Collins DS, Kanagawa O, Unanue ER. Liposome-encapsulated antigens engender lysosomal processing for class II MHC presentation and cytosolic processing for class I presentation. *J Immunol*. 1991; 147: 2860–2863.

153. Belizaire R, Unanue ER. Targeting proteins to distinct subcellular compartments reveals unique requirements for MHC class I and II presentation. *Proc Natl Acad Sci U S A*. 2009; 106: 17463–17468.

154. Joffre OP, Segura E, Savina A, Amigorena S. Cross-presentation by dendritic cells. *Nat Rev Immunol*. 2012; 12: 557–569.

155. Blander JM. Regulation of the Cell Biology of Antigen Cross-Presentation. *Annu Rev Immunol*. 2018; 36: 717–753.

156. Shen L, Sigal LJ, Boes M, Rock KL. Important role of cathepsin S in generating peptides for TAP-independent MHC class I crosspresentation in vivo. *Immunity*. 2004; 21: 155–165.

157. Lützner N, Kalbacher H. Quantifying cathepsin S activity in antigen presenting cells using a novel specific substrate. *J Biol Chem*. 2008; 283: 36185–36194.

Chapter 2

Goals of the Thesis

Nanoparticles are one of the most popular tools in contemporary vaccine development. They offer a number of benefits that can greatly improve the effectiveness of vaccination. This is mainly because the particles mimic pathogens, causing the immune system to react strongly to them. Their size is ideal for draining directly and quickly into the lymph nodes after injection. Lymph nodes are the key organ for induction of the (adaptive) immune response, since B and T cells and many other immune cells such as dendritic cells and macrophages are located there. Furthermore, the particle size between 20 and 200 nm is perfect for uptake by dendritic cells. This is crucial for inducing T cell responses because dendritic cells are most effective in activating T cells. In addition to the size, the variety of design options are very attractive. For example, when antigens are attached to the particle surface in a highly repetitive manner, cross-linking of B cell receptors can occur, resulting in strong B cell activation.

Although the design variability of the nanoparticles would offer the possibility to create universal vaccines that trigger both a humoral and a cellular immune response, most of the developed NP vaccines usually only induce an antibody response with a $CD4^+$ T cell response, but none or only a poor $CD8^+$ T cell response. There are already some approaches to induce cytotoxic T cell responses, but there is still a lot of room for improvement. Most importantly, the NP vaccines should target dendritic cells as they are potent inducers of T cells. Subsequent intracellular trafficking of the antigen delivery platform is critical to whether $CD4^+$ or $CD8^+$ T cells are activated. Previous strategies to enhance the cytotoxic T cell response are based on pH-sensitive, membrane fusion-induced or reduction-triggered release of antigens in the early endosome of dendritic cells, resulting in endosomal escape of the antigen with subsequent processing by the proteasome in the cytosol and presentation on MHC-I to $CD8^+$ T cells.

The aim of this work was to develop nanoparticles with antigens on the surface that exhibit a new enzyme-induced release mechanism for the antigens. Cathepsin S, a protease that is one of the few active enzymes in the early endosome of dendritic cells, was chosen as target enzyme. Antigens and nanoparticles were linked with a substrate of cathepsin S. Therefore, the conjugated antigens should be released in the early endosome after uptake into dendritic cells due to linker cleavage by cathepsin S, allowing endosomal escape and subsequent cross-presentation of the antigens.

A robust fabrication process for the nanoparticles and comprehensive knowledge about their composition, physicochemical properties and behavior in biological fluids is crucial for the right planning of *in vitro/in vivo* experiments and the correct interpretation of the

results. Therefore, a method for the production of pathogen-mimicking nanoparticles consisting of polymeric particle core and model antigen ovalbumin covalently conjugated *via* an enzymatically cleavable linker was first developed and the particles were extensively characterized (**Chapter 3**). Since the antigens should only be released through the enzymatic cleavage of the linker, the focus when developing the manufacturing process was on creating particles in which antigens are conjugated exclusively *via* the linker and are not adsorbed to the particle surface. For this purpose, different amounts of ovalbumin were tested in the conjugation reaction. Additionally, a method for functionalizing proteins was developed, allowing any antigen or protein to be conjugated to the particles, dramatically increasing the versatility of the developed antigen delivery system. Nanoparticles were characterized physicochemically with regard to size, zeta potential and antigen attachment mode. Moreover, storage stability, behavior in culture medium and protein corona formation in serum were tested.

Next, the concept of enhancing antigen cross-presentation on dendritic cells by enzymatic release of antigens in the early endosome was examined with *in vitro* experiments (**Chapter 4**). Cleavability of the linker by early endosomal protease cathepsin S was evaluated to ensure suitability for triggering antigen release. In addition, purity and toxicity of the particles and their cellular uptake in dendritic cells were verified. Finally, the intracellular fate of the particles after internalization in dendritic cells and cross-presentation by dendritic cells with subsequent activation of CD8+ T cells was evaluated in comparison to a similar particle system with a non-cleavable linker.

In **Chapter 5**, an additional pH-sensitive release mechanism for ovalbumin was integrated into the particle system. Acid-induced antigen delivery may also enhance cross-presentation by dendritic cells as it enables release in the slightly acidic environment of early endosomes and thus endosomal escape followed by cytosolic processing and loading onto MHC-I molecules. A mild visible light-induced copper-free click reaction was used to couple the peptide linker to the block copolymers. Click reactions in general are attractive because they are highly selective and exhibit fast reaction kinetics and high yields, and the mild click reaction used here was particularly charming as it forms a triazoline structure that is degradable in acidic environment. The focus here was on transforming the click reaction for bioconjugations and evaluating acid-induced ovalbumin release.

As a side project of this thesis, a new radiotracer for sentinel lymph node detection was developed (**Chapter 6**). The currently approved detection agents have various

disadvantages, such as categorization as blood product involving time-consuming patient information and batch documentation, or they have a wide size distribution leading to poor accuracy, or they are very expensive. Therefore, ^{99m}Tc-labelled polymeric nanoparticles were developed as a new alternative radiotracer overcoming the drawbacks of current tracers. The particles were prepared using microfluidics and preparation parameters were optimized to synthesize particles with a defined size and narrow size distribution. Afterwards, the nanoparticles were radiolabelled with ^{99m}Tc by a direct method and ideal reaction conditions were developed to obtain a radiotracer with 100% radiochemical purity.

Chapter 3

Development of polymeric nanoparticles

with covalently attached antigens

Abstract

Nanoparticles are very attractive as antigen delivery platforms because their size and highly versatile structure, together with their safe manufacture, allow for potent activation of the immune system by mimicking the properties of pathogens, while exhibiting minimal side effects and toxicity. The aim of this work was the development and comprehensive characterization of a nanoparticle-based system that can be used as a vaccine. For this purpose, the antigen delivery platform was first prepared by covalently binding the model antigen ovalbumin to the surface of polymeric nanoparticles. The subsequent characterization of the physicochemical properties demonstrated the ideal virus-sized dimensions of the particles and their well-defined composition with exclusively covalently conjugated antigens. By additionally proving the good storage stability, lack of aggregation in culture medium and negligible formation of a protein corona after serum incubation, an ideal knowledge base for subsequent *in vivo* and *in vitro* tests could be created. The findings suggest that the developed particle system possesses ideal properties that make it a promising candidate as a vaccine delivery platform. Furthermore, a conjugation strategy applicable for any protein was established, that excludes the requirement for protein reduction prior to conjugation reaction.

1   Introduction

Nanoparticles (NPs) hold great potential as antigen delivery platforms recognizable by the incredible number of nanoparticulate vaccines that have been developed over the last few decades [1–3]. NPs are attractive for vaccine development because their virus-sized dimensions of 20-200 nm are ideal for activating the immune system. Substances in this size range are preferentially recognized and taken up by antigen presenting cells such as dendritic cells (DCs) [4, 5] and can also be drained directly to the lymph nodes (LNs), home to large numbers of immune cells [6]. Additionally, the highly versatile structure of NPs is advantageous for vaccine development as it allows for the tailoring and control of the immune response [7]. Furthermore, NPs have a defined and simple structure [8] and are safe and easy to manufacture [9], which is of crucial importance for vaccines, since complex and not well-defined mixtures bear the risk of side effects and excessive immune reactions [10].

For the development of a NP-based vaccine, a wide range of material and design options are available [11–13]. The various particle types offer different advantages and disadvantages. For example, lipid and polymeric NPs are biocompatible, biodegradable and non-toxic, while inorganic NPs are simple, precise and inexpensive to produce [5, 13]. NPs also offer many possibilities regarding antigen and adjuvant incorporation. Antigens can be encapsulated or attached to surface. Encapsulated antigens are better protected from degradation [13]. Surface-attached antigens, on the other hand, can interact directly with B cells, enabling the induction of an antibody response. Since NPs are also captured by DC and thereby induce T cell responses [6], the formation of a universal immune response is possible. In terms of attachment type, covalently bound antigens are better than adsorbed ones because a chemical bond is more stable and NPs can reach the cells of interest without antigen loss [5]. When coupling antigens to NPs, the choice of coupling reaction is of crucial importance as it can greatly influence the manufacturing effort, vaccine stability and behavior *in vivo*, and the type of immune response. Generally, accessible thiol groups in proteins are a popular target used for coupling reactions [14]. However, most proteins do not contain freely accessible thiols, so harsh reduction conditions are required to set them free [15], increasing the risk of denaturation [16].

In this study, a system was developed consisting of polymeric NPs with antigens covalently bound to the surface, that can be used as a vaccine. To this end, the model antigen ovalbumin (OVA) was coupled to poly(ethylene glycol)-poly(lactic-co-glycolic

acid) (PEG-PLGA) NPs using a peptide linker. The colloidal stability of the particles during storage and under cell culture conditions as well as serum protein adsorption were investigated. Additionally, a protocol was devised that allows conjugation of proteins lacking free thiols *via* maleimide (Mal) thiol conjugation without the need for prior protein reduction.

2 Materials and Methods

2.1 Materials

Carboxylic acid-terminated poly(ethylene glycol) (HOOC-PEG-OH) with a molecular weight of 5000 Da was obtained from JenKem Technology USA Inc. (Allen, TX, USA). Cathepsin S substrate (CatS subs; amino acid sequence GRKWPPMGLPWEC-DArg-NH$_2$) was synthesized by Genscript (Piscataway, NJ, USA). Penicillin-streptomycin (P-S) was obtained from PAN-Biotech GmbH (Aidenbach, Germany). Pierce™ BCA protein assay kit, PageRuler™ plus prestained protein ladder, Imject™ maleimide-activated ovalbumin (Mal-OVA) and sulfosuccinimidyl 4-[N-maleimidomethyl]cyclohexane-1-carboxylate (sulfo-SMCC) were purchased from Thermo Fisher Scientific (Waltham, MA, USA). Ethylenediaminetetraacetic acid (EDTA) was obtained from AppliChem GmbH (Darmstadt, Germany) and OVA from InvivoGen (San Diego, CA, USA). Tris(2-carboxyethyl)phosphine (TCEP) and sodium chloride (NaCl) were purchased from Carl Roth GmbH + Co. KG (Karlsruhe, Germany) and 2 % BCL Agarose Bead Standard (50-150 μm) from Agarose Bead Technologies ABT (Madrid, Spanien). Resomer® RG 752 H PLGA and all other materials and reagents were purchased from Sigma Aldrich (Taufkirchen, Germany). Millipore water used for dialysis and buffer preparation was obtained from a Millipore Milli-Q water purification system (Billerica, MA, USA).

2.2 Polymer synthesis and NP preparation

2.2.1 Block Copolymer-Synthesis

HOOC-PEG$_{5k}$-PLGA$_{13k}$ block copolymer was synthesized by adapting a protocol described by Qian *et al.* [17]. Briefly, racemic 3,6-dimethyl-1,4-dioxane-2,5-dione (*D,L*-lactide) and 1,4-dioxane-2,5-dione (glycolide) were purified by recrystallization from ethyl acetate and tetrahydrofuran (THF), respectively, and dried under vacuum for 12 h.

HOOC-PEG-OH (0.09 mmol) used as a macroinitiator was mixed with lactide (12.6 mmol). Immediately after starting ring-opening polymerization by adding 1,8-diazabicyclo[5.4.0]undec-7-ene (0.27 mmol), glycolide (2.61 mmol) was continuously added at a rate of 1.2 ml/min (10 min). Afterwards, the reaction was quenched with benzoic acid (1.35 mmol). For purification, block copolymer was precipitated in diethyl ether and dried under vacuum and ^{1}H-NMR spectrum was recorded in CDCl$_3$ at 295 K using a Bruker Avance 300 spectrometer (Bruker BioSpin GmbH, Rheinstetten, Germany). Molecular weight and mass ratio of lactic to glycolic units were calculated from integration of ^{1}H-NMR data assuming the molecular weight of HOOC-PEG provided by the manufacturer.

2.2.2 Synthesis of CatS subs-PEG-PLGA

HOOC-PEG$_{5k}$-PLGA$_{13k}$ was covalently coupled to the lysine residue of CatS subs using ethyl-3-(3-dimethylaminopropyl)carbodiimide/N-hydroxysuccinimide (EDC/NHS) chemistry. First, HOOC-PEG$_{5k}$-PLGA$_{13k}$ (3.9 µmol) was activated with EDC (97.5 µmol) and NHS (97.5 µmol) in N,N-dimethylformamide (DMF) for 2 h under stirring. Disulfide bonds in CatS subs (5.85 µmol) were reduced by incubation with dithiothreitol (DTT; 58.5 µmol) in DMF for 1 h. 2-Mercaptoethanol (2-ME; 195 µmol) was added to quench EDC/NHS reaction, prior to addition of CatS subs-DTT mixture and N,N-diisopropylethylamine (39 µmol). After 72 h, resulting polymer was precipitated in diethyl ether and dialyzed against Millipore water for 24 hours using a 6-8 kDa molecular weight cut-off regenerated cellulose dialysis membrane (Spectrum Laboratories Inc., Rancho Dominguez, CA, USA) to remove unreacted CatS subs and excess reactants.

2.2.3 NP preparation

NPs were prepared by nanoprecipitation. For that, CatS subs-PEG-PLGA and PLGA were mixed at a mass ratio of 7:3 and diluted in acetonitrile (ACN) to a final concentration of 10 mg/ml. Polymer mixture was then added dropwise to vigorously stirring 0.1X low-endotoxin Dulbecco's phosphate-buffered saline (LT-PBS) (v/v) to a final concentration of 1 mg/ml. NPs were diluted with an equal volume of 0.1X LT-PBS immediately after preparation. Finally, they were purified and concentrated by ultracentrifugation using an Amicon® Ultra-15 MWCO 100 kDa centrifugal filter (Merck KGaA, Darmstadt, Germany) at 1400 *g*.

2.2.4 Conjugation of OVA

Mal-OVA was attached to cysteine residue of CatS subs on particle surface *via* maleimide thiol chemistry. In brief, CatS subs NPs were reduced immediately after preparation with a 10- or 50-fold molar excess of TCEP relative to CatS subs. After 2 h of gentle stirring, reduced CatS subs NPs were purified *via* ultracentrifugation with an Amicon® Ultra-15 MWCO 100 kDa centrifugal filter (Merck KGaA, Darmstadt, Germany) at 1400 *g*. Subsequently, CatS subs NPs were resuspended in LT-PBS and reacted with Mal-OVA for 4 h at room temperature. The amount of Mal-OVA was calculated either based on the NP surface area and protein size, where it corresponds to the protein amount forming a monolayer on the NP surface, or such that the molar ratio of maleimide groups to CatS subs was 1:1. OVA NPs were washed with 0.1X LT-PBS by ultracentrifugation with an Amicon® Ultra-15 MWCO 100 kDa centrifugal filter (Merck KGaA, Darmstadt, Germany) at 1400 *g*.

2.3 NP characterization

2.3.1 NP size

Hydrodynamic diameter and polydispersity index (PDI) of all NPs were measured using a Malvern ZetaSizer Nano ZS (Malvern Instruments GmbH, Lappersdorf, Germany) with a 633 nm He-Ne laser at a backscatter angle of 173°. For size and PDI determination samples were diluted in 0.1X LT-PBS to 1 mg/ml and measurements were performed at 25 °C in disposable microcuvettes (Brand, Wertheim, Germany).

2.3.2 PEG quantification and NP concentration

Particle PEG concentration was quantified by a colorimetric iodine complexing assay [18]. NP mass concentration was obtained by correlating the determined particle PEG content with the exact NP mass determined gravimetrically after lyophilization, as described before [19]. NP number concentration c_N was calculated after Wen *et al.* [20] assuming a spherical particle shape using equation 1, where c_m is the particle mass concentration, ρ_{NP} is the particle density (1.3 g/cm³) [21] and d_{NP} is the hydrodynamic diameter of the NPs obtained through DLS measurements.

$$c_N = \frac{c_m}{\rho_{NP} \cdot \frac{4}{3}\pi\left(\frac{d_{NP}}{2}\right)^3} \quad (1)$$

2.3.3 CatS subs and OVA quantification

The amount of CatS subs and OVA conjugated on NP surface was assessed with a Pierce™ BCA protein assay kit, using CatS subs and OVA as standards, following the manufacturer's instructions. Absorbance was measured with a FLUOstar Omega microplate reader (BMG Labtech, Ortenberg, Germany). To calculate the OVA amount, absorbance of CatS subs NPs was subtracted from the absorbance of OVA NPs.

2.3.4 OVA attachment characterization

Sodium dodecyl sulfate (SDS)-polyacrylamide gel electrophoresis (PAGE) was performed to determine the type of OVA attachment to the particle surface. In brief, 14% polyacrylamide gels were prepared and loaded with soluble OVA as reference and the different particle formulations. After running electrophoresis for 60 min at 120 V, protein bands were detected by Coomassie Blue staining and NPs were visualized by barium iodide staining [22]. Gels were imaged with a ChemiDoc™ MP gel imaging system (BioRad Laboratories GmbH, München, Germany) and Image Lab™ 6.0 software (BioRad Laboratories GmbH, München, Germany) was used to evaluate them.

2.4 Colloidal stability

To determine storage stability, OVA NPs (5 mg/ml) were incubated in 0.1X LT-PBS for 37 days at either 4 °C or room temperature. Size and PDI were determined as described above.

Colloidal stability under cell culture conditions was evaluated by incubating OVA NPs (0.75 mg/ml) for 24 h at 37 °C in RPMI 1640 supplemented with 10% heat inactivated fetal calf serum (FCS), 50 µM 2-ME and 1% P-S. At the displayed time points, size distribution was determined using Malvern ZetaSizer Nano ZS (Malvern Instruments GmbH, Lappersdorf, Germany).

2.5 Serum protein adsorption

Adsorption of serum proteins to NP surface was assessed by incubating OVA NPs (0.75 mg/ml) in 50% FCS (v/v) for 1 h at 37 °C. Afterwards, NPs were isolated from plasma proteins by size exclusion chromatography (SEC) using a column packed with 2 % BCL Agarose Bead Standard (50-150 µm). 0.1X LT-PBS was used as elution buffer and chromatography process was monitored using Malvern ZetaSizer Nano ZS

(Malvern Instruments GmbH, Lappersdorf, Germany). SEC was performed at a constant flow rate of 2 ml/min. Fractions containing NPs were concentrated *via* ultracentrifugation with an Amicon® Ultra-15 MWCO 100 kDa centrifugal filter (Merck KGaA, Darmstadt, Germany) at 1400 *g*. 0.1X LT-PBS incubated in 50% FCS was treated the same as the OVA NPs and used as control to determine proteins co-eluting with the NPs.

Size and PDI of the non-incubated OVA NPs and the concentrated fractions from SEC were determined as described above.

To qualitatively analyze the adsorbed proteins, SDS-PAGE was performed. Briefly, a 14% polyacrylamide gel was loaded with non-incubated OVA NPs, incubated and isolated OVA NPs, PBS control and 0.5% FCS (v/v) as reference. Electrophoresis was run for 60 min at 120 V and protein bands were visualized by silver staining. Gel imaging and evaluation were performed as described above.

Adsorbed proteins were quantified using a Pierce™ BCA protein assay kit, following the manufacturer's instructions. NPs were diluted to a concentration of 1 mg/ml and PBS control was diluted the same as the incubated OVA NPs. Bovine serum albumin (BSA) was used as standard and absorbance at 562 nm was read with a plate reader (Fluostar Omega, BMG Labtech).

2.6 Maleimide labelling of proteins

2.6.1 Determination of free thiols per protein

The number of free thiols per protein were quantified using Ellman's assay. Succinctly, 5,5-dithio-bis-(2-nitrobenzoic acid) (DTNB; Ellman's reagent) was dissolved in assay buffer (0.1 M phosphate buffer + 1 mM EDTA, pH 8.0) to prepare a stock solution (4 mg/ml). The stock solution (200 µl) was diluted with assay buffer (10 ml) to generate working solution. A calibration curve was obtained with a series of cysteine hydrochloride standard solutions (0-1.5 mM). OVA, BSA and human serum albumin (HSA) were dissolved in assay buffer at different concentrations (0.1–1 mM). Samples and standards (12.5 µl) were mixed with working solution (127.5 µl) and after a 15-minute incubation period, the absorbance at 412 nm was measured with a plate reader (Fluostar Omega, BMG Labtech). Free thiols per protein were calculated by dividing the determined molar concentration of thiols by the molar concentration of the proteins.

2.6.2   Investigation of different reaction conditions for maleimide labelling reaction

In order to determine the best reaction conditions for labelling proteins with maleimides, various parameters were tested. First, a stock solution of OVA (40 mg/ml) in Millipore water was prepared and further diluted with LT-PBS. 1.0 ml of OVA solutions (10, 5, 1 and 0.5 mg/ml, respectively) were incubated with a 5-, 10-, 20- and 50-fold molar excess, respectively, of sulfo-SMCC for 30 min, 1 h and 2 h at room temperature. Resulting maleimide-activated proteins were purified and concentrated by ultracentrifugation using an Amicon® Ultra-4 MWCO 10 kDa centrifugal filter (Merck KGaA, Darmstadt, Germany) at 7000 g. Protein concentration was determined with a Pierce™ BCA protein assay kit, using OVA as standards, according to the manufacturer's instructions. Maleimide concentration was assessed using an inverse Ellman's assay. In brief, samples were incubated with a known amount of cysteine hydrochloride for 1 h at room temperature. Thereafter, the unreacted cysteine hydrochloride was quantified *via* an Ellman's assay, as described above. The amount of maleimides corresponds to the amount of cysteines converted. The number of maleimide groups per protein was calculated by dividing molar concentration of maleimides by the molar concentration of the proteins.

2.6.3   Maleimide labelling of proteins

To synthesize maleimide-activated proteins, sulfo-SMCC was covalently conjugated *via* its NHS ester to primary amines in OVA, BSA and HSA. In short, proteins were dissolved in Millipore water (40 mg/ml) and diluted to 0.5 mg/ml with LT-PBS. After addition of a 50-fold molar excess of sulfo-SMCC, reaction mixture was incubated for 30 min at room temperature. The resulting proteins were purified *via* ultracentrifugation using an Amicon® Ultra-4 MWCO 10 kDa centrifugal filter (Merck KGaA, Darmstadt, Germany) at 7000 g. The number of maleimides per protein were determined as described above.

For purity test and analysis of protein integrity, a high-performance liquid chromatography (HPLC) analysis was performed with an Agilent Infinity 1260 HPLC (Agilent Technologies GmbH, Waldbronn, Germany). A SEC-HPLC Tosoh-3000SWXL column was used and operated at 30 °C. The mobile phase consisted of 50 mM PBS (pH 7.4) + 100 mM NaCl + 0.05% (m/V) sodium azide. Per run a sample volume of 1 µl was injected and the flow rate was set to 0.75 mL/min. Both Sulfo-SMCC and proteins were detected at a wavelength of 280 nm. HPLC runs were performed with the maleimide-activated proteins, freshly dissolved proteins, freshly dissolved sulfo-SMCC and heat denatured proteins (1 h, 100 °C)

3   Results

3.1   Development of NPs with covalently attached antigens

In order to prepare particles with antigens covalently conjugated to the NP surface, HOOC-PEG$_{5k}$-PLGA$_{13k}$ block co-polymer was first synthesized *via* ring-opening polymerization. Characteristic shifts in ^{1}H-NMR spectrum (Figure 1) confirmed successful synthesis of block co-polymer. The proton peaks at δ 1.57 and 5.16 were attributed to the methyl group and methine group of lactic units, respectively, whereas the peak at δ 4.81 corresponded to the methylene group of glycolic units. Proton peaks at δ 3.46 and 3.63 were assigned to methylene groups of PEG units. The molecular weights of HOOC-PEG-PLGA and the PLGA portion and the mass ratio of lactic to glycolic units, calculated based on the integration values of the described peaks, were ~18.1 kDa, ~13.1 kDa and ~72:28, respectively (please refer to supporting information for exact explanation of the calculation).
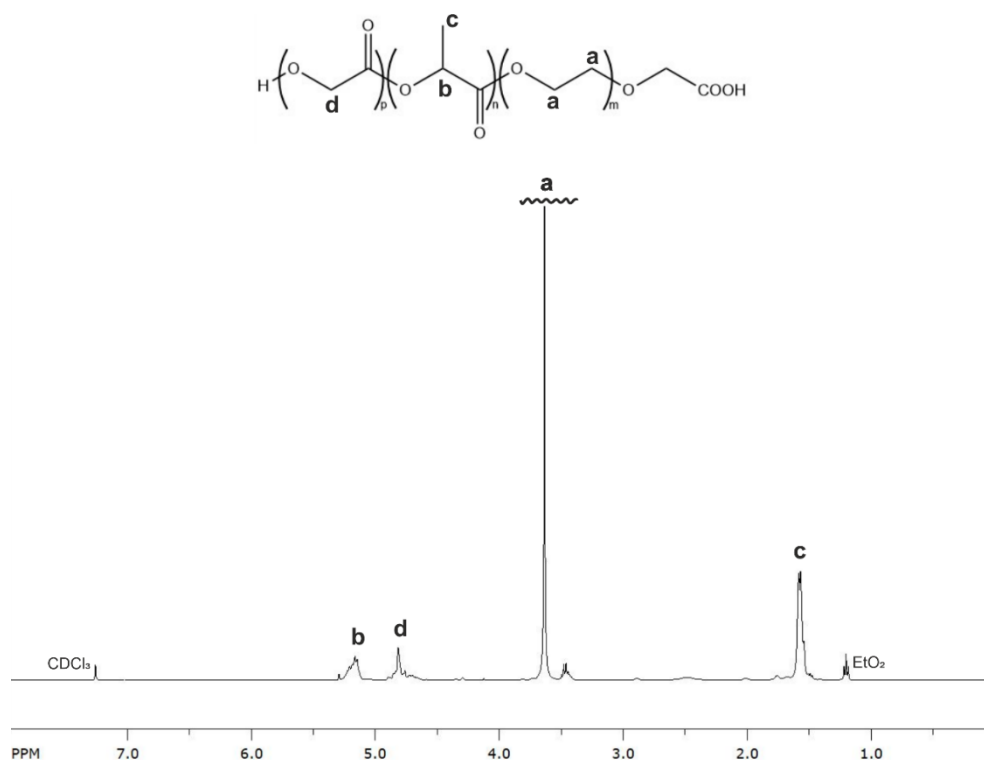
Figure 1. ^{1}H-NMR spectrum of HOOC-PEG$_{5k}$-PLGA$_{13.1k}$ obtained in CDCl$_3$. δ (ppm): 1.20 (solvent peak), 1.57 (-OCH(CH$_3$)CO-), 3.46 (-OCH$_2$CH$_2$OCH$_2$COOH), 3.63 (-OCH$_2$CH$_2$-), 4.81 (-OCH$_2$CO-), 5.16 (-OCH(CH$_3$)CO-), 7.26 (solvent peak). 'm', 'n' and 'p' represent the repeating number of PEG, lactic and glycolic units, respectively.

Afterwards, the linker CatS subs was coupled to HOOC-PEG-PLGA by EDC/NHS chemistry (Figure 2A). The degree of polymer functionalization was determined by quantifying the molar PEG and CatS subs content of NPs using a colorimetric iodine complexing assay and BCA assay, respectively. As shown in Figure 2B, both PEG and CatS subs amount were approximately 100%, demonstrating complete polymer modification.
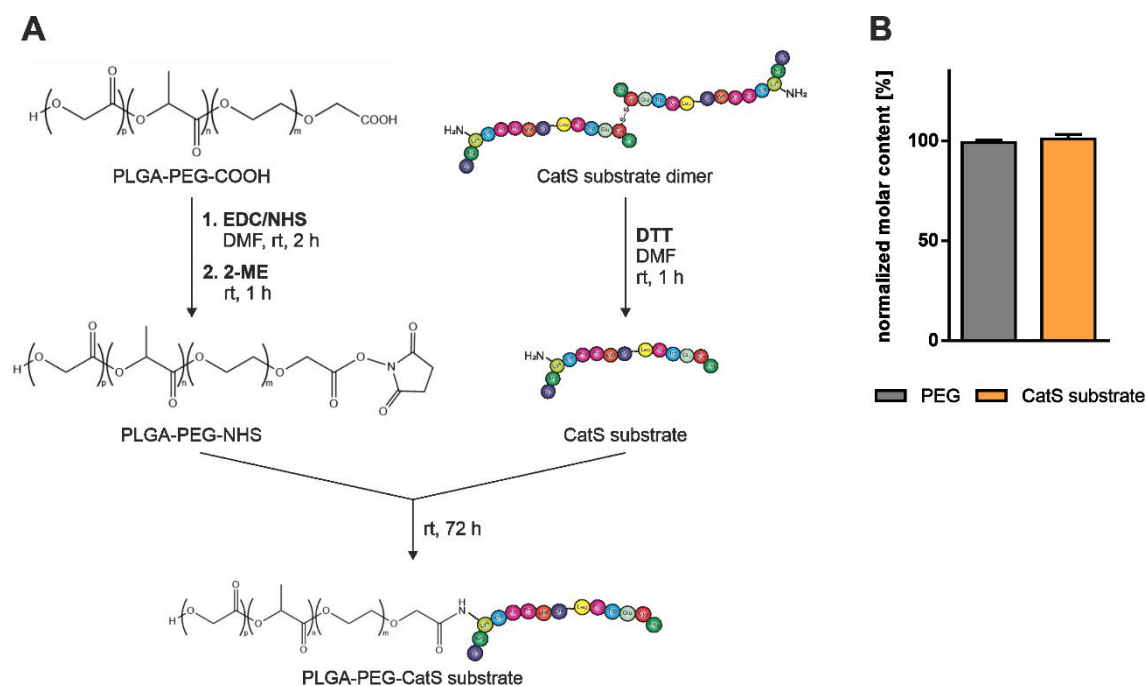
Figure 2. Coupling of CatS subs to PEG-PLGA block copolymers. (A) Synthesis strategy of the conjugation reaction. (B) Molar content of PEG and CatS subs normalized to the PEG content. Results represent mean ± SD of n = 3 measurements.

Finally, CatS subs NPs were prepared *via* nanoprecipitation and model antigen OVA was conjugated to NP surface through maleimide-thiol reaction using a maleimide-activated OVA that reacted with the thiol in the cysteine residue of CatS subs. To assess the influence of the OVA amount used for the coupling reaction on the type of OVA attachment formed, two different approaches were tested: The amount of OVA for the reaction was chosen such that it either enabled the formation of an OVA monolayer on the NP surface (approach 1; calculation based on NP surface area and protein dimensions) or that the molar ratio of maleimide groups to CatS subs was 1:1 (approach 2).

Regardless of the synthesis approach, the NPs were 100-150 nm in size and had a homogenous size distribution, as evidenced by the PDI below 0.3 (Figure 3A). Conjugation approach 1 (OVA monolayer) resulted in a slight decrease in size when comparing antigen-free CatS subs NPs and antigen-bearing OVA NPs, while approach 2 (Mal:CatS subs (1:1)) led to a slight increase in NP size (Figure 3A).

SDS-PAGE was used to characterize the type of OVA attachment (nonspecific adsorption or covalent conjugation) to the NP surface. Proteins adsorbed to NPs leave the particle surface during electrophoresis and migrate into the gel similar to free, soluble proteins. In contrast, covalently conjugated proteins do not migrate into the gel but remain on the particle surface. Figures 3C and 3E show barium iodide stained gels of the NPs synthesized according to approach 1 (Figure 3C) or approach 2 (Figure 3E). A clear NP band in the sample well was visible for all particles, as NPs are too large to migrate into the gel. Coomassie stained gel of NPs prepared with an OVA amount that could form an OVA monolayer on NP surface (approach 1) is depicted in Figure 3B. Soluble OVA (lane 2) showed the typical OVA band at 45 kDa, whereas OVA NPs (lane 3) displayed only one band in the sample well and none at 45 kDa, confirming the covalent conjugation of OVA to NPs. Figure 3D shows the Coomassie stained gel of NPs synthesized with a 1:1 ratio of maleimide to Cats subs (approach 2). Here, similar to the soluble OVA (lane 2), the typical OVA band at 45 kDa was visible for OVA NPs (lane 3), indicating that besides the conjugated proteins, a large proportion of OVA was only adsorbed.
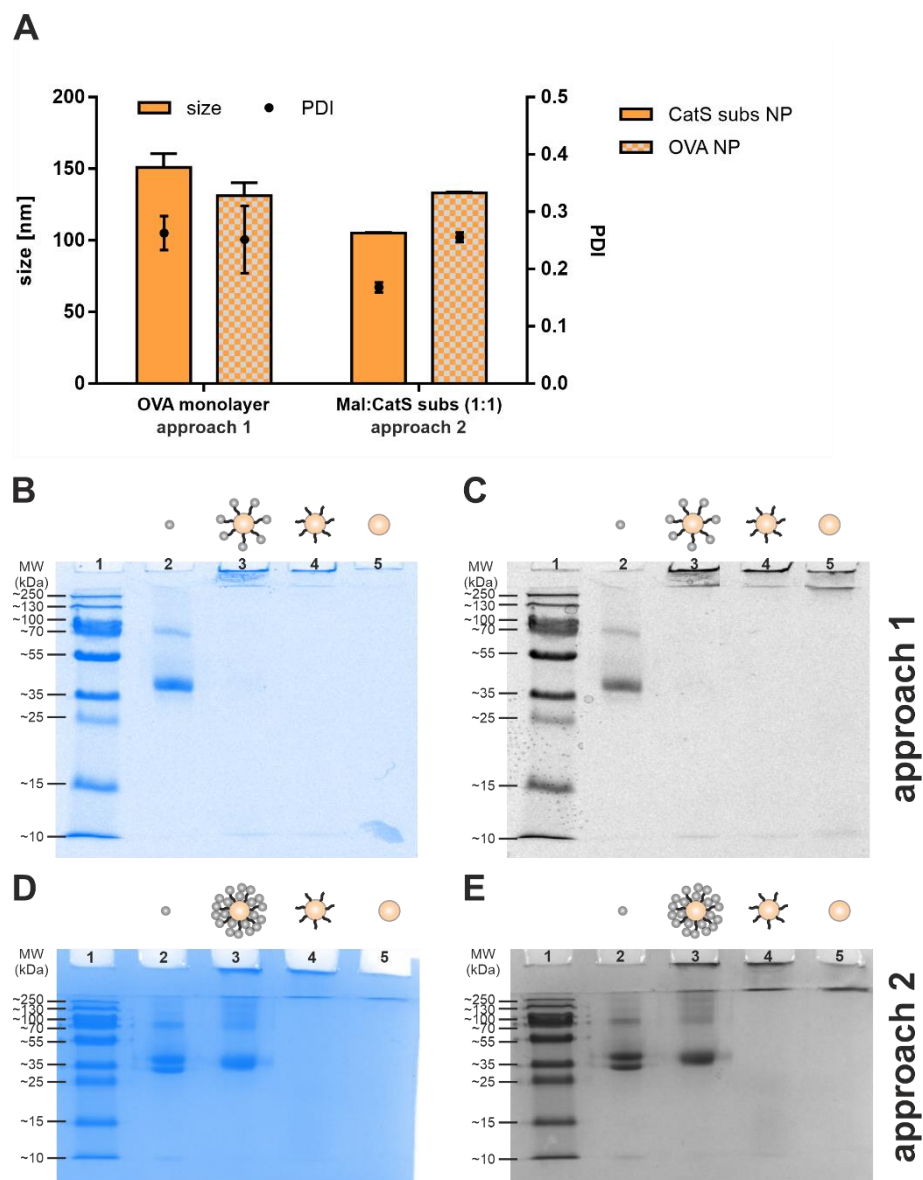
Figure 3. NP characterization. (A) Size and PDI of the antigen-free CatS subs NPs and antigen-bearing OVA NPs prepared by either approach 1 (OVA monolayer) or approach 2 (Mal:CatS subs (1:1)). (B) Coomassie and (C) barium iodide stained SDS-PAGE gels of NPs synthesized in such a way that an OVA monolayer could be formed on the NP surface (approach 1). (D) Coomassie and (E) barium iodide stained SDS-PAGE gels of NPs synthesized with a 1:1 molar ratio of maleimide to Cats subs (approach 2). Lane 1: ladder, lane 2: soluble OVA, lane 3: OVA NP, lane 4: CatS subs NP, lane 5: HOOC-PEG-PLGA NP. Results represent mean ± SD of at least n = 3 measurements.

As shown in Table 1, BCA assay revealed that OVA NPs synthesized according to approach 2 (Mal:CatS subs (1:1)) had almost twice the number of proteins per particle compared to OVA NPs synthesized with approach 1 (OVA monolayer). The ratio of maleimide groups to CatS subs was calculated to be 0.6:1 for approach 1.

Table 1. Amount of OVA per NP of prepared OVA NPs and molar ratio of maleimide groups to CatS subs in the synthesis. The OVA amount used for coupling to the NP surface was chosen such that either an OVA monolayer could be formed on the NP surface (approach 1) or a 1:1 molar ratio of maleimide groups to CatS subs was obtained (approach 2). Results represent mean ± SD of n = 3 measurements.

	µg OVA per mg NP	OVA per NP	Maleimide:CatS subs
OVA monolayer	143 ± 5	2383 ± 182	0.6:1
Mal:CatS subs (1:1)	204 ± 7	4392 ± 150	1:1

3.2   Colloidal stability of OVA NPs

The colloidal stability of OVA NPs over time in 0.1X LT-PBS at room temperature or 4 °C, as well as in cell culture medium (RPMI 1640 supplemented with 10% heat inactivated FCS, 50 µM 2-ME and 1% P-S) was assessed by dynamic light scattering (DLS) measurements. As shown in Figure 4A, no changes in size and PDI were detectable for OVA NPs after storage for 37 days in 0.1X LT-PBS at 4 °C. In contrast, at room temperature size and PDI of OVA NPs slightly increased (Figure 4B). Furthermore, colloidal stability and aggregation behavior of OVA NPs under cell culture conditions was very satisfactory (Figure 4C). Neither an increase in size nor aggregates were observed. The peaks with sizes of 10-50 nm probably originate from ingredients such as proteins, antibodies or exosomes [23] in FCS added to cell culture medium.

A

B

C
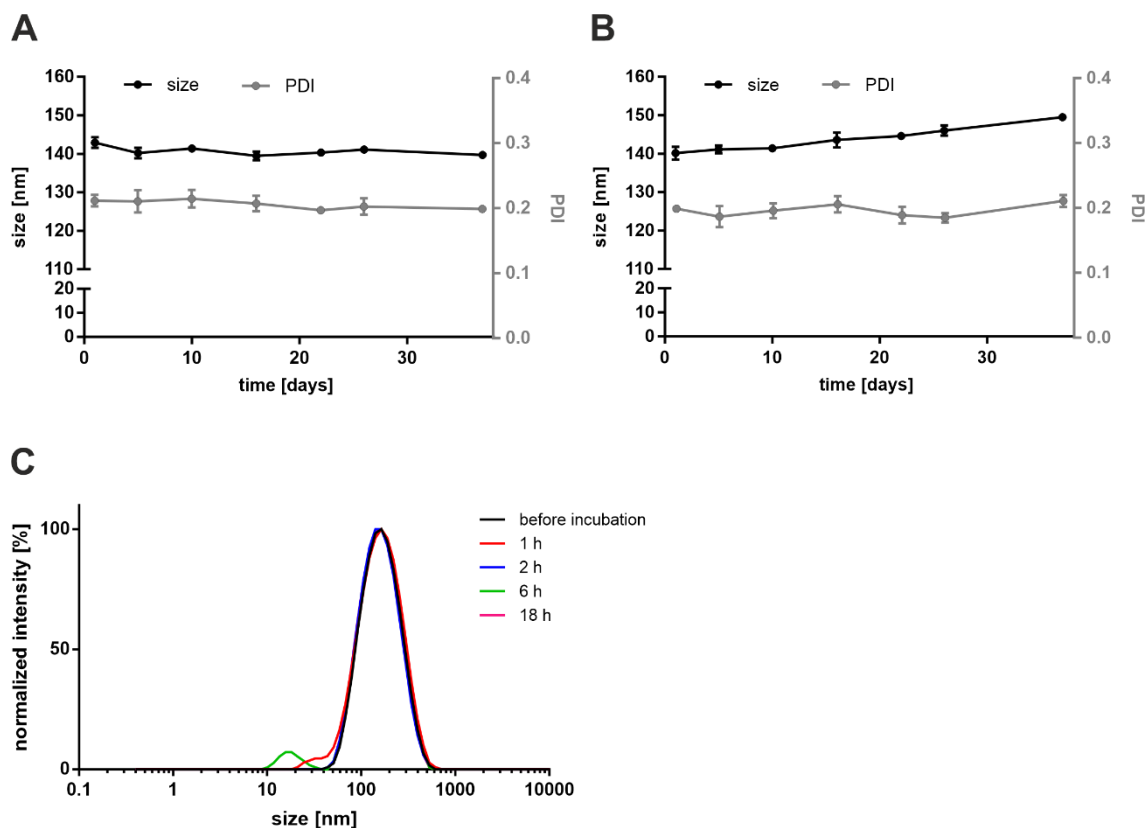
Figure 4. Colloidal stability of OVA NPs. Size and PDI of NPs in 0.1X LT-PBS at (A) 4 °C and (B) room temperature over 37 days. (C) Intensity-weighted size distribution before (black line) and after incubation for 1-18 h (colored lines) in cell culture medium. Intensities were normalized for better comparison. Results represent mean ± SD of n = 3 measurements.

3.3   Serum protein adsorption on OVA NPs

To study the interactions of the OVA NPs with serum proteins, NPs were incubated with 50% FCS and subsequently the OVA NPs were separated from non-adsorbed plasma components by SEC. Then size changes were determined by DLS measurements, the composition of adsorbed proteins was analyzed using SDS-PAGE and the amount of adsorbed proteins was quantified with BCA assay. For all experiments, a PBS control (PBS incubated with 50% FCS followed by SEC) was used to identify proteins that simply co-elute with NPs during SEC. Size measurements, presented in Figure 5A, showed a slight shift of the NP peak to the left when comparing incubated purified NPs (OVA NPs + FCS (SEC)) with non-incubated NPs (OVA NPs - FCS). Additionally, DLS analysis revealed that co-eluted proteins in the PBS control (PBS + FCS (SEC)) were in a size range of 20-6000 nm. Figure 5B shows the silver stained gel of non-incubated NPs

(OVA NPs - FCS), incubated purified NPs (OVA NPs + FCS (SEC)) and PBS control (PBS + FCS (SEC)). For non-incubated OVA NPs, only one band in the sample well corresponding to OVA conjugated to NP surface was visible. For incubated purified OVA NPs, additionally to the band in the sample well, various bands at molecular weights > 70 kDa were detectable, which were also seen for the FCS reference (lane 2). The PBS control displayed a protein band pattern very similar to the incubated OVA NPs. Finally, the amount of proteins on NPs (c = 1 mg/ml) was determined to be 272 µg per mg of non-incubated NPs and 316 µg per mg of incubated purified NPs. The quantity of co-eluted proteins in the PBS control, which was diluted the same as incubated purified NPs, was 44 µg/ml. Thus, protein amount on incubated NPs was equal to the sum of protein amounts of PBS control and non-incubated NPs.
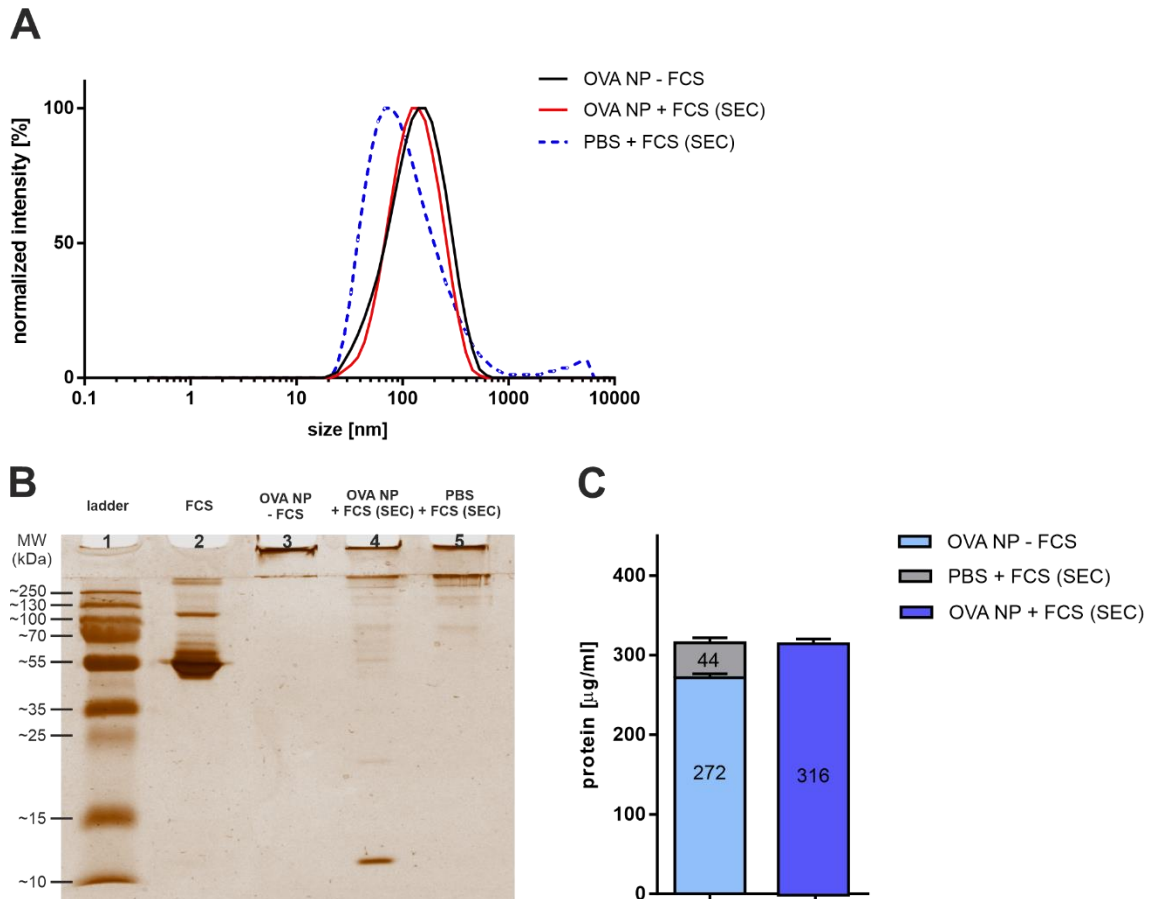
Figure 5. Characterization of adsorbed serum proteins. (A) Normalized intensity-weighted size distribution, (B) silver stained SDS-PAGE gel and (C) proteins levels of non-incubated NPs (OVA NP - FCS), incubated purified NPs (OVA NP + FCS (SEC)), and PBS control (PBS + FCS (SEC)). Results represent mean ± SD of n = 3 measurements.

3.4   Maleimide labelling of proteins

In order to enable the covalent conjugation of proteins lacking free thiols to NPs without requiring prior protein reduction, a simple method was developed in which proteins were labelled with maleimide groups using sulfo-SMCC. Such maleimide-activated proteins can easily be coupled to thiol-decorated NPs *via* a maleimide-thiol reaction, as already described above for the OVA NPs. For method establishment, the number of free thiols in the selected model proteins OVA, HSA and BSA was first quantified using Ellman's assay. As shown in Figure 6A, none of the model proteins contain free thiols, making them suitable for the method. Then the best conditions for maleimide labelling reaction were determined by incubating different amounts of OVA with various molar excesses of sulfo-SMCC for 30 min, 1 h and 2 h, respectively. Generally, lower protein amounts with higher excesses of sulfo-SMCC resulted in higher labelling efficiencies (Figure 6B-E). Additionally, shorter reaction times displayed better results. Overall, the highest amount of maleimide groups per OVA molecule was obtained with 0.5 mg OVA, 50-fold molar excess of sulfo-SMCC, and 30 min reaction time (Figure 6B, left bar). The labelling efficiency was approximately 2-4.5 times higher than for other conditions.
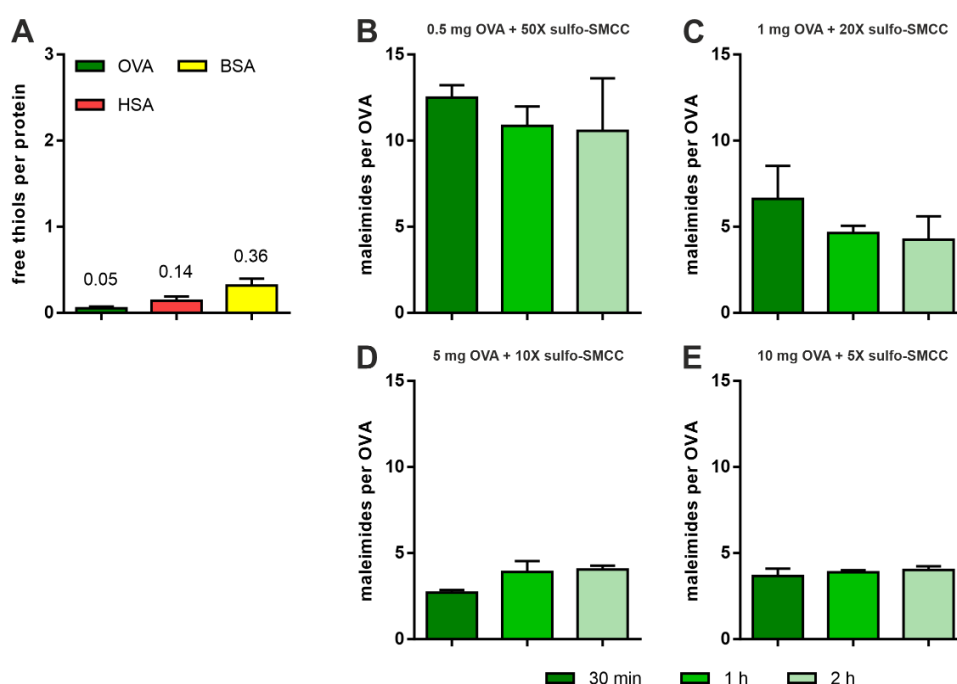
Figure 6. (A) Number of free thiols in model proteins. Maleimide groups per OVA molecule after labelling with sulfo-SMCC using (B) 0.5 mg OVA with a 50-fold molar excess of sulfo-SMCC, (C) 1 mg OVA with a 20-fold molar excess, (D) 5 mg OVA with a 10-fold molar excess and (E) 10 mg OVA with a 5-fold molar excess. Results represent mean ± SD of n = 3 measurements.

Afterwards, the ideal reaction conditions were tested with the selected model proteins and additionally sample purity and protein integrity were analyzed by HPLC. OVA was labelled with approximately 6 maleimide groups per OVA molecule, HSA with 17-18 maleimides per protein and BSA with approximately 19 maleimides per BSA (Figure 7A).
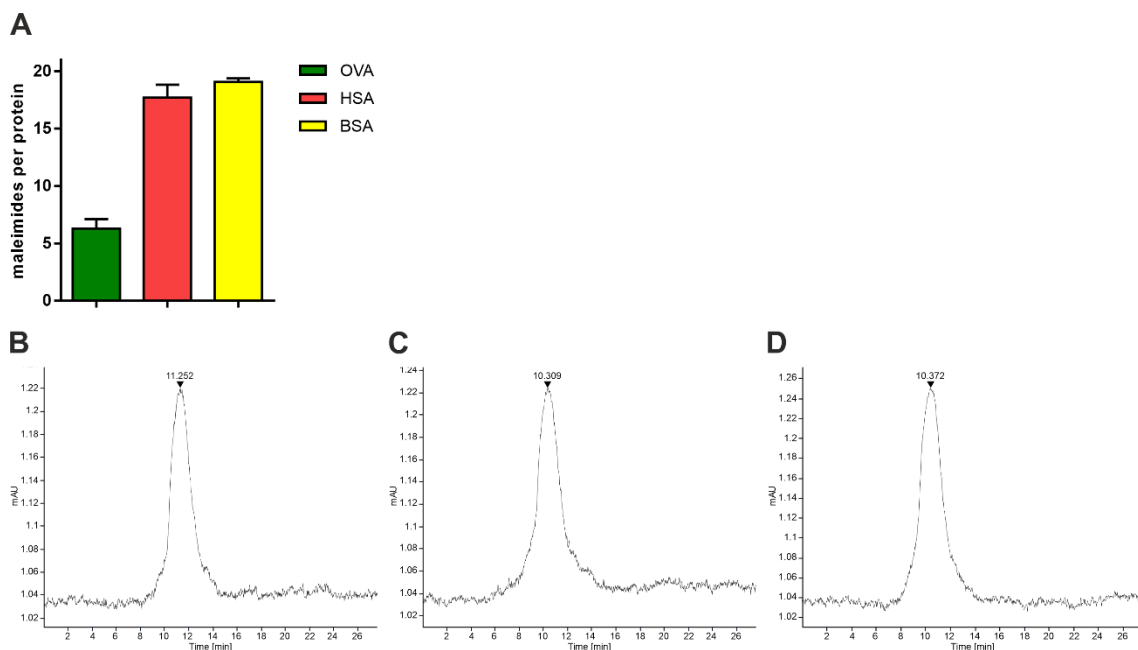

Figure 7. Characteristics of maleimide-labelled proteins. (A) Number of maleimide groups per protein. Representative HPLC chromatograms for (B) Mal-OVA, (C) Mal-HSA and (D) Mal-BSA. Results represent mean ± SD of n = 3 measurements.

HPLC chromatograms (Figure 7B-D) showed almost identical retention times (R_T) for Mal-proteins and freshly dissolved proteins (Table 2). Denatured proteins displayed shorter R_T. Additionally, no peak was detectable at R_T = 14.120 min, corresponding to free sulfo-SMCC. For representative HPLC chromatograms of freshly dissolved proteins and sulfo-SMCC, as well as heat denatured proteins, please refer to supporting information (Figure S1).

Table 2. Retention times of compounds analyzed by HPLC. Results represent mean ± SD of n = 3 runs.

Compound	Retention time [min]
Mal-OVA	11.259 ± 0.005
OVA (freshly dissolved)	11.196 ± 0.046
OVA (heat denatured)	6.885 ± 0.067
Mal-HSA	10.327 ± 0.032
HSA (freshly dissolved)	10.464 ± 0.113
HSA (heat denatured)	7.420 ± 0.154
Mal-BSA	10.401 ± 0.034
BSA (freshly dissolved)	10.473 ± 0.061
BSA (heat denatured)	7.029 ± 0.028
Sulfo-SMCC	14.120 ± 0.067

4 Discussion

The development of well-defined vaccines is of increasing importance in the large field of vaccinations. Many of the traditional vaccines, such as live-attenuated microorganisms, killed whole organisms or split vaccines, have a complex and not well-defined composition [24]. For such complex mixtures, the risk of undesirable side effects, as well as unpredictable and unassignable effects is much higher and they exhibit high batch-to-batch variability. Nanoparticulate vaccines offer the solution here. NPs can be produced in a highly controlled and defined manner and additionally, they are easy to characterize [25, 26]. When developing a NP-based vaccine, it is crucial to establish a robust preparation method resulting in a well-defined product. Furthermore, proper and comprehensive characterization of the particles is mandatory. Besides the structure and the physicochemical properties, the NP stability during storage and under cell culture conditions as well as the possible behavior after *in vivo* administration has to be investigated. This is the only way to create a good knowledge base that enables the subsequent planning of *in vitro* and *in vivo* tests, a prediction of the results and finally the adequate interpretation of them.

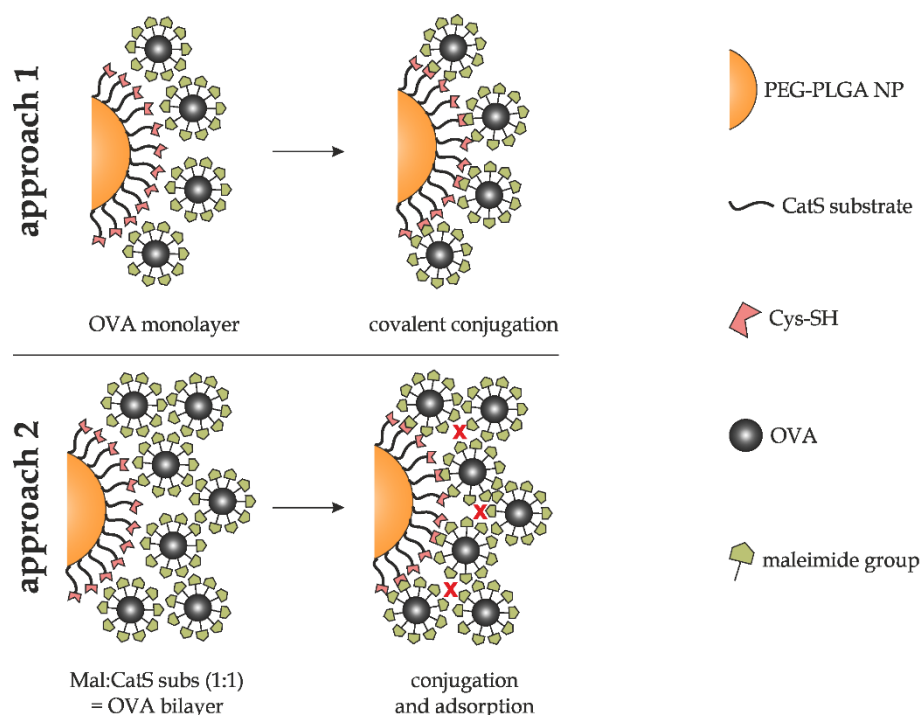## Chapter 3: Development of polymeric nanoparticles

In this study, an antigen delivery platform was developed in which the model antigen OVA was covalently attached to the surface of polymeric NPs. Storage stability of these particles at 4 °C as well as the colloidal stability under cell culture conditions were shown, and it was demonstrated that almost no serum proteins adsorb to the particle surface. Additionally, a work flow with subsequent quality control for the maleimide activation of any protein was elaborated, which allows the application of the conjugation strategy used here for virtually any antigen.

Polymeric NPs composed of block copolymers PEG-PLGA and PLGA were used as particle platform in this study because of their good biocompatibility, biodegradability and non-toxicity [27]. PEG-PLGA was synthesized *via* ring-opening polymerization as this synthesis strategy is highly flexible and well controllable. It is possible to synthesize block copolymers with any desired molecular weight and mass ratio of lactic to glycolic acid [17]. The goal was to prepare a nanoparticulate antigen delivery system that should be stable enough to reach the LNs before degradation to allow interaction with B cells, DCs and other immune cells located in the LNs. In order to create such a stable particle system, it was decided to synthesize PEG-PLGA with a PLGA molecular weight of 13.4 kDa and a 25:75 ratio of glycolic to lactic units [28]. The synthesized block copolymer finally had a molecular weight of 13.1 kDa and a glycolic to lactic unit ratio of 28:72, which closely corresponds to the planned properties and thus demonstrates the well controllable synthesis strategy. Because glycolic acid reacts much faster than lactic acid, it was added continuously, allowing the formation of block copolymers with alternating lactic and glycolic units instead of long lactic and glycolic blocks [17]. Alternating lactic and glycolic units lead to a much slower cleavage of the polymers [29]. Additionally, the higher lactic content of the PLGA block results in a higher particle stability due to slower hydrolysis [30]. Overall, due to these polymer properties, the NPs should be stable enough *in vivo* to reach the LNs prior to degradation.

By using well-known EDC/NHS reaction [31], the block copolymers could be completely functionalized with a cysteine-containing peptide linker. NPs prepared with these linker-functionalized polymers had a thiol-decorated surface allowing for many modification reactions [32]. The hydrophobic NP core was stabilized with additional PLGA in order to improve particle integrity in aqueous media [33].

The thiol surface of the NPs allowed the coupling of maleimide-activated OVA *via* maleimide thiol conjugation [32]. Here, two approaches were tested. Either an OVA amount that could form a monolayer on the particle surface (approach 1) or a 1:1 ratio

of maleimide to CatS subs (approach 2) was used. Size changes assessed by DLS after coupling indicate successful attachment of OVA, as protein attachment affects the size, mass, hydrophobicity and hydration layer of the NPs, all altering Brownian motion [34]. The DLS measurements also showed that the size of the particles was in an ideal range below 200 nm, allowing direct drainage to the LNs [35] and preferential uptake by DCs [36]. SDS-PAGE revealed that when using a 1:1 ratio of maleimide to CatS subs (approach 2), a relatively high amount of OVA was only adsorbed. According to the manufacturer, one Mal-OVA contains 10 maleimide groups. Thus, at the 1:1 ratio, theoretically 10 CatS subs could react with one OVA, which should be sufficient to covalently bind all OVA. However, as adsorbed OVA was found, other factors also seem to play a role. Spatially, the OVA amount used for approach 2 is so high that a bilayer is formed. Since all of the CatS subs thiols are at the same level and the proteins are in a bilayer, the reaction is likely sterically hindered to proceed to completion, as shown in Scheme 1. Obviously, space on NP surface is the limiting factor and thus the OVA amount for maleimide thiol conjugation should not be calculated in a chemical manner with reactants in a 1:1 ratio, but in a spatial manner based on protein size and NP surface.

Scheme 1. Illustration of both approaches used for maleimide thiol conjugation of OVA to NP surface.

The stability studies in PBS revealed that the OVA NPs were stable for over one month when stored at 4 °C. On the other hand, storage stability at room temperature was less good. The colloidal stability of the particles *in vitro* is essential for an effective interaction with the cells, since particle aggregation alters the availability of ligands for binding to uptake receptors and also reduces the internalization rate [37]. It was demonstrated that the OVA NPs were stable under cell culture conditions, thus NP-cell interactions should not be affected.

Adsorption of serum proteins to NP surface can severely alter the functionality of nanoparticulate antigen-delivery systems [38]. Surface binding of antibodies or C3 and C4 fragments may mediate the recognition by innate immune cells. Additionally, protein adsorption largely affects the cellular uptake. Native albumin, Apolipoprotein A4 (ApoA4) or clusterin for example reduce the cellular internalization whereas denatured albumin or Apolipoprotein H (ApoH) enhances binding to uptake receptors of various immune cells. [38] Therefore, investigating whether a protein corona is formed is crucial to estimate the possible impact on NP behavior *in vivo*. Since adsorption of proteins affects the size and mass of NPs, thereby changing their Brownian motion [39], the formation of a protein corona was first evaluated by DLS. The observed decrease in size of the incubated purified OVA NPs (OVA NPs + FCS (SEC)) compared to the non-incubated NPs (OVA NPs - FCS) is probably due to co-eluted proteins and not protein adsorption. As shown with the PBS control (PBS + FCS (SEC)), the co-eluted proteins had a mean size of ~70 nm. These small co-eluted proteins also affect the size distribution of the incubated purified OVA NPs, presumably leading to the reduced mean size. Characterization of the composition of the adsorbed proteins by SDS-PAGE revealed that the protein signature of the incubated purified OVA NPs (OVA NPs + FCS (SEC)) was very similar to that of the PBS control (PBS + FCS (SEC)), indicating that the proteins detected were co-eluted rather than adsorbed. That was confirmed by BCA assay as the determined amount of proteins on the incubated purified OVA NPs was equal to the sum of the amount of co-eluted proteins in the PBS control and the protein amount on non-incubated OVA NPs. Since the silver stained gel showed some very light additional bands for the incubated OVA NPs, a few proteins were probably adsorbed anyway. Overall, however, the OVA NPs showed a negligible protein corona, consistent with previous studies that showed reduced protein adsorption on particles decorated with proteins [40] or PEG [41] on the surface. This indicates that the particles do not change their appearance after being introduced into the body. Their behavior *in vivo* and the

interaction with immune cells is therefore unaffected and is solely due to the determined particle characteristics and not to any protein corona.

Finally, a method including quality control was developed that enables the covalent attachment of any protein to NPs without the need to reduce the protein. The rationale for this method development was that most proteins do not contain freely available thiols, although these are very attractive to use for coupling proteins to materials, surfaces or NPs. A lot of well-known conjugation reactions exploiting sulfhydryl groups are described in the literature [32]. However, in the most proteins, the thiols are either inaccessible due to protein folding or are involved in intra- and intermolecular disulfide bonds and thus not available for reactions [14]. This lack of free thiols was confirmed for the chosen model proteins BSA, HSA and OVA. Proteins are therefore often reduced to generate free thiols. Protein reduction, even with mild reducing agents, always bears the risk of protein denaturation [16] resulting in loss of protein integrity and functionality, which in turn alters antigenicity [42, 43]. Additionally, the native form of the protein antigens is crucial for interaction with B cells [6]. Therefore, to avoid the reduction and the associated risk of denaturation, it was decided to use the popular and well-studied maleimide thiol reaction, but in reverse order. Typically, cysteine groups of protein antigens are coupled to maleimide-activated NPs [32, 44]. Here, however, maleimide-labelled proteins were conjugated to sulfhydryl-bearing NPs. Maleimide-activated proteins are already used for peptide-carrier protein conjugations [45, 46]. For example, for OVA, BSA and keyhole limpet hemocyanin (KLH), which are typical carrier proteins, maleimide-activated forms are commercially purchasable, but nothing is available on the market for other proteins, not even kits for maleimide labelling. However, since this coupling technique could be of interest for a variety of protein antigens to allow conjugation in their native form, a method including quality control assays applicable for any protein was developed. The method is based on the coupling of sulfo-SMCC to amine groups that are ubiquitously present in proteins, whereby they are maleimide-labelled [47]. Testing different reaction parameters revealed that a higher excess of sulfo-SMCC led to a higher number of maleimides per proteins and that longer incubation times were detrimental to labelling efficiency, probably because the maleimide groups hydrolyze with time in the aqueous reaction medium [48]. As demonstrated by the labelling of OVA, BSA and HSA, the optimized reaction conditions resulted in labelling efficiencies similar to commercially available products, which are 5-15 maleimides per OVA and 15-20 maleimides per BSA [49]. Since HSA is very similar to BSA [50], 15-20 maleimides per HSA can be considered ideal. Finally, HPLC analysis completed the

method procedure by confirming the native form of the proteins after the reaction as evidenced by the almost identical R_T of the Mal-proteins and freshly dissolved proteins. Additionally, the absence of sulfo-SMCC peak proved successful purification of the proteins. By using this protocol it is possible to couple any protein antigen to NPs in a very mild manner without the need for protein reduction and the associated risk of denaturation.

5 Conclusion

In summary, in this study a polymeric NP-based vaccine with antigens covalently coupled to the surface were developed. Extensive characterizations provided information about size, structure and composition and also revealed a good storage stability and neglectable protein corona formation. In addition, a protocol suitable for easy and mild conjugation of any protein to NPs was established. Since the developed NPs carry the antigens on the surface and are virus-sized, they offer the possibility to interact with DCs, leading to T cell activation, and also with B cells. Thus, these particles have the potential to act as a universal vaccine. This study represents the first step in the development of a new nanoparticulate antigen delivery system. However, the nature and strength of the immune response induced by the NPs has yet to be tested in subsequent *in vitro* and *in vivo* tests.

References

1. Mi-Gyeong K, Joo Yeon P, Yuna Shon, Gunwoo K, Gayong S, Yu-Kyoung Oh. Nanotechnology and vaccine development. *Asian Journal of Pharmaceutical Sciences*. 2014; 9: 227–235.

2. Diaz-Arévalo D, Zeng M. Nanoparticle-based vaccines: opportunities and limitations. *Nanopharmaceuticals*. 2020: 135–150.

3. Vu MN, Kelly HG, Kent SJ, Wheatley AK. Current and future nanoparticle vaccines for COVID-19. *EBioMedicine*. 2021; 74: 103699.

4. Slütter B, Jiskoot W. Sizing the optimal dimensions of a vaccine delivery system: a particulate matter. *Expert Opin Drug Deliv*. 2016; 13: 167–170.

5. Zhao L, Seth A, Wibowo N, et al. Nanoparticle vaccines. *Vaccine*. 2014; 32: 327–337.

6. Bachmann MF, Jennings GT. Vaccine delivery: A matter of size, geometry, kinetics and molecular patterns. *Nat Rev Immunol*. 2010; 10: 787–796.

7. Roth GA, Picece VCTM, Ou BS, Luo W, Pulendran B, Appel EA. Designing spatial and temporal control of vaccine responses. *Nat Rev Mater*. 2021: 1–22.

8. Kelly HG, Kent SJ, Wheatley AK. Immunological basis for enhanced immunity of nanoparticle vaccines. *Expert Rev Vaccines*. 2019; 18: 269–280.

9. Sahdev P, Ochyl LJ, Moon JJ. Biomaterials for nanoparticle vaccine delivery systems. *Pharm Res*. 2014; 31: 2563–2582.

10. Mao HH, Chao S. Advances in Vaccines. *Adv Biochem Eng Biotechnol*. 2020; 171: 155–188.

11. Chattopadhyay S, Chen J-Y, Chen H-W, Hu C-MJ. Nanoparticle Vaccines Adopting Virus-like Features for Enhanced Immune Potentiation. *Nanotheranostics*. 2017; 1: 244–260.

12. Lung P, Yang J, Li Q. Nanoparticle formulated vaccines: opportunities and challenges. *Nanoscale*. 2020; 12: 5746–5763.

13. Pati R, Shevtsov M, Sonawane A. Nanoparticle Vaccines Against Infectious Diseases. *Front Immunol*. 2018; 9: 2224.

14. Lu L, Duong VT, Shalash AO, Skwarczynski M, Toth I. Chemical Conjugation Strategies for the Development of Protein-Based Subunit Nanovaccines. *Vaccines (Basel)*. 2021; 9.

15. Kim Y, Ho SO, Gassman NR, et al. Efficient site-specific labeling of proteins via cysteines. *Bioconjug Chem*. 2008; 19: 786–791.

16. Ho JGS, Middelberg APJ, Ramage P, Kocher HP. The likelihood of aggregation during protein renaturation can be assessed using the second virial coefficient. *Protein Sci*. 2003; 12: 708–716.

17. Qian H, Wohl AR, Crow JT, Macosko CW, Hoye TR. A Strategy for Control of "Random" Copolymerization of Lactide and Glycolide: Application to Synthesis of PEG-b-PLGA Block Polymers Having Narrow Dispersity. *Macromolecules*. 2011; 44: 7132–7140.

18. Childs CE. The determination of polyethylene glycol in gamma globulin solutions. *Microchemical Journal*. 1975; 20: 190–192.

19. Abstiens K, Gregoritza M, Goepferich AM. Ligand Density and Linker Length are Critical Factors for Multivalent Nanoparticle-Receptor Interactions. *ACS Appl Mater Interfaces*. 2019; 11: 1311–1320.

20. Wen C-Y, Tang M, Hu J, et al. Determination of the Absolute Number Concentration of Nanoparticles and the Active Affinity Sites on Their Surfaces. *Anal Chem*. 2016; 88: 10134–10142.

21. Gholizadeh S, Kamps JAAM, Hennink WE, Kok RJ. PLGA-PEG nanoparticles for targeted delivery of the mTOR/PI3kinase inhibitor dactolisib to inflamed endothelium. *Int J Pharm*. 2018; 548: 747–758.

22. Kurfürst MM. Detection and molecular weight determination of polyethylene glycol-modified hirudin by staining after sodium dodecyl sulfate-polyacrylamide gel electrophoresis. *Analytical Biochemistry*. 1992; 200: 244–248.

23. Johnson M. Fetal Bovine Serum. *MATER METHODS*. 2012; 2.

24. Wen EP, ed. *Vaccine development and manufacturing*. Hoboken, New Jersey: Wiley; 2015.

25. Khan I, Saeed K, Khan I. Nanoparticles: Properties, applications and toxicities. *Arabian Journal of Chemistry*. 2019; 12: 908–931.

26. Mourdikoudis S, Pallares RM, Thanh NTK. Characterization techniques for nanoparticles: comparison and complementarity upon studying nanoparticle properties. *Nanoscale*. 2018; 10: 12871–12934.

27. Rocha CV, Gonçalves V, da Silva MC, Bañobre-López M, Gallo J. PLGA-Based Composites for Various Biomedical Applications. *Int J Mol Sci*. 2022; 23.

28. Makadia HK, Siegel SJ. Poly Lactic-co-Glycolic Acid (PLGA) as Biodegradable Controlled Drug Delivery Carrier. *Polymers (Basel)*. 2011; 3: 1377–1397.

29. Li J, Stayshich RM, Meyer TY. Exploiting sequence to control the hydrolysis behavior of biodegradable PLGA copolymers. *J Am Chem Soc*. 2011; 133: 6910–6913.

30. Keles H, Naylor A, Clegg F, Sammon C. Investigation of factors influencing the hydrolytic degradation of single PLGA microparticles. *Polymer Degradation and Stability*. 2015; 119: 228–241.

31. Maslanka Figueroa S, Fleischmann D, Beck S, Goepferich A. The Effect of Ligand Mobility on the Cellular Interaction of Multivalent Nanoparticles. *Macromol Biosci*. 2020; 20: e1900427.

32. Hermanson GT. *Bioconjugate techniques*. Amsterdam: Academic Press; 2008.

33. Owen SC, Chan DPY, Shoichet MS. Polymeric micelle stability. *Nano Today*. 2012; 7: 53–65.

34. Malvern Instruments Ltd. Dynamic Light Scattering: An Introduction in 30 Minutes. Available at https://warwick.ac.uk/fac/cross_fac/sciencecity/programmes/internal/themes/am2/booking/particlesize/intro_to_dls.pdf.

35. Manolova V, Flace A, Bauer M, Schwarz K, Saudan P, Bachmann MF. Nanoparticles target distinct dendritic cell populations according to their size. *Eur J Immunol*. 2008; 38: 1404–1413.

36. Xiang SD, Scholzen A, Minigo G, et al. Pathogen recognition and development of particulate vaccines: does size matter? *Methods*. 2006; 40: 1–9.

37. Forest V, Pourchez J. Preferential binding of positive nanoparticles on cell membranes is due to electrostatic interactions: A too simplistic explanation that does not take into account the nanoparticle protein corona. *Mater Sci Eng C Mater Biol Appl*. 2017; 70: 889–896.

38. Bros M, Nuhn L, Simon J, et al. The Protein Corona as a Confounding Variable of Nanoparticle-Mediated Targeted Vaccine Delivery. *Front Immunol*. 2018; 9: 1760.

39. Carrillo-Carrion C, Carril M, Parak WJ. Techniques for the experimental investigation of the protein corona. *Curr Opin Biotechnol*. 2017; 46: 106–113.

40. Oh JY, Kim HS, Palanikumar L, et al. Cloaking nanoparticles with protein corona shield for targeted drug delivery. *Nat Commun*. 2018; 9: 4548.

41. Alberg I, Kramer S, Schinnerer M, et al. Polymeric Nanoparticles with Neglectable Protein Corona. *Small*. 2020; 16: e1907574.

42. Greenfield EA, DeCaprio J, Brahmandam M. Making Weak Antigens Strong: Modifying Protein Antigens by Denaturation. *Cold Spring Harb Protoc*. 2018; 2018.

43. Peränen J, Rikkonen M, Kääriäinen L. A method for exposing hidden antigenic sites in paraformaldehyde-fixed cultured cells, applied to initially unreactive antibodies. *J Histochem Cytochem*. 1993; 41: 447–454.

44. Martínez-Jothar L, Doulkeridou S, Schiffelers RM, et al. Insights into maleimide-thiol conjugation chemistry: Conditions for efficient surface functionalization of nanoparticles for receptor targeting. *J Control Release*. 2018; 282: 101–109.

45. Abbas IM, Schwaar T, Bienwald F, Weller MG. Predictable Peptide Conjugation Ratios by Activation of Proteins with Succinimidyl Iodoacetate (SIA). *Methods Protoc*. 2017; 1.

46. Carter JM. Conjugation of Peptide to Carrier Proteins via m-Maleimidobenzoyl-N-Hydroxysuccinimide Ester (MBS). In: Walker JM, ed. *The Protein Protocols Handbook*. Totowa, NJ: Humana Press; 1996: 689–692.

47. Thermo Fisher Scientific Inc. Instructions SMCC and Sulfo-SMCC. Available at https://fnkprddata.blob.core.windows.net/domestic/data/datasheet/PCC/22360.pdf.

48. Flügel S. *Oligodeoxynucleotide-Polypeptide Block Copolymers*. Dissertation. Mainz: Johannes Gutenberg-Universität; 2010.

49. Thermo Fisher Scientific Inc. Instructions Imject Maleimide Activated BSA and OVA. Available at https://assets.fishersci.com/TFS-Assets/LSG/manuals/MAN0011185_Imject_Maleimide_Activ_BSA_OVA_UG.pdf .

50. Szekeres GP, Kneipp J. Different binding sites of serum albumins in the protein corona of gold nanoparticles. *Analyst*. 2018; 143: 6061–6068.

Chapter 3 – Supporting Information

Development of polymeric nanoparticles

with covalently attached antigens

1   Polymer characterization

Molecular weight of HOOC-PEG-PLGA and mass ratio of lactic to glycolic units were calculated based on the integration values of methyl, methine and methylene signals of lactic, glycolic and PEG units and the molecular weight of PEG (provided by the manufacturer) [1].

The molecular weight of HOOC-PEG$_{5k}$ provided by the manufacturer was 5085 Da. Based on the fact that a PEG monomer unit has a molecular weight of 44.05 Da, the number of PEG monomer units per PEG chain was calculated as follows:

$$PEG\ units/_{PEG\ chain} = 5085\ Da/_{44.05\ Da} = 115.43$$

Each repeating PEG monomer contains four protons, therefore the number of protons per PEG chain was calculated using the following equation:

$$protons/_{PEG\ chain} = 115.43 \times 4 = 461.75$$

After amplifying the integral of the methylene signal of PEG chain to 461.75, the integral of the methine signal of lactic units was 125.25, the methyl signal of lactic units was 412.72 and the methylene signal of glycolic units was 124.33.

Since three protons contribute to the methyl signal, one proton to the methine signal and two protons to the methylene signal, the number of lactic and glycolic monomer units was calculated as follows:

$$lactic\ units_{methyl\ signal} = 412.72 \div 3 = 137.57$$

$$lactic\ units_{methine\ signal} = 125.25$$

$$lactic\ units = \frac{137.57 + 125.25}{2} = 131.41$$

$$glycolic\ units = 124.33 \div 2 = 62.17$$

Based on the fact that a lactide unit has a molecular weight of 72.06 Da and a glycolide unit has a molecular weight of 58.04 Da, the molecular weight of lactic units (LA) and glycolic units (GA) was calculated as follows:

$$M_n(LA) = 131.41 \times 72.06\ Da = 9469.40\ Da$$

$$M_n(GA) = 62.17 \times 58.04\ Da = 3608.35\ Da$$

Thus, molecular weight of poly(lactic-co-glycolic acid) (PLGA) and mass ratio of lactic to glycolic units was:

$$M_n(PLGA) = 9469.40\ Da + 3608.35\ Da = 13077.75\ Da$$

$$LA/GA = {9469.40\ Da}/{3608.35\ Da} \approx {72}/{28}$$

Overall molecular weight of HOOC-PEG$_{5k}$PLGA$_{13k}$ was:

$$M_n(PLGA) = 13077.75\ Da + 5085\ Da = 18162.75\ Da$$

2   Maleimide labelling of proteins
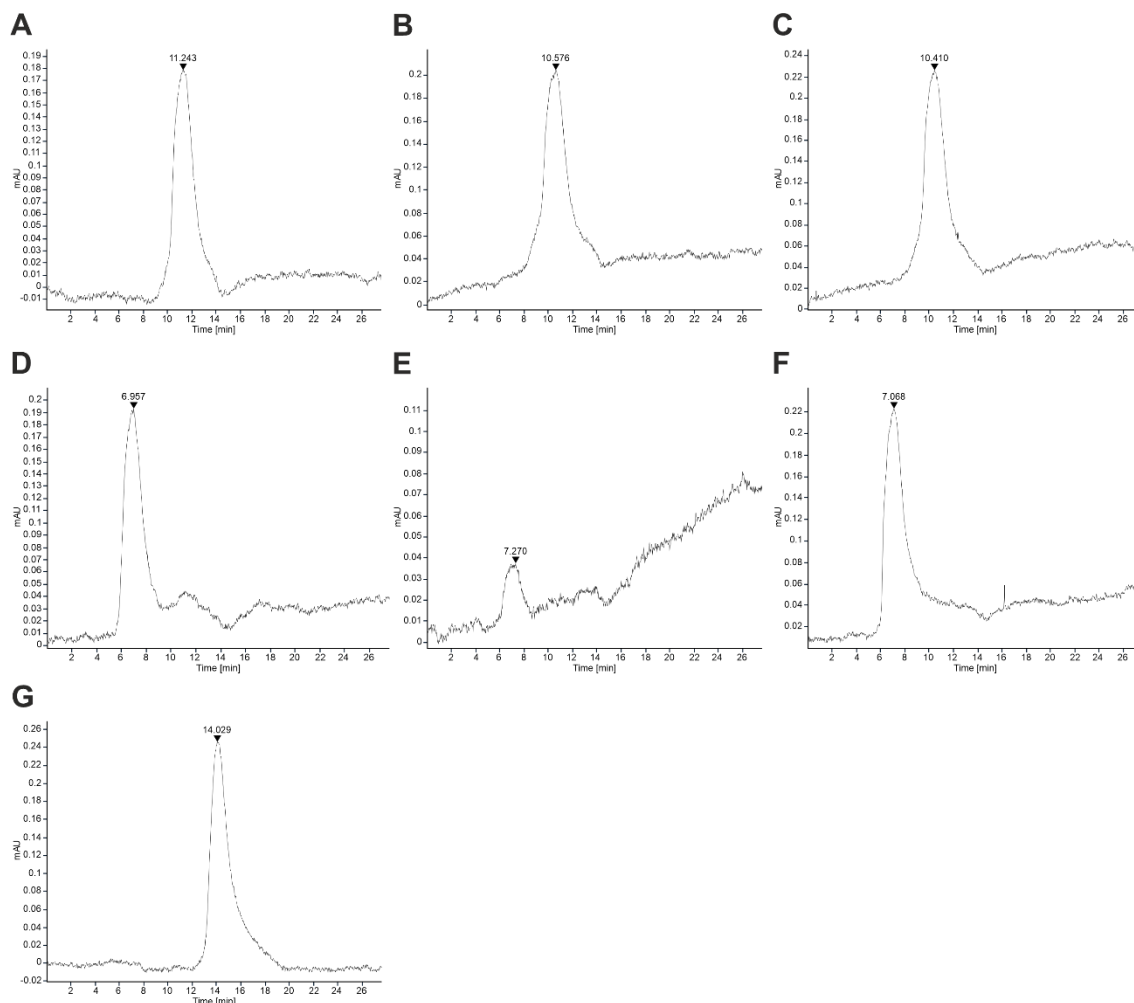
Figure S1. Representative HPLC chromatograms of freshly dissolved (A) OVA, (B) HSA and (C) BSA, respectively, and heat denatured (D) OVA, (E) HSA and (F) BSA, respectively, as well as (G) freshly dissolved sulfo-SMCC.

3   References

1.   Qian H, Wohl AR, Crow JT, Macosko CW, Hoye TR. A Strategy for Control of "Random" Copolymerization of Lactide and Glycolide: Application to Synthesis of PEG-b-PLGA Block Polymers Having Narrow Dispersity. *Macromolecules*. 2011; 44: 7132–7140.

Chapter 4

Enzyme-triggered antigen release enhances cross-presentation by dendritic cells

Abstract

Nanoparticles hold great potential as vaccine carriers due to their highly versatile structure and the possibility to influence intracellular trafficking and antigen presentation by their design. In this study, we developed a nanoparticulate system with a new enzyme-triggered antigen release mechanism. For this novel approach, nanoparticle and model antigen ovalbumin were linked with a substrate of the early endosomal protease cathepsin S. This construct enabled the transfer of antigens delivered to bone marrow-derived dendritic cells from the endo-lysosomal compartments in the cytosol. Consecutively, our particles enhanced cross-presentation on dendritic cells and subsequently promoted a stronger activation of CD8+ T cells. Our findings suggest that enzyme-triggered antigen release allows the endosomal escape of the antigen, leading to increased MHC-I presentation. Since T cell immunity is central for the control of viral infections and cancer, this release mechanism offers a promising approach for the development of both prophylactic and therapeutic vaccines.

1   Introduction

According to the World Health Organization (WHO), vaccines against more than 20 infectious diseases are currently available [1]. Vaccinations enable control or even eradication of infectious diseases and thus not only reduce healthcare costs but also potently save human lives [2]. Additionally, therapeutic cancer vaccines are a rapidly emerging field of immunotherapy, as reflected by the immense number of ongoing clinical trials in that sector [3]. In the broad field of vaccination technologies available, nanoparticles (NPs) hold great potential as antigen delivery platforms as they can be manufactured in various designs [4, 5]. Antigens are either conjugated to the surface of NPs or encapsulated into their core [6]. Additionally, adjuvants like toll-like receptor (TLR) agonists or ligands targeting immune cells can be integrated. Importantly, NPs can act as self-adjuvants and can be targeted to lymph nodes by controlling their size [5]. Furthermore, numerous materials used in nanoparticle production are biocompatible, biodegradable and non-toxic. In addition, most of these materials have already been approved [7]. The success of vaccines against cancer and intracellular pathogens is highly dependent on adequate presentation of vaccine antigens on MHC-I by antigen-presenting cells (APCs) and subsequent induction of cytotoxic T cells [8, 9]; however, despite the rapid advances in vaccine research in recent years, problems prevail [10].

Extracellularly delivered antigens, like those found in protein-based vaccines, are internalized and processed by APCs. Processed antigens are then loaded onto MHC-II molecules, thus activating CD4$^+$ T helper cells [11, 12]. In contrast, cytoplasmatic antigens, as occurring during viral infections, are presented to CD8$^+$ cytotoxic T cells by MHC-I molecules [11, 12]. However, dendritic cells (DCs) are also able to present exogenous antigens on MHC-I to CD8$^+$ T cells, a mechanism termed as cross-presentation. In cross-presentation, two pathways after cellular antigen uptake exist. Antigen export from endosomes into the cytosol, followed by proteasomal degradation and antigen loading on MHC-I molecules in the endoplasmic reticulum or endosomes is called cytosolic pathway. The other possible route is the vacuolar pathway where both, antigen degradation and MHC-I loading, occur in endosomes [13]. For nanoparticle-based vaccines, different mechanisms – such as proton sponge effect [14], membrane fusion [15] or reduction-sensitive mechanisms [16] – have been described to enhance antigen cross-presentation by leading to endosomal escape of antigen followed by cytosolic cross-presentation pathway [17].

In this study, we developed a nanoparticulate antigen delivery system with an enzymatically triggered antigen release that represents a novel enzyme-sensitive mechanism to enhance cross-presentation. We decided to use a substrate of the protease cathepsin S (CatS) as linker between nanoparticles and antigens. Cathepsins are the most common lysosomal proteases, found in endosomal and lysosomal compartments of various cells throughout the body [18, 19]. Despite this ubiquitous occurrence of cathepsins, CatS is known to be one of the few enzymes active in the early endosome of dendritic cells [20, 21], and thus offers ideal properties to mediate a selective antigen release in the early endosome. This enzymatic antigen release leads to increased availability of free antigen in the early endosome, allowing for endosomal escape and subsequent cytosolic cross-presentation pathway. To this end, we coupled the antigen to the nanoparticle surface *via* a specific substrate for early endosomal protease CatS, discovered by Lützner *et al.* [22]. After verifying the non-cytotoxicity, purity and DC uptake of the particle system, we studied the intracellular trafficking and the type of antigen presentation compared to a system with a stable linker.

2 Materials and Methods

2.1 Materials

All materials and reagents were purchased from Sigma Aldrich (Taufkirchen, Germany) unless otherwise stated.

2.2 Cells and mice

Bone marrow-derived dendritic cells (BMDCs) were generated following a protocol described by Lutz *et al.* [23] and harvested on day 7. Tibias and femurs were isolated from male C57BL/6J mice kept under specific pathogen-free conditions (University Hospital Regensburg, Germany).

Naïve CD8^{+} T cells with an OVA-specific T cell receptor were isolated from spleen and lymph node cells from male OTI mice (Charles River Laboratories, France) using naïve CD8a^{+} T cell isolation kit (Miltenyi Biotec, Bergisch Gladbach, Germany), following manufacturer's instructions.

2.3   Polymer synthesis and nanoparticle preparation

HOOC-PEG$_{5k}$-PLGA$_{13.1k}$ block copolymer was synthesized after Qian *et al.* [24] with slight modifications as described in supplementary materials. ^{1}H-NMR spectrum is shown in Supplementary Figure S1.

To synthesize cathepsin S substrate-PEG-PLGA, cathepsin S substrate (CatS subs; amino acid sequence GRKWPPMGLPWEC-DArg-NH$_2$, customer synthesis Genscript, Piscataway, NJ, USA) was covalently coupled *via* its lysine residue to HOOC-PEG$_{5k}$-PLGA$_{13.1k}$ using ethyl-3-(3-dimethylaminopropyl)carbodiimide/N-hydroxysuccinimide (EDC/NHS) chemistry. Please refer to supplementary methods for detailed description of the coupling reaction.

NPs were prepared using nanoprecipitation. In brief, CatS subs-PEG-PLGA and Resomer® RG 752 H (PLGA) were dissolved in acetonitrile (10 mg/ml) and mixed at a ratio of 7:3 (m/m). Afterwards, polymer mixture (200 µl) was added dropwise into 2 ml 0.1X low-endotoxin Dulbecco's phosphate-buffered saline (LT-PBS) while stirring. Immediately after preparation, 2 ml 0.1X LT-PBS was added and particles were washed and concentrated by ultracentrifugation with an Amicon® Ultra-15 MWCO 100 kDa centrifugal filter (Merck KGaA, Darmstadt, Germany) at 1400 *g*.

For visualization of NPs *in vitro*, core component PLGA was labelled with CF™647, a cyanine-based far-red fluorescent dye, as described before [25].

Ovalbumin (OVA) was covalently coupled to CatS substrate on particle surface using maleimide thiol chemistry. Immediately after nanoparticle preparation, CatS subs NPs were incubated for 2 h with a 50-fold molar excess of tris(2-carboxyethyl)phosphine (Carl Roth GmbH, Karlsruhe, Germany) relative to CatS substrate. Subsequently, Imject™ maleimide activated OVA (Mal-OVA; Thermo Fisher Scientific, Waltham, MA, USA) was added and gently stirred for 4 h at room temperature. The amount of OVA added was calculated based on nanoparticle surface area and protein size (please refer to supplementary methods for detailed explanation of calculation). Unbound OVA was removed through washing the NPs with 0.1X LT-PBS and ultracentrifugation as described above.

For antigen detection *in vitro*, OVA was labelled with Alexa Fluor™ 647 NHS Ester (Thermo Fisher Scientific, Waltham, MA, USA), following the manufacturer's instructions.

To minimize the risk of endotoxin contamination, nanoparticle preparation and protein conjugation were performed in a LAF box, glassware was depyrogenated at 250 °C and LT-PBS and water for injection (B. Braun, Melsungen, Germany) were used [26].

2.4   Nanoparticle characterization

Zeta potential, evaluated by diffusion barrier method [27], hydrodynamic diameter and polydispersity index (PDI) of all NP formulations were determined in 0.1X LT-PBS at 25 °C using a Malvern ZetaSizer Nano ZS (Malvern Instruments GmbH, Lappersdorf, Germany).

The amounts of CatS substrate and OVA on NP surface were assessed with a Pierce™ BCA protein assay kit (Thermo Fisher Scientific, Waltham, MA, USA), using CatS substrate and OVA as standards, following the manufacturer's instructions. Protein amount was calculated by subtracting the absorbance of CatS subs NPs from that of OVA NPs.

To verify the covalent attachment of OVA to the particle surface, a sodium dodecyl sulfate (SDS)-polyacrylamide gel electrophoresis (PAGE) was performed. Protein bands were detected by Coomassie or silver staining and NPs were visualized by barium iodide staining [28].

2.5   CatS substrate cleavage assay

In order to confirm the cleavability of the designed CatS substrate by CatS, a cleavage assay was performed using recombinant mouse CatS (Sino Biological Europe GmbH, Eschborn, Germany) and Dabcyl-GRKWPPMGLPWEC-DArg-Glu(EDANS) (FRET-CatS substrate; customer synthesis Genscript, Piscataway, NJ, USA), an internally quenched peptide substrate. NPs were prepared in the same manner as non-labelled NPs. For the cleavage assay CatS was diluted with assay buffer (50 mM potassium phosphate buffer pH 6.5, 50 mM NaCl, 0.5 mM DTT, 2 mM EDTA, 0.01% Triton X-100) to a final concentration of 8 µg/ml and 20 µl was placed in a Corning® 384-well, black, nonbinding surface microplate (Corning Inc., Corning, NY, USA). After 15 min pre-incubation at 37 °C, pre-warmed FRET-CatS substrate, FRET-CatS substrate NP or FRET-OVA NP solutions diluted in assay buffer were added (final substrate concentration 40 µM). To inhibit enzyme activity, CatS was pre-incubated with 10 µM E-64.

Fluorescence increase as a function of time was recorded at 37 °C (λ_{ex}=340 nm, λ_{em}=485 nm).

2.6   *In vitro* BMDC activation assay

To evaluate the potential of NPs to stimulate dendritic cells, BMDCs were incubated for 5 h in a 96-well plate (Corning Inc., Corning, NY, USA) at a density of 3×10^5 cells/well. NP solutions, adjusted to a final OVA concentration of 50 µg/ml, were added to the cells and incubated for 18 h at 37 °C. 0.1X LT-PBS and lipopolysaccharide (LPS; 1.5 µg/ml) were used as negative and positive control, respectively. Cells were stained with anti-CD11c-FITC, anti-CD40-APC, anti-CD80-APC and anti-CD86-APC antibodies (Miltenyi Biotec, Bergisch Gladbach, Germany) according to the manufacturer's instructions, and analyzed with a BD FACSCanto™ II (BD, Heidelberg, Germany). Isotype-matched control antibodies were used, and viability was determined by propidium iodide staining (500 ng/ml).

2.7   *In vitro* NP uptake in BMDCs

For qualitative uptake studies, BMDCs stained with CellTracker™ green (CTG) dye (Thermo Fisher Scientific, Waltham, MA, USA) were seeded at 3×10^5 cells/well into 8-well µ-slides (Ibidi GmbH, Planegg, Germany) and cultured for 2 h. NPs (OVA concentration 50 µg/ml) and ODN1826 (63 ng/ml; Eurofins Genomics, Ebersberg, Germany) were added. After 2 h, cells were fixed with 4% paraformaldehyde (PFA) and cell nuclei were stained with 4',6-diamidine-2'-phenylindole dihydrochloride (DAPI; 10 µg/ml in DPBS) prior to imaging using a Zeiss LSM 710 (Carl Zeiss Microscopy GmbH, Jena, Germany).

To quantify NP uptake, BMDCs were seeded at a density of 3×10^5 cells/well in a 96-well plate and treated as described for confocal laser scanning microscopy (CLSM) uptake analysis. Cells were additionally labelled with anti-CD11c-FITC and analyzed by flow cytometry as described above.

2.8   Intracellular antigen localization

Intracellular trafficking of OVA was examined by CLSM. In order to investigate differences in antigen localization due to enzymatic antigen release, control NPs with a non-cleavable stable linker (stL) were prepared (please refer to supplementary materials for detailed description). $3x10^5$ BMDCs were seeded per well in 8-well µ-slides. Cells were incubated for 2 h before NPs (OVA concentration 50 µg/ml) and ODN1826 (63 ng/ml) were added. For EEA1 staining, NPs were removed after 2-hour incubation and cells were fixed using 4% PFA. Samples were blocked with 0.1 M phosphate buffer + 2% bovine serum albumin (BSA) + 0.3% Triton X-100 for 1 h prior to incubation with anti-EEA1 primary antibody (clone C45B10, Cell Signaling, Danvers, MA, USA) overnight at 4 °C. After incubation with F(ab')2-goat anti-rabbit IgG secondary antibody Alexa Fluor 488 (Thermo Fisher Scientific, Waltham, MA, USA) for 1 h, cell nuclei were stained with DAPI (10 µg/ml in DPBS). For Lysotracker imaging, LysoTracker™ Green DND-26 (LTG; 5 µM; Thermo Fisher Scientific, Waltham, MA, USA) was added together with the NP solutions. After a 2-hour incubation period, nuclei were stained with Hoechst 33258 (10 µg/ml in LT-PBS; Polysciences Inc., Warrington, PA, USA). Images were acquired using a Zeiss LSM 710 and Manders' Colocalization Coefficient was determined using ZEN software 2008 (Carl Zeiss Microscopy GmbH, Jena, Germany) [29].

2.9   *In vitro* cross-presentation assay

To evaluate cross-presentation of OVA by BMDCs, co-culture experiments with naïve CD8+ T cells from OTI mice were performed. BMDCs were seeded at a density of $3x10^4$ cells/well in a 96-well plate and incubated for 5 h. Then, BMDCs were stimulated with NPs (OVA concentration 50 µg/ml) and ODN1826 (63 ng/ml). After incubation for 18 h, $1x10^5$ naïve CD8+ T cells were added. 5 days later T cells were harvested, stained with anti-CD8a-VioBlue, anti-CD3-APC (Miltenyi Biotec, Bergisch Gladbach, Germany) and anti-CD44-FITC (Becton Dickinson, Franklin Lakes, NJ, USA) and analyzed using a BD FACSCanto™ II (BD, Heidelberg, Germany). 7-AAD (500 ng/ml; Thermo Fisher Scientific, Waltham, MA, USA) was used for viability staining.

2.10 Statistics

Statistical analysis was performed using GraphPad Prism Software 6.0. Student's t-tests (Figures 4C and 5E) or one-way analysis of variance (one-way ANOVA) as well as Tukey post-test (Figures 3, 6, and S7F-H) were performed to evaluate statistical differences between analyzed groups. Levels of statistical significance and "n" numbers are stated in the figure legends.

3 Results

3.1 Nanoparticle preparation and characterization

To create NPs with antigens covalently coupled to the particle surface *via* an enzyme-cleavable linker, we followed a multi-step synthesis strategy outlined in Scheme 1. First, we synthesized PEG_{5k}-$PLGA_{13.1k}$ block copolymer with a 72:28 ratio of lactic to glycolic units (Supplementary Figure S1) by ring-opening polymerization (Scheme 1A). Then, we covalently conjugated the CatS substrate as an enzymatically cleavable linker to PEG-PLGA (Supplementary Figure S2) using EDC/NHS chemistry (Scheme 1B) and prepared the NPs through nanoprecipitation (Scheme 1C). Finally, we coupled OVA *via* a maleimide thiol reaction between maleimide activated OVA and the cysteine residue of CatS substrate (Scheme 1D). The amount of protein used for the reaction was calculated based on particle surface area and protein dimensions resulting in an approximately 17-fold molar excess of CatS substrate, as we observed nonspecific adsorption of OVA to the particle surface when using higher quantities (data not shown).
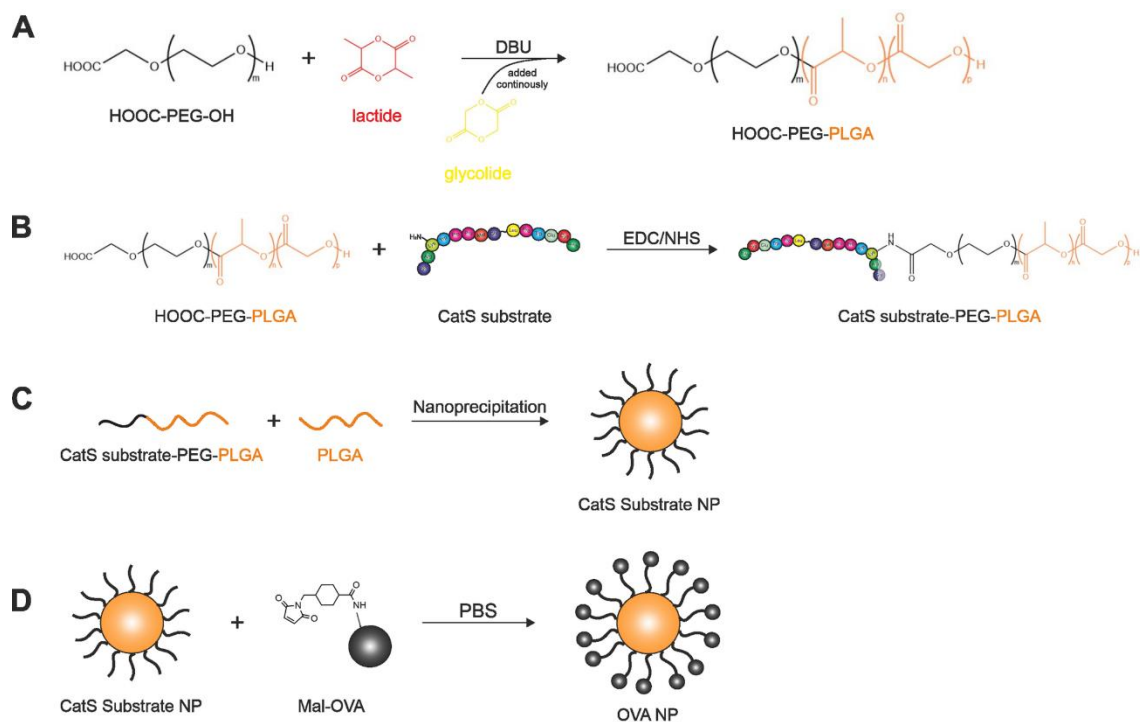
Scheme 1. NP preparation. (A) Synthesis of PEG-PLGA by ring-opening polymerization. (B) Conjugation of CatS substrate using EDC/NHS chemistry. (C) Preparation of NPs *via* nanoprecipitation. (D) Coupling of OVA using maleimide thiol reaction.

All NPs were in a size range of 100–150 nm (Figure 1A) with a PDI below 0.3 indicating a homogenous size distribution [30] and zeta potential was slightly negative (Figure 1B). Labelling of the core component PLGA or OVA with fluorescent dye did not affect particle characteristics.

We confirmed covalent conjugation of OVA by SDS-PAGE. Barium iodide staining revealed that the NPs, due to their size, were unable to migrate into the gel (Figure 1E). Coomassie staining (Figure 1C) and the more sensitive silver staining (Figure 1D) verified that no OVA was adsorbed to particle surface. Adsorbed protein would show the OVA band at 45 kDa as it would leave the particle surface and migrate into the gel during electrophoresis. The OVA band at 45 kDa was visible for the soluble OVA (lane 2), while OVA NPs (lane 3) only showed a band in the sample well corresponding to the proteins covalently conjugated to the large particles. The second band at 35 kDa visible for soluble OVA (lane 2) is probably ovomucoid, which can sometimes be present in OVA [31, 32].
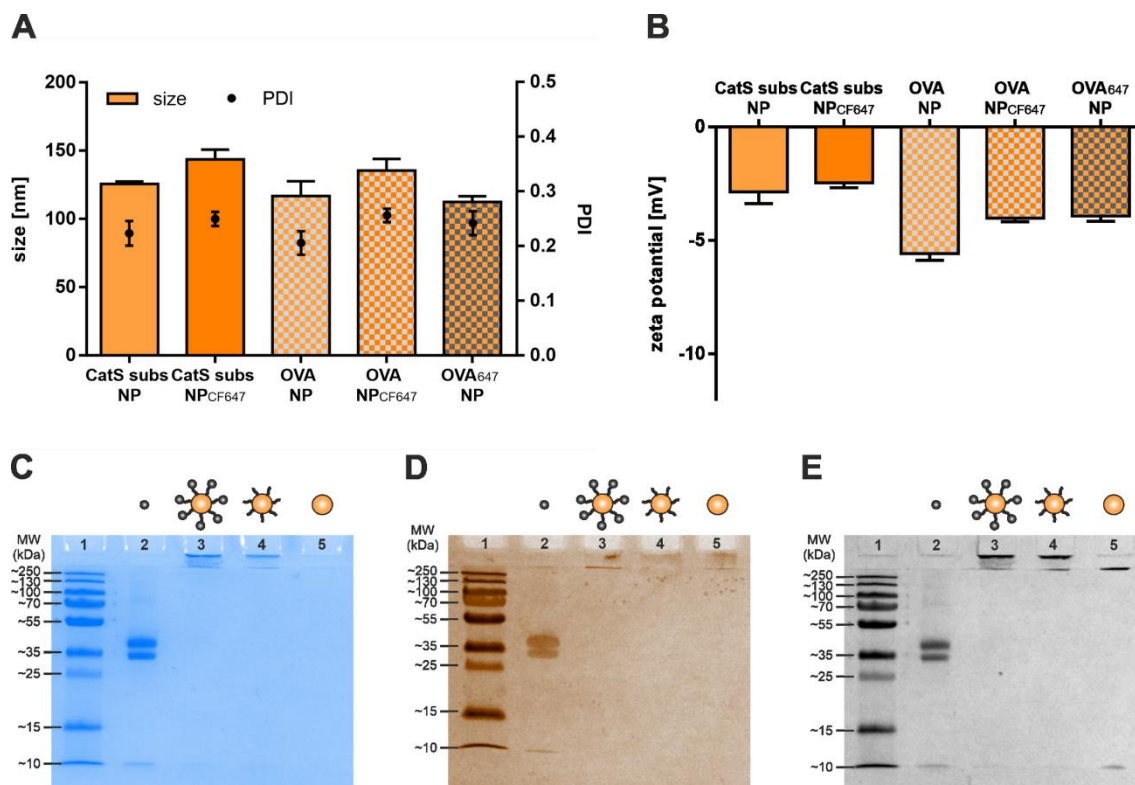
Figure 1. NP characterization. (A) Size and PDI and (B) zeta potential of the prepared NPs. (C) Coomassie, (D) silver and (E) barium iodide stained SDS-PAGE gels with ladder (lane 1), soluble OVA (lane 2), OVA NP (lane 3), CatS subs NP (lane 4) and HOOC-PEG-PLGA NP (lane 5). Results represent mean ± SD of n = 3 NP batches (A) or n = 3 measurements (B).

The average amount of OVA attached to the particle surface, determined by BCA assay, was 116 µg per mg NP, corresponding to 1635 proteins per particle and a surface coverage of approx. 98% (Table 1).

Table 1. Antigen amount per nanoparticle. Amount of OVA per mg NP, numbers of OVA per OVA NP and surface coverage of NPs with ovalbumin. Results represent mean ± SD of n = 3 NP batches.

	µg OVA per mg NP	OVA per NP	surface coverage [%]
OVA NP	116 ± 7	1635 ± 277	97.6 ± 2.0

3.2 Enzymatic cleavage of linker

To investigate whether the designed linker is cleavable by CatS, we performed cleavage assays. The sequence of our linker is based on a substrate first described by Lützner *et al.* [22], but a lysine and cysteine residue has been introduced at positions P-6 and P-5′, respectively, to enable coupling reactions. Additionally, we investigated whether conjugation to the particle surface and the antigen changes the enzymatic substrate cleavage. A FRET-labelled CatS substrate was used for this assay allowing the detection of fluorescence increase upon enzymatic cleavage. We measured the changes in fluorescence over time resulting in substrate conversion curves. As presented in Figure 2 and Supplementary Figure S4, the soluble substrate as well as the FRET-OVA NPs and the FRET-CatS subs NPs displayed an increase in fluorescence. The slope magnitude at the beginning of the curve, reflecting the substrate conversion rate (CVR), was higher for the soluble substrate (313.8 ΔAU/min) than for FRET-OVA NPs (85.8 ΔAU/min). In all cases, enzymatic activity was suppressed by addition of the inhibitor E-64, indicated by a lack of increase in fluorescence.
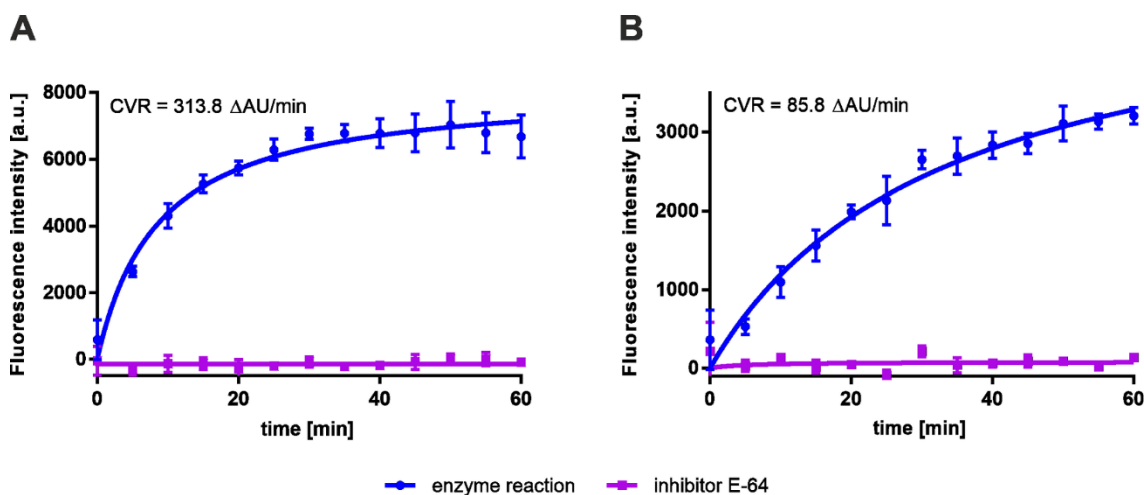
Figure 2. CatS substrate cleavage assay. CatS substrate conversion curves of (A) soluble FRET-CatS substrate and (B) FRET-OVA NPs. Results represent mean ± SD of n = 3 measurements.

3.3 Cytotoxicity and purity of NPs

FACS analysis revealed that, independently of fluorescent dye labelling, cytotoxicity was very low for our NPs (Supplementary Figure S5). Even at the highest NP concentration of 750 μg/ml, only 15% dead cells were detected, whereas the mean

particle concentration for the other experiments was much lower at around 450 μg/ml. Additional data on nanoparticle cytotoxicity are included in supplementary material.

We assessed the effect of our formulations on dendritic cell activation by determining the expression of different surface activation markers after treatment with NPs. Cells incubated with the particles expressed CD80, CD86 and CD40 at similar levels as non-treated BMDCs (Figure 3). Upon treatment with LPS, which was used as positive control, BMDCs showed a significantly increased expression of all three markers. Due to the low immunostimulatory potential of our NPs, we decided to add ODN1826 as an adjuvant for future experiments.
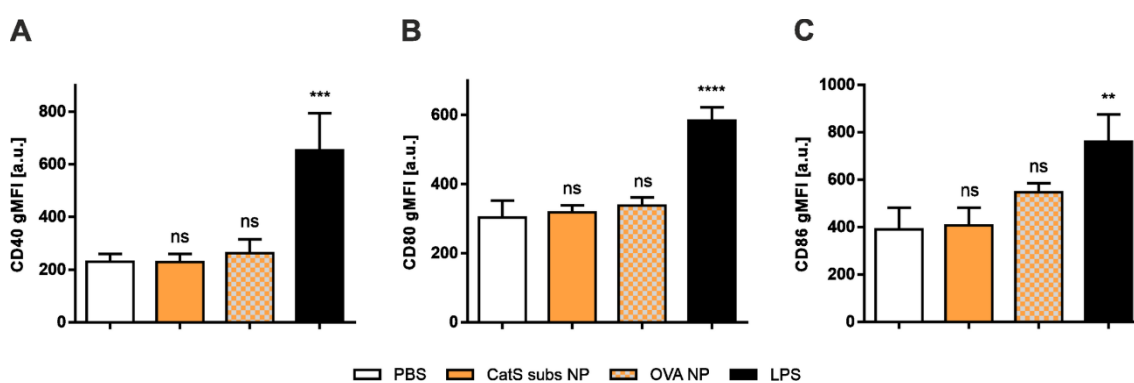
Figure 3. Effect of NPs on BMDC activation. Expression levels of (A) CD40, (B) CD80 and (C) CD86 on BMDCs after stimulation with NP formulations and LPS as positive control. Results represent mean ± SD of n = 3 experiments. Levels of statistical significance are indicated as **P ≤ 0.01, ***P ≤ 0.001 and ****P ≤ 0.0001, ns: non-significant.

3.4 Cellular uptake and intracellular antigen localization

We demonstrated internalization of our particle formulations into BMDCs using confocal microscopy and flow cytometry (Figure 4). We tested CatS subs NP_{CF647} and OVA NP_{CF647} in which the core component PLGA was labelled with fluorescent CF™ 647 dye, as well as OVA_{647} NP in which the surface-conjugated OVA was tagged with fluorescent Alexa Fluor™ 647. After 2 h, both CatS subs NP_{CF647} and OVA NP_{CF647} were internalized by CTG-stained BMDCs (Figure 4, A). Of note, the uptake of OVA NP_{CF647}, as determined by both CLSM and flow cytometry, was more efficient than for CatS subs NP_{CF647} (Figure 4A and 4C). The control experiment at 4 °C demonstrated a negligible fluorescence derived from particle binding to the cell surface (data not shown). Additionally, CLSM images of OVA_{647} NPs revealed the successful cellular uptake of OVA conjugated to the NPs after 2 h (Figure 4B).
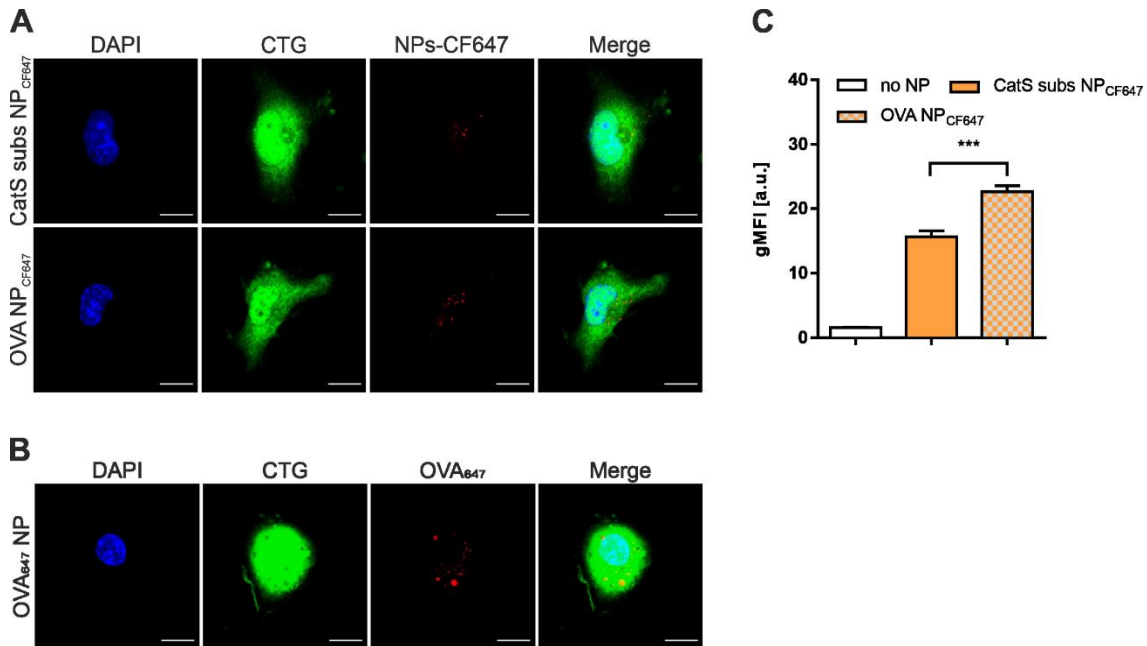
Figure 4. Uptake of NPs by BMDCs. CLSM images of (A) core-labelled and (B) OVA-labelled NPs (red) internalized by CTG-stained BMDCs (green). Nuclei are stained with DAPI (blue). Scale bar 10 µm. (C) Uptake of core-labelled particles by BMDCs as shown by flow cytometry. Results represent mean ± SD of n = 3 measurements. Level of statistical significance is indicated as ***$P \leq 0.001$.

To further study the intracellular antigen localization after uptake, we assessed colocalization of fluorescently labelled OVA_{647} attached to NPs with a cleavable (OVA_{647} NPs) or a non-cleavable linker (OVA_{647}-stL NPs), respectively, with early endosome antigen 1 (EEA1), a marker for the endosomal compartments, or lysotracker (LTG), a dye for staining lysosomal compartments. Characteristics of the control particles (stL NPs and OVA-stL NPs) were comparable to those of CatS subs NPs and OVA NPs (Supplementary Figure S7 and Supplementary Table S2). Confocal imaging (Figure 5A-D) revealed that OVA_{647} released from the NPs with the cleavable linker is more localized outside the endo-lysosomal organelles in the cytosol, visible as the separation of the red antigen fluorescence from the green organelle fluorescence. Antigens on NPs with the stable linker, in turn, remained in the endo-lysosomal compartments, recognizable by the yellow spots indicating colocalization, especially in the LTG images. We quantified colocalization by determining Manders' colocalization coefficient which reflects the fraction of OVA fluorescence colocalized with EEA1/lysotracker fluorescence in relation to the total OVA fluorescence in a cell [29]. Colocalization coefficients showed a significantly higher colocalization of OVA_{647}

conjugated to OVA$_{647}$-stL NPs with both endosomes and lysosomes, compared to OVA$_{647}$ from OVA$_{647}$ NPs (Figure 5E).
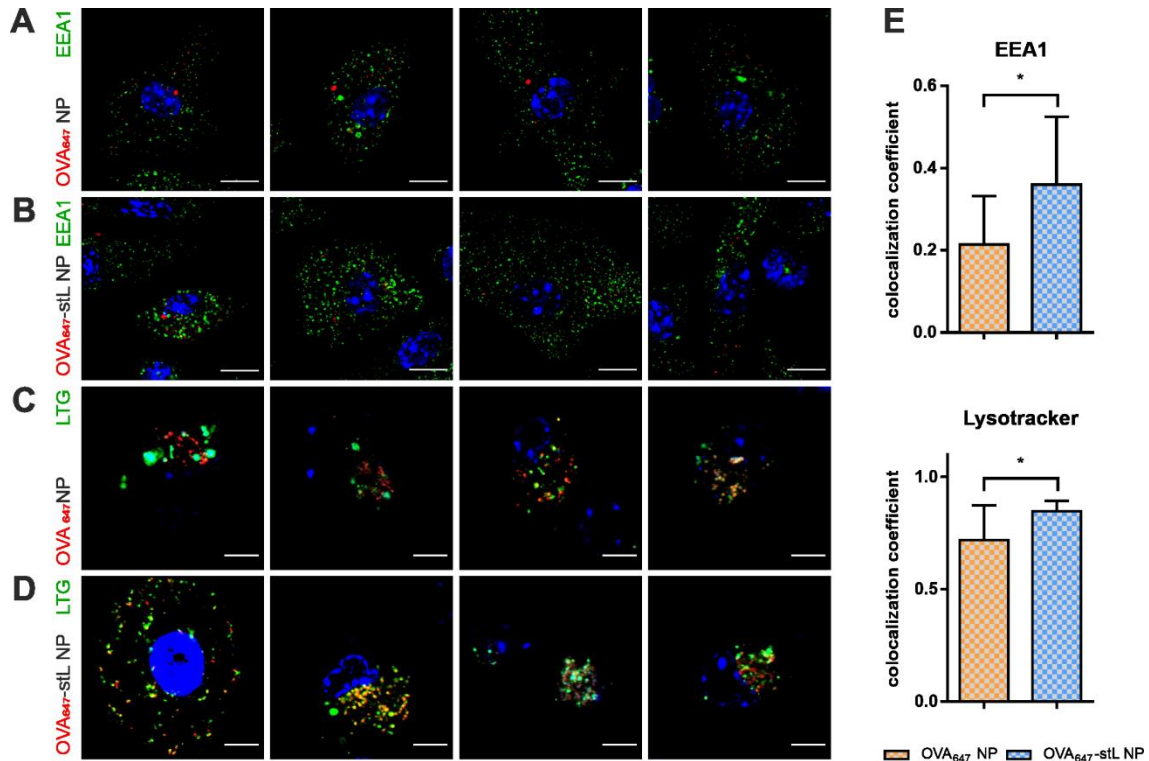
Figure 5. Intracellular antigen localization of NPs after internalization by BMDCs. (A-D) Confocal microscopy images of OVA$_{647}$ NP or OVA$_{647}$-stL NP (red) and endosomal (EEA1) or lysosomal (LTG) vesicles (green) after 2 h incubation of NPs with BMDCs. Nuclei are stained with DAPI or Hoechst (blue). Scale bar 10 μm (A-B) and 5 μm (C-D). (E) Manders' coefficient for colocalization of OVA$_{647}$ NP or OVA$_{647}$-stL NP with EEA1 or lysotracker. Results represent mean ± SD of n = 10 cells. Level of statistical significance is indicated as *P ≤ 0.05.

3.5   Antigen presentation by BMDCs

To assess antigen presentation by BMDCs after stimulation with our NPs, we performed co-culture experiments of BMDCs and naïve OTI CD8$^+$ T cells. OTI T cells express a transgenic T cell receptor that specifically recognizes the peptide OVA$_{257-264}$ in context of MHC-I. BMDCs were incubated with different particle formulations and CpG ODN1826. After co-culture with naïve CD8$^+$ T cells, the percentage of activated (CD44$^+$) T cells was determined. The co-culture results revealed that OVA NPs promoted a significantly higher percentage of activated T cells compared to OVA-stL NPs (Figure 6), suggesting an enhanced cross-presentation of OVA delivered on particles with the enzymatically cleavable linker.
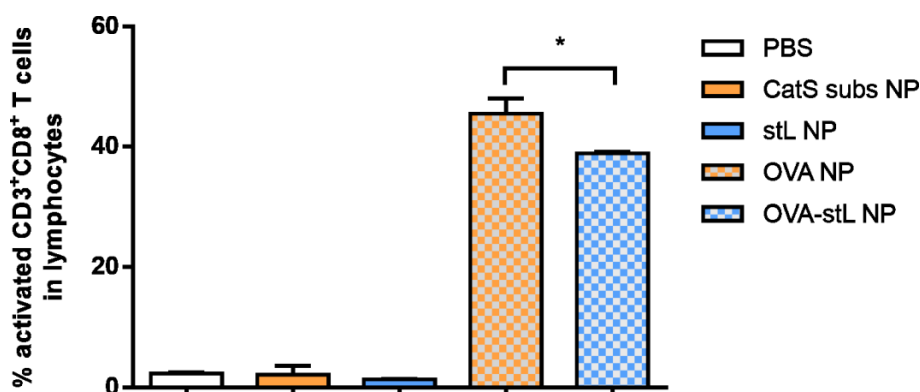
Figure 6. OTI CD8+ T cell activation by BMDCs incubated with different NP formulations and CpG ODN1826. Percentage of activated OTI T cells (CD44+CD3+CD8+) assessed by flow cytometry. Results represent mean ± SD (n = 4). Level of statistical significance is indicated as *P ≤ 0.05.

4   Discussion

The induction of a robust cytotoxic T cell response is one of the biggest challenges in vaccine development and crucial for establishing protective immunity against tumors and intracellular pathogens [33, 34]. One promising approach to improve the priming of CD8+ T cells is the use of nanoparticulate subunit vaccines [35], which are attractive due to their safety, defined composition and cost-effectiveness [4, 36]. To elicit such an immune response to subunit vaccines, DCs have to present the exogenous vaccine antigens on MHC-I molecules, a process called cross-presentation [37]. For the particulate antigens of nanovaccines, antigen presentation is time-dependent. If internalized antigens are available before acidification and maturation of endosomes to lysosomes, cross-presentation is favored whereas antigen processing in mature lysosomes leads to MHC-II restricted presentation [38]. Hirosue *et al.* showed that antigens conjugated to NPs with a disulfide bond reducible in the early endosomal compartments are preferably cross-presented on DCs [16]. We assumed that an enzyme-based release can also enhance cross-presentation. One of the few enzymes that are active in the early endosome is the protease CatS [20, 21]. We hypothesized that exploiting the activity of this enzyme for antigen release could enhance cross-presentation due to the increased availability of free antigen in the early endosome.

In this study, we developed a nanoparticulate antigen delivery platform with a CatS-mediated antigen release mechanism. We demonstrated that antigens from these particles are more efficiently cross-presented by DCs than antigens from particles

without enzymatic antigen release, subsequently leading to a more pronounced CD8^{+} T cell activation *in vitro* likely due to early endosomal escape of the antigen and subsequent cytosolic cross-presentation pathway.

We successfully immobilized the model antigen ovalbumin on the surface of polymeric NPs *via* an enzymatically cleavable linker, while control particles contained a stable, non-cleavable linker. Because of their biocompatibility, non-toxicity and good biodegradability [39], we used PLGA and PEG-PLGA as material for the particle platform. We synthesized a PEG-PLGA block copolymer with a high lactic acid content to increase hydrophobicity and therefore slow down the degradation rate *in vitro* and *in vivo* [40]. With these superior stability properties, the NPs should be able to reach the lymph nodes, the sites of action of vaccines, before they degrade. For the preparation of our particle system, we used established and simple conjugation reactions [25, 41] resulting in a versatile system where individual components can be easily exchanged without affecting the particle properties. As shown for our control particles, the linker exchange had no effect on the physicochemical particle properties. The high level of versatility makes this system very attractive as vaccine platform as it can be used for immunization against numerous diseases or pathogens by simply changing the antigen. In addition, by coupling to the polymers, adjuvants can also be integrated. For NP preparation, we blended block copolymer PEG-PLGA with PLGA to improve particle stability and integrity [42]. NP size between 100 and 150 nm offers the ideal dimensions to be transported directly to the lymph nodes *via* lymph drainage [43].

As an enzymatically cleavable linker, we chose a specific CatS substrate discovered by Lützner *et al.* [22], Mca-GRWPPMGLPWE-Lys(Dnp)-DArg-NH$_2$, which shows only a single cleavage site between Gly and Leu. We modified the substrate at positions P-6 and P-5′ to enable coupling reactions. The cleavage assay with the soluble substrate revealed that the introduced lysine and cysteine residues did not affect substrate cleavability. These results are in line with Lützner *et al.* who identified P-2, P-1′, and P-3′ as the essential substrate positions for CatS specificity [22]. The enzymatic conversion of substrates bound to materials – such as surfaces, nanoparticles, or hydrogels – may completely differ from the soluble substrates, due to steric hindrance or lower mobility [44]. Therefore, we also verified the cleavage of the particle-bound CatS substrate. As the conversion curves showed, CatS was still able to catalyze the hydrolysis. Taken together, our results suggest that the modified substrate is suitable for triggering the enzymatic antigen release from NPs that we are aiming for.

Before using NPs in functional studies, it was mandatory to test their safety and toxicity. As professional antigen-presenting cells, DCs, which are our target cells, capture and process antigens and present them to T cells. Our cytotoxicity assay in BMDCs revealed low cytotoxicity for our particles, indicating good biocompatibility of the polymers used and the successful removal of potentially cytotoxic by-products of the synthesis. Additionally, the absence of LPS and other pyrogens is crucial for the use of NPs in immune assays to avoid misinterpretation of results [45]. We modified the particle preparation procedure as described above to minimize the risk of contamination [26]. The lack of upregulation of the maturation markers after treating BMDCs with our particle formulations suggested that the NPs were clean and free of endotoxin.

To act as an efficient antigen delivery platform, internalization by DCs is essential for our nanoparticle system as it initiates antigen processing and presentation. CLSM images showed that both particle core and antigens were taken up by DCs, indicating that the particle system remains intact during the uptake process. Additionally, the uptake studies revealed that the particles with OVA were internalized more efficiently than those without antigens. DCs internalize NPs *via* phagocytosis and macropinocytosis [46] while soluble OVA is known to be taken up through macropinocytosis and clathrin-mediated endocytosis *via* the mannose receptor (MR) [47]. We hypothesized that the ovalbumin on the OVA NP surface likely also addresses the MR causing the NPs to be taken up through a third uptake route. That results in an enhanced uptake of OVA NPs compared to the NPs without ovalbumin. Our results agree with Chang *et al.* who postulated a clathrin-mediated uptake *via* the mannose receptor for their OVA protein NPs [48].

The intracellular pathway of an antigen strongly determines its type of presentation and thus the consecutive T cell response. As described above, an escape of the antigen from the early endosome leads to cross-presentation *via* the cytosolic pathway. Colocalization studies revealed a lower colocalization of ovalbumin from OVA NPs with endosomes and lysosomes. This suggests that the antigens underwent an endosomal escape into the cytosol likely due to the enzymatic release from the carrier because of the activity of CatS in the early endosome. On the other hand, antigens from OVA-stL NPs were not released from the particle and thus could not be exported into the cytosol but remained in the endo-lysosomal compartments, detectable as a higher colocalization with endosomes and lysosomes. Overall, these results confirmed the predicted intracellular trafficking of

our particle system and supported the assumption that the particles with a cleavable linker show enhanced antigen cross-presentation.

Finally, we investigated whether the antigen released from our nanoparticle system is cross-presented by BMDCs and whether these can then activate cytotoxic CD8^{+} T cells. The co-culture results showed that after stimulation with OVA NPs a significantly higher percentage of CD8^{+} T cells were activated than with OVA-stL NPs, suggesting that the enzymatic antigen release enhances cross-presentation. The findings support our hypothesis that exploiting CatS activity in the early endosome for antigen release leads to an endosomal escape with subsequent proteasomal processing and MHC-I loading of the antigen, i.e., that it induces the cytosolic cross-presentation pathway. CatS also plays an important role in the vacuolar pathway of antigen cross- presentation. The protease is known to generate MHC-I restricted peptides for loading within the vacuolar compartments [20, 49]. In the case of our particle system, the antigen is released from the nanoparticle in the early endosome and thus available in its soluble form. The protease CatS possibly has better access to this released soluble antigen for peptide processing than to the particle-bound ones as in the case of the control particles. We assume that the enzymatic antigen release possibly also favors the vacuolar cross-presentation pathway. An illustration of the proposed intracellular trafficking of our particle system is shown in Scheme 2.
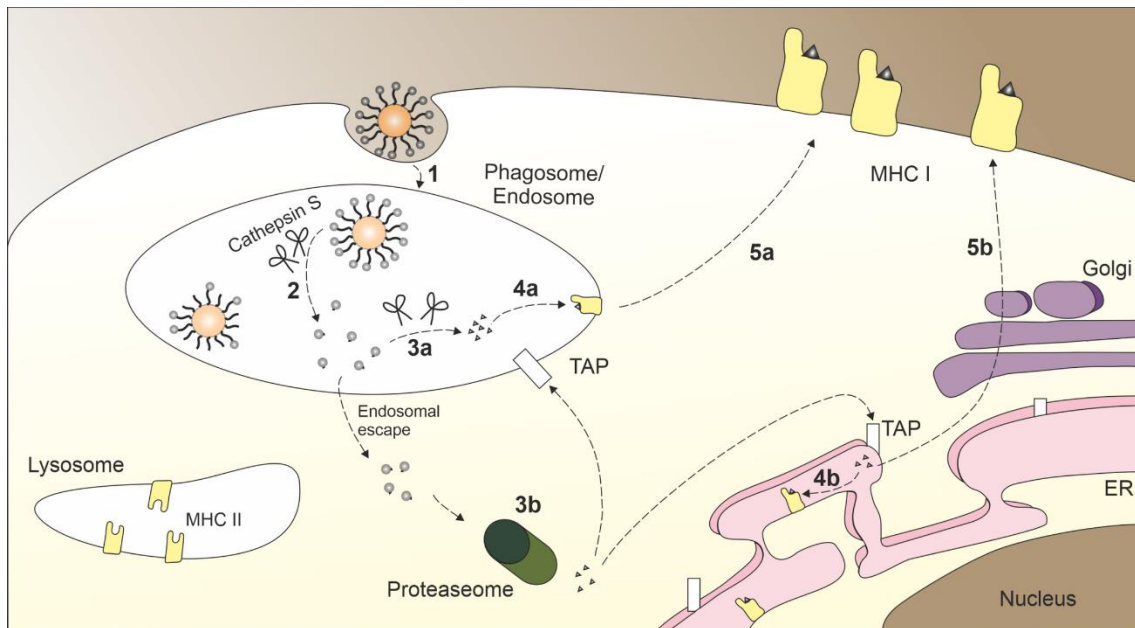
Scheme 2. Suggested subcellular mechanisms of antigen cross-presentation of OVA NPs. After uptake of OVA NPs in phagosomes/endosomes (1), antigens are released by enzymatic linker cleavage through CatS (2). Free antigens are either processed further by CatS (3a) and loaded onto MHC-I molecules within the phagosomes/endosomes (4a) or undergo an endosomal escape and are processed by proteasomes in the cytosol (3b) and loaded onto MHC-I receptors in the endoplasmic reticulum (ER) (4b) or in phagosomes/endosomes (4a). Antigen-MHC-I complexes are then transported to the cell membrane for CD8+ T cell recognition (5a, 5b).

Altogether, we have shown that an enzyme-triggered antigen release can enhance the cross-presentation by dendritic cells. We successfully developed a non-toxic nanoparticulate antigen delivery system that is internalized by BMDCs and enzymatically releases its antigens which are then cross-presented on MHC-I molecules. Our data suggest that the CatS-triggered antigen release allows endosomal escape and subsequent MHC-I processing. The presented enzyme-sensitive mechanism and the highly versatile particle design offer a simple and new approach for T cell inducing vaccines. Thus, it would be worthwhile to test the potential of this mechanism to elicit a cytotoxic T cell response *in vivo*.

References

1. World Health Organization. Vaccines and immunization. Available at https://www.who.int/health-topics/vaccines-and-immunization#tab=tab_1.

2. Mao HH, Chao S. Advances in Vaccines. *Adv Biochem Eng Biotechnol*. 2020; 171: 155–188.

3. Cuzzubbo S, Mangsbo S, Nagarajan D, Habra K, Pockley AG, McArdle SEB. Cancer Vaccines: Adjuvant Potency, Importance of Age, Lifestyle, and Treatments. *Front Immunol*. 2020; 11: 615240.

4. Brisse M, Vrba SM, Kirk N, Liang Y, Ly H. Emerging Concepts and Technologies in Vaccine Development. *Front Immunol*. 2020; 11: 583077.

5. Zhao L, Seth A, Wibowo N, et al. Nanoparticle vaccines. *Vaccine*. 2014; 32: 327–337.

6. Pati R, Shevtsov M, Sonawane A. Nanoparticle Vaccines Against Infectious Diseases. *Front Immunol*. 2018; 9: 2224.

7. Mitchell MJ, Billingsley MM, Haley RM, Wechsler ME, Peppas NA, Langer R. Engineering precision nanoparticles for drug delivery. *Nat Rev Drug Discov*. 2021; 20: 101–124.

8. Griffiths KL, Khader SA. Novel vaccine approaches for protection against intracellular pathogens. *Current Opinion in Immunology*. 2014; 28: 58–63.

9. Durgeau A, Virk Y, Corgnac S, Mami-Chouaib F. Recent Advances in Targeting CD8 T-Cell Immunity for More Effective Cancer Immunotherapy. *Front Immunol*. 2018; 9: 14.

10. Kastenmüller W, Kastenmüller K, Kurts C, Seder RA. Dendritic cell-targeted vaccines--hope or hype? *Nat Rev Immunol*. 2014; 14: 705–711.

11. Théry C, Amigorena S. The cell biology of antigen presentation in dendritic cells. *Current Opinion in Immunology*. 2001; 13: 45–51.

12. Burgdorf S, Kautz A, Böhnert V, Knolle PA, Kurts C. Distinct pathways of antigen uptake and intracellular routing in CD4 and CD8 T cell activation. *Science*. 2007; 316: 612–616.

13. Joffre OP, Segura E, Savina A, Amigorena S. Cross-presentation by dendritic cells. *Nat Rev Immunol*. 2012; 12: 557–569.

14. Chen J, Li Z, Huang H, et al. Improved antigen cross-presentation by polyethyleneimine-based nanoparticles. *Int J Nanomedicine*. 2011; 6: 77–84.

15. Yuba E, Harada A, Sakanishi Y, Watarai S, Kono K. A liposome-based antigen delivery system using pH-sensitive fusogenic polymers for cancer immunotherapy. *Biomaterials*. 2013; 34: 3042–3052.

16. Hirosue S, Kourtis IC, van der Vlies AJ, Hubbell JA, Swartz MA. Antigen delivery to dendritic cells by poly(propylene sulfide) nanoparticles with disulfide conjugated peptides: Cross-presentation and T cell activation. *Vaccine*. 2010; 28: 7897–7906.

17. Kim CG, Kye Y-C, Yun C-H. The Role of Nanovaccine in Cross-Presentation of Antigen-Presenting Cells for the Activation of CD8+ T Cell Responses. *Pharmaceutics*. 2019; 11.

18. Yadati T, Houben T, Bitorina A, Shiri-Sverdlov R. The Ins and Outs of Cathepsins: Physiological Function and Role in Disease Management. *Cells*. 2020; 9.

19. Patel S, Homaei A, El-Seedi HR, Akhtar N. Cathepsins: Proteases that are vital for survival but can also be fatal. *Biomed Pharmacother*. 2018; 105: 526–532.

20. Blander JM. Regulation of the Cell Biology of Antigen Cross-Presentation. *Annu Rev Immunol*. 2018; 36: 717–753.

21. Savina A, Amigorena S. Phagocytosis and antigen presentation in dendritic cells. *Immunol Rev*. 2007; 219: 143–156.

22. Lützner N, Kalbacher H. Quantifying cathepsin S activity in antigen presenting cells using a novel specific substrate. *J Biol Chem*. 2008; 283: 36185–36194.

23. Lutz MB, Kukutsch N, Ogilvie ALJ, et al. An advanced culture method for generating large quantities of highly pure dendritic cells from mouse bone marrow. *J Immunol Methods*. 1999; 223: 77–92.

24. Qian H, Wohl AR, Crow JT, Macosko CW, Hoye TR. A Strategy for Control of "Random" Copolymerization of Lactide and Glycolide: Application to Synthesis of PEG-b-PLGA Block Polymers Having Narrow Dispersity. *Macromolecules*. 2011; 44: 7132–7140.

25. Abstiens K, Gregoritza M, Goepferich AM. Ligand Density and Linker Length are Critical Factors for Multivalent Nanoparticle-Receptor Interactions. *ACS Appl Mater Interfaces*. 2019; 11: 1311–1320.

26. Vallhov H, Qin J, Johansson SM, et al. The importance of an endotoxin-free environment during the production of nanoparticles used in medical applications. *Nano Lett*. 2006; 6: 1682–1686.

27. Malvern Instruments Ltd. The Diffusion Barrier Technique, Practical Aspects and Data interpretation. Available at https://www.atascientific.com.au/wp-content/uploads/2017/02/MRK1651-02.-The-Diffusion-Barrier-Technique-Practical-Aspects-and-Data-interpretation.pdf.

28. Kurfürst MM. Detection and molecular weight determination of polyethylene glycol-modified hirudin by staining after sodium dodecyl sulfate-polyacrylamide gel electrophoresis. *Analytical Biochemistry*. 1992; 200: 244–248.

29. Manders EMM, Verbeek FJ, Aten JA. Measurement of co-localization of objects in dual-colour confocal images. *J Microsc*. 1993; 169: 375–382.

30. Danaei M, Dehghankhold M, Ataei S, et al. Impact of Particle Size and Polydispersity Index on the Clinical Applications of Lipidic Nanocarrier Systems. *Pharmaceutics*. 2018; 10.

31. Geng F, Xie Y, Wang J, Li S, Jin Y, Ma M. Large-scale purification of ovalbumin using polyethylene glycol precipitation and isoelectric precipitation. *Poult Sci*. 2019; 98: 1545–1550.

32. Abeyrathne EDNS, Lee HY, Ahn DU. Sequential separation of lysozyme, ovomucin, ovotransferrin, and ovalbumin from egg white. *Poult Sci*. 2014; 93: 1001–1009.

33. Salerno-Gonçalves R, Sztein MB. Cell-mediated immunity and the challenges for vaccine development. *Trends Microbiol*. 2006; 14: 536–542.

34. Gilbert SC. T-cell-inducing vaccines - what's the future. *Immunology*. 2012; 135: 19–26.

35. Du G, Sun X. Engineering nanoparticulate vaccines for enhancing antigen cross-presentation. *Curr Opin Biotechnol*. 2020; 66: 113–122.

36. Wang M, Jiang S, Wang Y. Recent advances in the production of recombinant subunit vaccines in Pichia pastoris. *Bioengineered*. 2016; 7: 155–165.

37. Foged C, Hansen J, Agger EM. License to kill: Formulation requirements for optimal priming of CD8(+) CTL responses with particulate vaccine delivery systems. *Eur J Pharm Sci*. 2012; 45: 482–491.

38. Burgdorf S, Kurts C. Endocytosis mechanisms and the cell biology of antigen presentation. *Current Opinion in Immunology*. 2008; 20: 89–95.

39. Locatelli E, Comes Franchini M. Biodegradable PLGA-b-PEG polymeric nanoparticles: synthesis, properties, and nanomedical applications as drug delivery system. *J Nanopart Res*. 2012; 14: 3582.

40. Makadia HK, Siegel SJ. Poly Lactic-co-Glycolic Acid (PLGA) as Biodegradable Controlled Drug Delivery Carrier. *Polymers (Basel)*. 2011; 3: 1377–1397.

41. Hermanson GT. *Bioconjugate techniques*. Amsterdam: Academic Press; 2008.

42. Owen SC, Chan DPY, Shoichet MS. Polymeric micelle stability. *Nano Today*. 2012; 7: 53–65.

43. Bachmann MF, Jennings GT. Vaccine delivery: A matter of size, geometry, kinetics and molecular patterns. *Nat Rev Immunol*. 2010; 10: 787–796.

44. Zelzer M, Todd SJ, Hirst AR, McDonald TO, Ulijn RV. Enzyme responsive materials: design strategies and future developments. *Biomater Sci*. 2013; 1: 11–39.

45. Swartzwelter BJ, Fux AC, Johnson L, et al. The Impact of Nanoparticles on Innate Immune Activation by Live Bacteria. *Int J Mol Sci*. 2020; 21.

46. Donahue ND, Acar H, Wilhelm S. Concepts of nanoparticle cellular uptake, intracellular trafficking, and kinetics in nanomedicine. *Adv Drug Deliv Rev*. 2019; 143: 68–96.

47. Autenrieth SE, Autenrieth IB. Variable antigen uptake due to different expression of the macrophage mannose receptor by dendritic cells in various inbred mouse strains. *Immunology*. 2009; 127: 523–529.

48. Chang TZ, Stadmiller SS, Staskevicius E, Champion JA. Effects of ovalbumin protein nanoparticle vaccine size and coating on dendritic cell processing. *Biomater Sci*. 2017; 5: 223–233.

49. Shen L, Sigal LJ, Boes M, Rock KL. Important role of cathepsin S in generating peptides for TAP-independent MHC class I crosspresentation in vivo. *Immunity*. 2004; 21: 155–165.

Chapter 4 – Supporting Information

Enzyme-triggered antigen release enhances cross-presentation by dendritic cells

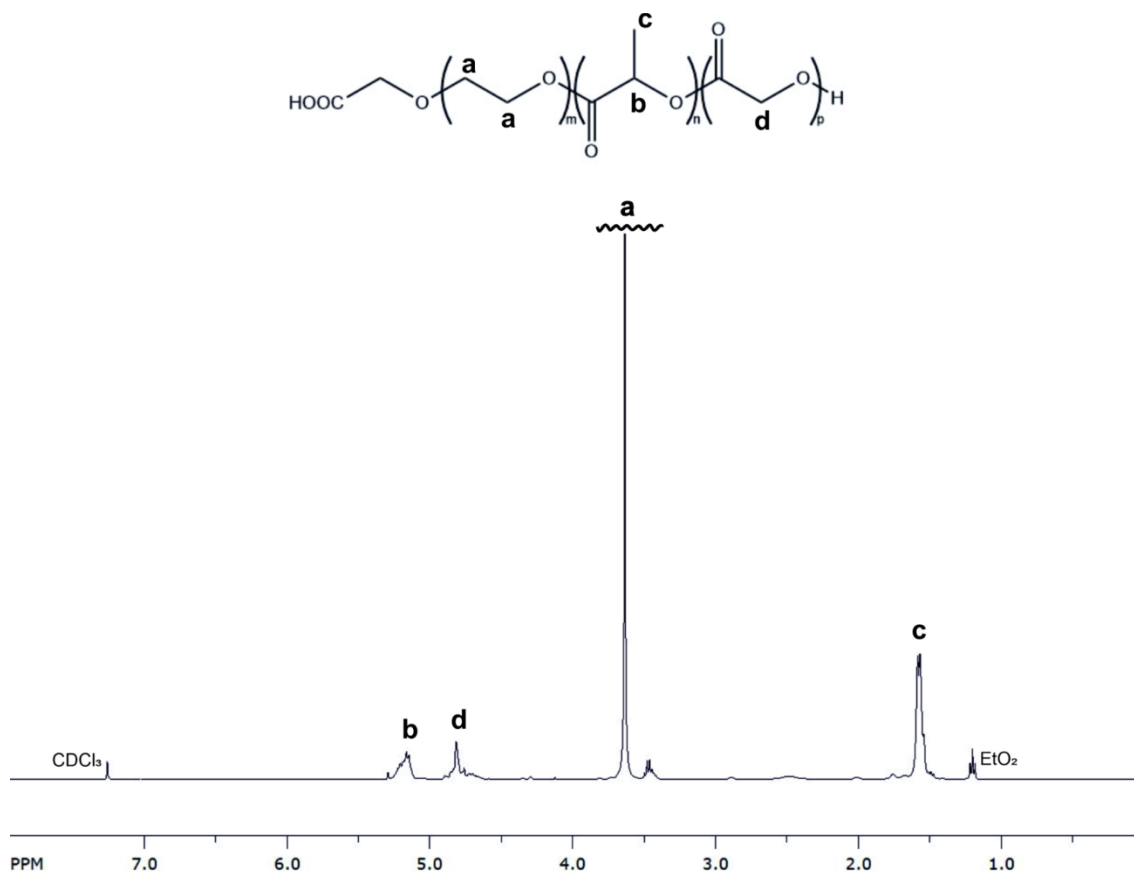# 1   Polymer characterization

Figure S1. ^{1}H-NMR (CDCl$_3$, 300 MHz) spectrum of HOOC-PEG$_{5k}$-PLGA$_{13.1k}$ synthesized by ring-opening polymerization. First, racemic 3,6-dimethyl-1,4-dioxane-2,5-dione (D,L-lactide) and 1,4-dioxane-2,5-dione (glycolide) were recrystallized from ethyl acetate and tetrahydrofuran (THF), respectively, and dried under vacuum for 12 h. Carboxylic acid-terminated poly(ethylene glycol) (0.09 mmol), which was used as macroinitiator, was dissolved in dichloromethane (DCM), mixed with lactide (12.6 mmol) and reaction was initiated by adding 1,8-diazabicyclo[5.4.0]undec-7-ene (DBU) (0.27 mmol) as catalyst. Immediately thereafter, glycolide (2.61 mmol) dissolved in THF was added continuously at a rate of 1.2 ml/min (10 min) until ring-opening polymerization was quenched with benzoic acid (1.35 mmol). Resulting block copolymer was purified by precipitation in diethyl ether and dried under vacuum. Molecular weight and mass ratio of lactic to glycolic units were calculated by integration of ^{1}H-NMR spectrum.
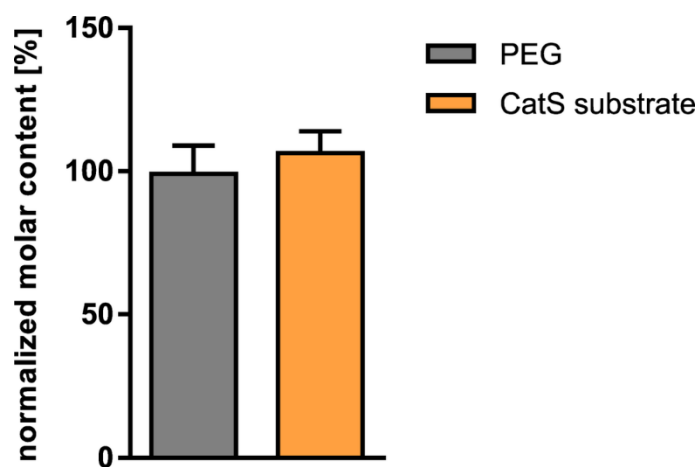
Figure S2. PEG and CatS substrate content of nanoparticles (NPs) normalized to the PEG content. PEG was quantified by a colorimetric iodine complexing assay and CatS substrate by a BCA assay. Results represent mean ± SD of n = 6 measurements

2 Characterization of FRET-labeled polymer and NPs
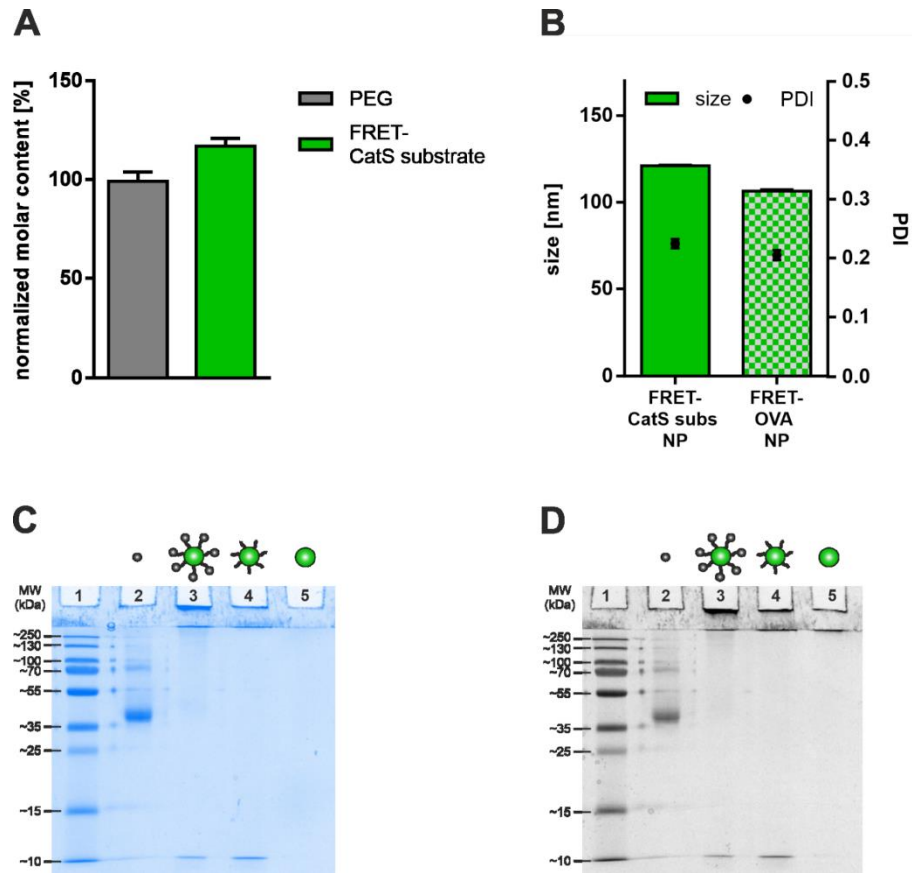
Figure S3. Characteristics of FRET-labeled polymer and NPs. Synthesized FRET-CatS subs-PEG-PLGA as well as prepared FRET-CatS subs NPs and FRET-OVA NPs displayed similar characteristics as non-labeled polymer and NPs. (A) PEG and CatS substrate content of FRET-CatS subs NPs determined by colorimetric iodine complexing assay and BCA assay, respectively. (B) Size and PDI of the prepared NPs. (C) Coomassie Blue and (D) barium iodide stained SDS-PAGE gels with ladder (lane 1), soluble OVA (lane 2), FRET-OVA NP (lane 3), FRET-CatS subs NP (lane 4) and HOOC-PEG-PLGA NP (lane 5) revealed that no OVA was adsorbed. Results represent mean ± SD of n = 3 measurements.

Table S1. Amount of OVA per mg NP, numbers of OVA per FRET-OVA NP and surface coverage of NPs with ovalbumin. Results represent mean ± SD of n = 3 measurements.

	µg OVA per mg NP	OVA per NP	surface coverage [%]
OVA NP	139 ± 13	1522 ± 114	108.1 ± 9.5

3   Cleavage assay with FRET-CatS subs NPs
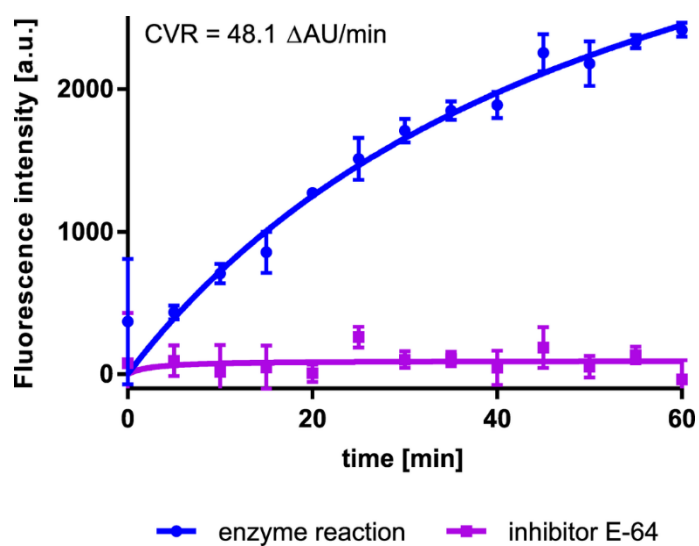
Figure S4. Cathepsin S substrate conversion curve of FRET-CatS subs NPs. Results represent mean ± SD of n = 3 measurements.

4   Cytotoxicity of nanoparticles
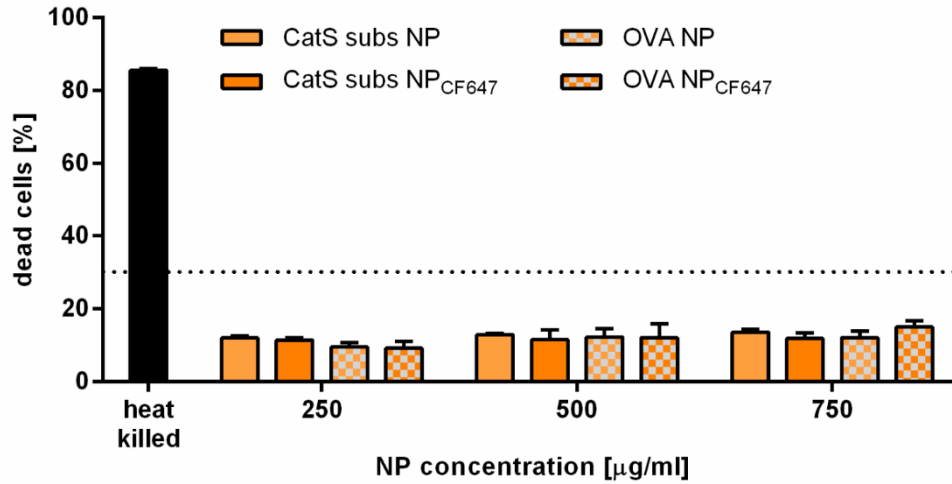
Figure S5. Dendritic cell viability after treatment with CF647-labeled and unlabeled NPs. BMDCs were seeded at 3 x 10^5 cells/well in a 96-well plate and pre-incubated for 2 h. After addition of NP solutions at final concentrations of 250, 500 or 750 µg/ml, respectively, and a 24-h incubation period, percentage of dead cells was analyzed by flow cytometry using propidium iodide as live/dead stain. Heat-killed cells (10 min, 70°C) were used as a positive control. The dotted line indicates 30% dead cells. Results represent mean ± SD of n = 3 measurements.
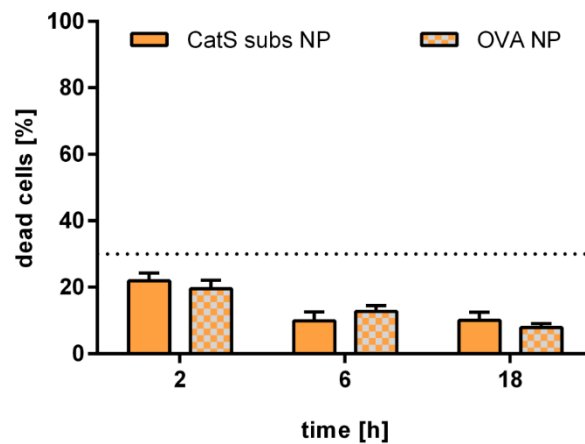
Figure S6. Viability of dendritic cells that had internalized NPs. BMDCs were seeded at 3 x 10^5 cells/well in a 96-well plate and cultured for 2 h. NPs (OVA concentration 50 µg/ml) and ODN1826 (63 ng/ml) were added. After 2, 6 and 18 h, cells were labelled with anti-CD11c-FITC and percentage of dead cells in the population of NP-positive BMDCs was analyzed by flow cytometry using propidium iodide as live/dead stain. The dotted line indicates 30% dead cells. No more than 23% dead cells were detectable. According to ISO guideline 10993−5:2009 (Biological evaluation of medical devices, part 5: Tests for *in vitro* cytotoxicity) the particles can be considered 'non-toxic'. Results represent mean ± SD of n = 3 measurements.

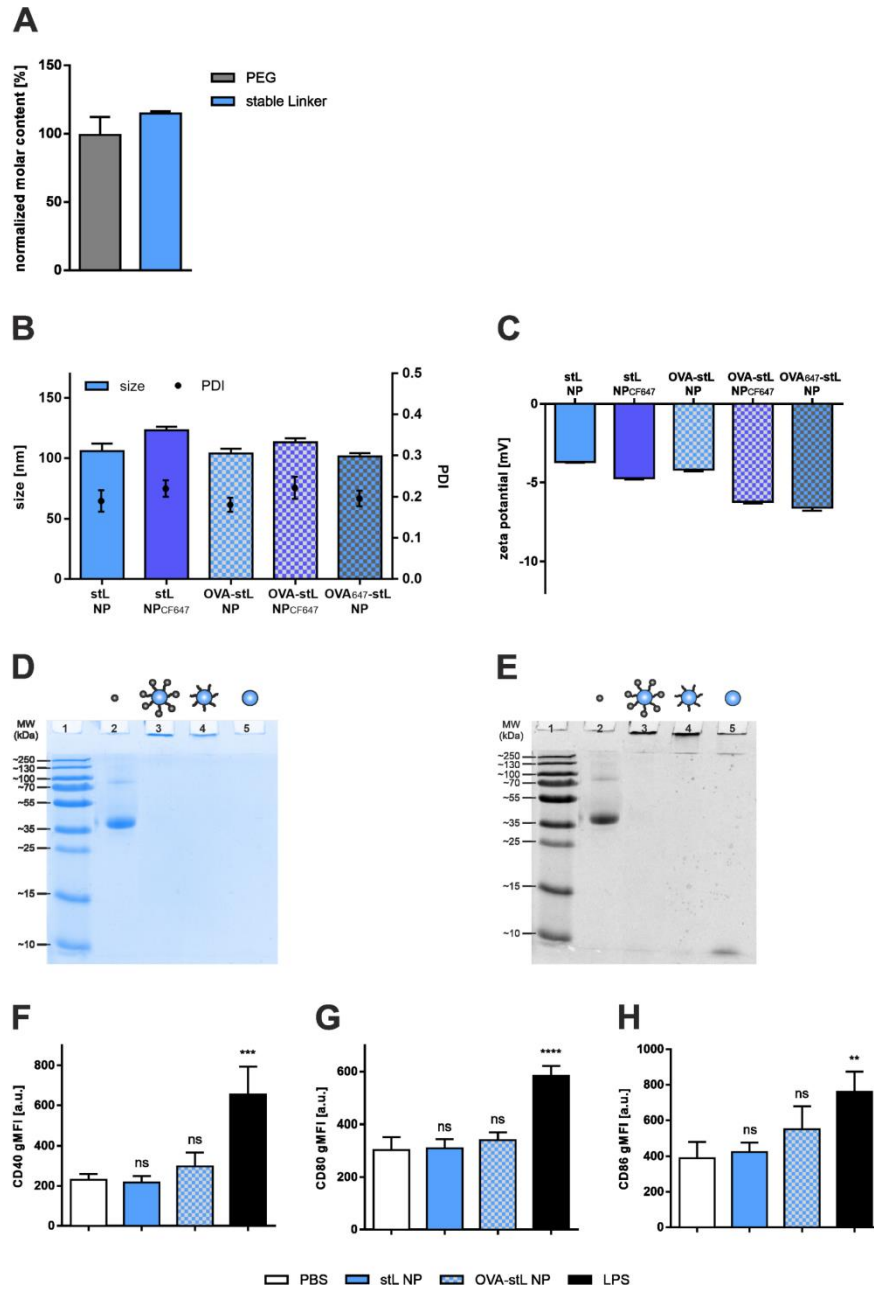## 5 Characterization of stable linker polymer and NPs

Figure S7. Characteristics of stable linker polymer and NPs. (A) PEG and stable linker content of stL NPs determined by colorimetric iodine complexing assay and BCA assay, respectively. (B) Size and PDI and (C) zeta potential of the prepared NPs. (D) Coomassie and (E) barium iodide stained SDS-PAGE gels with ladder (lane 1), soluble OVA (lane 2), OVA-stL NP (lane 3), stL NP (lane 4) and HOOC-PEG-PLGA NP (lane 5) revealed that no OVA was adsorbed. (F-H) Expression levels of CD40, CD80 and CD86 on BMDCs after stimulation with NP formulations demonstrated that the NPs were endotoxin-free. PBS and LPS served as negative and positive control, respectively. Results represent mean ± SD of n = 3 measurements (A, C), n = 3 NP batches (B) or n = 3 experiments (F-H). Levels of statistical significance are indicated as **p ≤ 0.01, ***p ≤ 0.001 and ****p ≤ 0.0001, ns: non-significant.

Table S2. Amount of OVA per mg NP, numbers of OVA per OVA-stL NP and surface coverage of NPs with ovalbumin. Results represent mean ± SD of n = 3 NP batches.

	µg OVA per mg NP	OVA per NP	surface coverage [%]
OVA NP	124 ± 5	1374 ± 302	96.5 ± 8.6

6 Antigen presentation by BMDCs

Table S3. Total number of lymphocytes and activated OTI T cells (CD44$^+$CD3$^+$CD8$^+$) after co-culture with BMDCs incubated with different NP formulations and CpG ODN1826.

NP formulation	Total number of activated OTI T cells	Total number of lymphocytes
PBS	838 ± 72	36589 ± 559
CatS subs NP	707 ± 359	33774 ± 145
stL NP	445 ± 30	33655 ± 645
OVA NP	46534 ± 620	102530 ± 2703
OVA-stL NP	47152 ± 994	121466 ± 3164

7 Supplementary Methods

7.1 Synthesis of cathepsin S substrate-PEG-PLGA

Block copolymer (3.9 µmol) was activated with EDC (97.5 µmol) and NHS (97.5 µmol) in N,N-dimethylformamide (DMF) for 2 h at room temperature. Cathepsin S substrate (5.85 µmol) dissolved in DMF was incubated with dithiothreitol (DTT) (58.5 µmol) for 1 h to reduce disulfide bonds of formed dimers. After EDC/NHS reaction was quenched with 2-mercaptoethanol (195 µmol), cathepsin S substrate-DTT mixture and N,N-diiso-propylethylamine (DIPEA) (39 µmol) were added dropwise and stirred for 72 h at room temperature. Resulting polymer was purified by precipitation in diethyl ether, followed by dialysis against Millipore water using a 6-8 kDa molecular weight cut-off regenerated cellulose dialysis membrane (Spectrum Laboratories Inc., Rancho Dominguez, CA, USA) over 24 hours to remove unbound ligands and reactants.

7.2   Calculation of the number concentration of the nanoparticles

Number concentration of the nanoparticles was calculated after Wen *et al.* [1] using equation 1. c_m is the mass concentration of the particles obtained by correlating the PEG content of the particles, quantified by a colorimetric iodine complexing assay [2], with the exact nanoparticle mass determined gravimetrically after lyophilization, as described before [3]. m_{NP} is the mass of one nanoparticle, which in turn was calculated with equation 2, where ρ_{NP} is the density of the NPs (1.3 g/cm³) [4] and d_{NP} is the hydrodynamic diameter of the particles determined through DLS measurements.

$$c_N = {c_m}/{m_{NP}} \quad (1)$$

$$m_{NP} = \rho_{NP} \cdot {4}/{3}\,\pi \left({d_{NP}}/{2}\right)^3 \quad (2)$$

Calculation of the amount of OVA for conjugation reaction

Prior to conjugation reaction, size and NP concentration of TCEP-reduced and purified CatS subs NPs were determined.

NP surface area was calculated assuming a spherical shape after equation 3, where d_{NP} is the hydrodynamic diameter of the NPs determined through DLS measurements.

$$SA_{NP} = 4\pi \left({d_{NP}}/{2}\right)^2 \quad (3)$$

The surface area occupied by one ovalbumin was calculated according to equation 4 based on dimensions information from literature [5]. The larger dimensions were used as basis for the calculation so that the maximum area occupied by one protein was determined.

$$A_{OVA_{max}} = 7.0\,nm \cdot 3.6\,nm = 25.2\,nm^2 \quad (4)$$

Number of proteins that can be coupled in a monolayer to nanoparticle surface was calculated by dividing available particle surface area by the maximum area occupied by one OVA (equation 5).

$$N_{OVA}/{NP} = {SA_{NP}}/{A_{OVA_{max}}} \quad (5)$$

Number of proteins per particle was converted to the mass of OVA per nanoparticle based on molecular weight (MW_{OVA}=45,000 g/mol) and Avogadro number (N_A=6.022 $\cdot 10^{23}$ 1/mol) (equation 6).

$$m_{OVA}/NP = \frac{N_{OVA}/NP}{N_A} \cdot MW_{OVA} \quad (6)$$

Finally, the mass of OVA required for the coupling reaction was determined after equation 7, where m_{NP} is the mass of one nanoparticle calculated as described in the section above, V is the volume of the reaction mixture and c_m is the mass concentration of the nanoparticles determined by an iodine assay.

$$m_{OVA} = \frac{V \cdot c_m \cdot m_{OVA}/NP}{m_{NP}} \quad (7)$$

7.3 Preparation and characterization of nanoparticles with stable linker

For intracellular antigen localization and cross-presentation assay, control particles with a stable, non-cleavable linker were prepared. NP preparation and characterization were performed in the same manner as for the NPs with CatS subs as linker, as described in the main text. In brief, GRKWPLPWPMGEC-DArg-NH₂ (stable linker) (customer synthesis Genscript, Piscataway, NJ, USA) was conjugated *via* its lysine residue to HOOC-PEG$_{5k}$-PLGA$_{13.1k}$ using EDC/NHS chemistry. Afterwards stable linker nanoparticles (stL NPs) were prepared through nanoprecipitation and Imject™ maleimide activated ovalbumin was covalently coupled to the cysteine residue of the stable linker on particle surface using maleimide thiol conjugation chemistry. Size and zeta potential were measured using a Malvern ZetaSizer Nano ZS (Malvern Instruments GmbH, Lappersdorf, Germany). NP concentration was calculated from the determined PEG content, as described above. The amount of stable linker and OVA was quantified with a Pierce BCA Protein Assay Kit, using stable linker and OVA as standards and covalent attachment of OVA was verified using SDS-PAGE.

8 References

1. Wen C-Y, Tang M, Hu J, et al. Determination of the Absolute Number Concentration of Nanoparticles and the Active Affinity Sites on Their Surfaces. *Anal Chem*. 2016; 88: 10134–10142.

2. Childs CE. The determination of polyethylene glycol in gamma globulin solutions. *Microchemical Journal*. 1975; 20: 190–192.

3. Abstiens K, Gregoritza M, Goepferich AM. Ligand Density and Linker Length are Critical Factors for Multivalent Nanoparticle-Receptor Interactions. *ACS Appl Mater Interfaces*. 2019; 11: 1311–1320.

4. Gholizadeh S, Kamps JAAM, Hennink WE, Kok RJ. PLGA-PEG nanoparticles for targeted delivery of the mTOR/PI3kinase inhibitor dactolisib to inflamed endothelium. *Int J Pharm*. 2018; 548: 747–758.

5. Erickson HP. Size and shape of protein molecules at the nanometer level determined by sedimentation, gel filtration, and electron microscopy. *Biol Proced Online*. 2009; 11: 32–51.

Chapter 5

pH-sensitive release of

click chemistry-conjugated proteins

from nanoparticles

Abstract

The functionalization of nanoparticles with biomolecules such as proteins and peptides is of great interest for a lot of applications. Protein-decorated particles are used for targeting, to overcome barriers in the body or to mimic pathogens. In addition to the conjugation strategy, it is crucial for many nanoparticulate platforms that the cargo can be released again in a controlled manner. Here, pH-sensitive release mechanisms are particularly popular. The aim of this study was to develop protein-functionalized polymeric nanoparticles that offer a pH-sensitive release mechanism. To do this, ovalbumin as a model protein was conjugated to block copolymer particles *via* a peptide linker using visible-light induced copper-free click chemistry. The reaction used was selective, fast, high yielding and moreover the bond formed was an acid-degradable triazoline structure. The release studies revealed that the proteins are released at slightly acidic pH values. However, protein release at neutral pH and a decrease in release in more acidic environments were also seen. Therefore, further optimizations are required for a fully controlled release. The click reaction presented here offers a great tool for selective particle functionalization with proteins and subsequent pH-controlled release.

1   Introduction

Click chemistry is a powerful and popular tool for nanoparticle (NP) modification. Click reactions form covalent bonds, are highly selective, have very fast reaction kinetics with high yields, and also work in a variety of solvents and in the presence of many other functional groups [1–4]. Click reactions can be classified in four major groups: 1) Cycloadditions like Diels-Alder reaction or Cu-catalyzed Huisgen reaction of azides and alkynes, 2) nucleophilic ring openings between a nucleophile and a strained electrophile such as an epoxide or aziridine, 3) non-aldol carbonyl chemistry involving, for example, the formation of hydrazones from carbonyls and hydrazines, and 4) carbon multiple bond additions such as certain Michael additions [5]. The most common click reaction is the copper-catalyzed cycloaddition between azide and alkyne [5]. This reaction is extensively researched, well established, there is a lot of literature, and it is often used in the surface modification of NPs [6–8]. However, the copper catalyst is problematic, especially when the particles are later used in biological, biomedical and pharmaceutical applications, since residual Cu is toxic to living systems [9]. In order to avoid copper catalysis, new approaches like the strain-promoted click reaction were developed. Here, educts with a high reactivity such as strained alkynes are used. The intramolecular strain of the reactant, which is the driving force for the reaction, eliminated the need for a catalyst [10]. However, due to their high reactivity, these educts can also easily react with other biological functionalities such as thiols in proteins, making the reaction less selective [11]. Therefore, researchers developed a next stage where they used high-energy ultraviolet (UV) light to generate a highly reactive molecule *in situ* from an unreactive precursor, allowing a well-controllable reaction [12] and avoiding side reactions with other functional groups. However, this approach cannot be used for conjugation of proteins, antibodies or other biological substances to NPs, since UV light can damage the functional structures of proteins [13].

However, Singh *et al.* developed an interesting new click chemistry in which they used a photocatalyst and visible light to generate the reactive molecule and thus induce the click reaction [14]. As shown in Scheme 1, they used primarily unreactive cycloalkenes as strain-loadable molecules and irradiated them with a blue light emitting diode (LED) in presence of an iridium-based photocatalyst. The double bond of the cycloalkene then undergoes isomerization, leading to intramolecular strain as the cycle is stiffened by direct fusion with the aryl group. The intramolecular strain makes the alkene highly reactive, allowing it to easily react with an azide in a click reaction, finally forming a

triazoline. The molecular strain is the driving force of the click reaction and is strong enough that no catalyst is needed for the click reaction. [14]
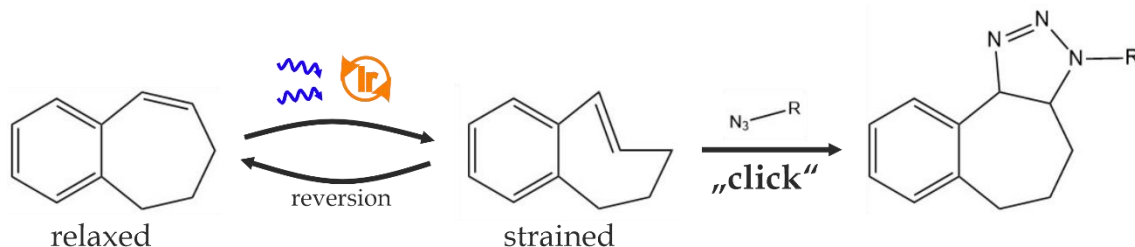
Scheme 1. Mechanism of click reaction discovered by Singh *et al.* [14]. Cycloalkene undergoes double-bond isomerization after irradiation with blue light in the presence of a photocatalyst. The induced molecular strain drives the copper-free click reaction of the strained alkene with an azide, resulting in a triazoline.

This new click reaction overcomes all the disadvantages of the previous approaches. First, the relaxed cycloalkene and the azide are unreactive towards other functional groups. Second, visible light and not UV light is used to unmask the reactive molecule, allowing its use for bioconjugations. And third, no catalyst, especially copper catalyst, is required, since the molecular strain is strong enough to drive the click reaction. [14] All these advantages make this click reaction very attractive for NP modification, especially when coupling proteins or other complex biomolecules.

Furthermore, Singh *et al.* have shown that the triazoline structure formed through the reaction is degraded in acidic media, allowing controlled pH-sensitive release of the cargo [14]. Controlled release mechanisms, especially acid-driven releases, are of great interest for a lot of medical applications. For example, tumor tissue (pH 6.5-6.9) [15] and also inflamed tissue (pH 6.0-7.0) [16] is characterized by an acidic environment. A pH-sensitive release mechanism, which releases the therapeutic agent in slightly acidic conditions, offers the possibility to protect the active agent from degradation during *in vivo* circulation [15] and only release it at the desired tissue. In the case of tumor therapeutics, it enhances the drug concentration in the target tissue, enables a dose reduction, improves the efficacy of tumor therapy and reduces side effects [17]. The same effects have also been observed for pH-sensitive release of anti-inflammatory drugs [18].

Additionally, there are different compartments inside cells having different pH values. For example endosomes have a pH around 6.5, lysosomes are more acidic (pH 4.5) and cytoplasm, in turn, is in the physiological range at 7.0 [19]. Through pH-controlled release mechanisms it is possible to release the payload in a specific cell compartment. Such a defined intracellular cargo release is of particular interest for vaccines. Depending

on the antigen localization in antigen-presenting cells, different processing routes are induced, resulting in different antigen presentation modes and immune responses. Antigens present in the cytosol are degraded by the proteasome and presented on MHC-I molecules, while antigens located in the endo-lysosomal compartments are loaded primarily on MHC-II molecules [20]. However, here the endosomal antigens can also be loaded onto MHC-I molecules after endosomal escape, a process called cross-presentation. On the other hand, antigens in late endosomes and lysosomes are loaded onto MHC-II [21]. Acid-labile vaccine carrier systems showed increased cellular immunity due to enhanced cross-presentation after antigen escape into the cytoplasm [22]. For the particles used in this study made of polymeric core, enzyme-cleavable peptide linker and protein, our group has previously shown an increased cross-presentation on dendritic cells due to the enzyme-triggered protein release in the early endosome and subsequent endosomal escape [23]. It is hypothesized that the additional integration of the click reaction-formed triazoline structure as an acid-cleavable group may further enhance cross-presentation, since then two mechanisms – one enzyme- and one pH-induced – trigger protein release in the early endosome, resulting in more released protein that may undergo endosomal escape with following MHC-I presentation.

The aim of this study was to use the click reaction of Singh *et al.* to modify polymeric NPs. First, the strain-loadable alkene structure was synthesized and extensively characterized, and then coupled to the NP-forming polymer. The click-reaction was optimized for use in bioconjugation and then used to synthesize a polymer-peptide-conjugate with which finally NPs were prepared. After coupling ovalbumin (OVA) as model protein to the particle, the pH-sensitivity of the triazoline structure was investigated as possible release mechanism for the protein.

2 Materials and Methods

2.1 Materials

Carboxylic acid-terminated poly(ethylene glycol) (HOOC-PEG-OH) with a molecular weight of 5000 Da was obtained from JenKem Technology USA Inc. (Allen, TX, USA). Azide-modified Cathepsin S substrate (CatS subs azide; amino acid sequence GR-Lys(N$_3$)-WPPMGLPWEC-DArg-NH$_2$) was synthesized by Thermo Fisher Scientific (Darmstadt, Germany). Pierce™ BCA protein assay kit and Imject™ maleimide-

activated ovalbumin (Mal-OVA) were purchased from Thermo Fisher Scientific (Waltham, MA, USA). Tris(2-carboxyethyl)phosphine (TCEP) and sodium chloride (NaCl) were obtained from Carl Roth GmbH + Co. KG (Karlsruhe, Germany). Resomer® RG 752 H poly(lactic-co-glycolic acid) (PLGA) and all other materials and reagents were purchased from Sigma Aldrich (Taufkirchen, Germany). Millipore water used for dialysis and buffer preparation was obtained from a Millipore Milli-Q water purification system (Billerica, MA, USA). The phagolysosomal simulant fluid (PSF) used for protein release was a 0.02 M potassium hydrogen phthalate buffer with 1 mM Na_2HPO_4, 114 mM NaCl, 0.5 mM Na_2SO_4, 0.2 mM $CaCl_2$ and 6 mM glycine [24]. pH was adjusted with NaOH and HCl.

2.2   Synthesis and characterization of 6,7-dihydro-5H-benzo[7]annulene-2-amine

6,7-Dihydro-5H-benzo[7]annulene-2-amine (aminobenzocycloheptene, H_2N-BC7) was synthesized according to Singh *et al.* [14] with slight modifications. Briefly, 6,7,8,9-tetrahydro-5H-benzo[7]annulene-5-one (1-benzosuberone; 6.25 mmol) and concentrated sulfuric acid (conc. H_2SO_4; 15.5 ml) were placed in a round bottom flask. After cooling the mixture to 0 °C, potassium nitrate (KNO_3; 6.88 mmol) dissolved in conc. H_2SO_4 was added dropwise. The reaction mixture was stirred for 2 h at 0 °C. Then the solution was added into an ice-water mixture (150 ml) and stirred for 30 min. Thereafter, the aqueous phase was extracted with ethyl acetate (EtOAc) which was then washed with brine and dried over sodium sulfate (Na_2SO_4). After vacuum concentration, the crude product was purified by column chromatography (stationary phase: silica gel, mobile phase: EtOAc/hexane = 30/70) to get 3-nitro-6,7,8,9-tetrahydro-5H-benzo[7]annulene-5-one (3-nitrobenzosuberone).

3-Nitrobenzosuberone (1.02 mmol) was placed in a dried round bottom flask (dried overnight at 180 °C) and dissolved in ethanol (EtOH; 0.09 mol). After addition of a saturated copper(II)acetate solution in EtOH (4.2 ml), sodium borohydride ($NaBH_4$; 11.26 mmol) was added portionwise to the mixture and left stirred for 3 h at room temperature. Then brine (10 ml) was added and EtOH removed under reduced pressure. The residue was dissolved in EtOAc (100 ml) and washed with brine (50 ml) and a saturated sodium hydrogen carbonate solution (50 ml). The organic phase was dried over Na_2SO_4 prior to concentrating under vacuum to obtain 3-amino-6,7,8,9-tetrahydro-5H-benzo[7]anuulene-5-ol (aminobenzocycloheptanol).

Aminobenzocycloheptanol used without further purification (0.68 mmol) was dissolved in 6 N HCl (3.8 ml). After reacting at 90 °C for 6 h, the mixture was cooled to room temperature and neutralized using 1 M NaOH. The aqueous phase was then extracted with EtOAc (3x 30 ml). Finally, the organic phase was dried over Na_2SO_4, concentrated under vacuum and purified by column chromatography (silica gel, EtOAc/hexane = 30/70) to get 6,7-dihydro-5H-benzo[7]annulene-2-amine (aminobenzocycloheptene, H_2N-BC7).

3-Nitro-6,7,8,9-tetrahydro-5H-benzo[7]annulene-5-one, 3-amino-6,7,8,9-tetrahydro-5H-benzo[7]anuulene-5-ol and 6,7-dihydro-5H-benzo[7]annulene-2-amine have been extensively characterized. After evaluation of physical states and colors, ^{1}H-NMR spectra were recorded at 295 K using a Bruker Avance 300 spectrometer (Bruker BioSpin GmbH, Rheinstetten, Germany) with $CDCl_3$ or d_6-DMSO as solvents. Furthermore, melting points were determined with a DSC 2920 differential scanning calorimeter (UB TA Instruments, Eschborn, Germany) and infrared (IR) spectra were measured on a Cary 630 FTIR spectrometer (Agilent Technologies GmbH, Waldbronn, Germany) over the wavenumber range 4000–650 cm^{-1}. Finally, UV-vis absorbance spectra (220-800 nm) were recorded using a FLUOstar Omega microplate reader (BMG Labtech, Ortenberg, Germany).

2.3 Synthesis of BC7-PEG-PLGA

HOOC-PEG-PLGA block copolymer was synthesized *via* ring-opening polymerization after Qian *et al.* [25] with slight modifications. Macroinitiator HOOC-PEG-OH (1 equivalent = equiv) was mixed with lactide (140 equiv) and after addition of catalyst 1,8-diazabicyclo[5.4.0]undec-7-ene (3 equiv), glycolide (29 equiv) was added at a constant rate of 1.2 ml/min over 10 min. After quenching the reaction with benzoic acid (15 equiv), resulting block copolymer was precipitated in diethyl ether and dried under vacuum. Subsequently, HOOC-PEG-PLGA was activated with a 50-fold molar excess of ethyl-3-(3-dimethylaminopropyl)carbodiimide/N-hydroxysuccinimide (EDC/NHS) for 2 h in dichloromethane (DCM). Then, diisopropylethylamine (DIPEA) and a 3-fold molar excess of H_2N-BC7 were added dropwise and allowed to react for 72 h at room temperature. After precipitation in diethyl ether, resulting BC7-PEG-PLGA was purified through dialysis against Millipore water using a 6-8 kDa molecular weight cut-off

regenerated cellulose dialysis membrane (Spectrum Laboratories Inc., Rancho Dominguez, CA, USA) over 34 h.

Coupling efficiency was assessed by measuring the concentration of polymer and benzocycloheptene (BC7). Polymer concentration was determined gravimetrically after lyophilization and BC7 content was quantified by measuring absorbance at 308 nm after polymer dissolution in acetonitrile (ACN) using a FLUOstar Omega microplate reader (BMG Labtech, Ortenberg, Germany).

2.4   Click reaction

Click reaction of azide-modified CatS substrate (CatS subs azide) with BC7-PEG-PGLA was performed by adapting a protocol described by Singh *et al.* [14] (please refer to supporting information for optimization studies). In short, BC7-PEG-PLGA (1.61 µmol) and CatS Subs-N_3 (2.76 µmol) were mixed and dissolved in dimethylformamide (DMF). $Ir(p\text{-}CF_3\text{-}ppy)_3$ (1.2 mol%) was added as a photocatalyst and reaction mixture was placed in the light bath (Figure S1). After 2 h of reaction with 60% light intensity at room temperature, resulting CatS subs-PEG-PLGA was precipitated in diethyl ether and excess reactants were removed by dialysis against Millipore water using a 6-8 kDa molecular weight cut-off regenerated cellulose dialysis membrane (Spectrum Laboratories Inc., Rancho Dominguez, CA, USA) over 34 h.

To determine coupling efficiency, nanoparticles were prepared as described in the following section and CatS subs and PEG content were measured using Pierce™ BCA protein assay kit, following the manufacturer's instructions, and an iodine complexing assay [26], respectively. Absorbance measurements were performed with a FLUOstar Omega microplate reader (BMG Labtech, Ortenberg, Germany).

2.5   NP preparation and characterization

For NP preparation, CatS subs-PEG-PLGA and PLGA in ACN (10 mg/ml) were mixed at a 7:3 mass ratio. NPs were prepared *via* nanoprecipitation by adding the polymer mixture dropwise into 10 volumes of stirred 0.1X low-endotoxin Dulbecco's phosphate-buffered saline (LT-PBS) (v/v). Immediately after preparation, the NPs were diluted with an equal volume of 0.1X LT-PBS and purified and concentrated through

centrifugation at 1400 g using an Amicon® Ultra-15 MWCO 100 kDa centrifugal filter (Merck KGaA, Darmstadt, Germany).

NP size and polydispersity index (PDI) were evaluated by dynamic light scattering (DLS) using a Malvern ZetaSizer Nano ZS (Malvern Instruments GmbH, Lappersdorf, Germany). Samples were diluted in 0.1X LT-PBS and analyzed in disposable microcuvettes (Brand, Wertheim, Germany) at 25 °C.

Quantification of NP mass concentration was performed by correlation of particle PEG content, determined through the iodine complexing assay [26], and particle mass, determined gravimetrically after lyophilization, as previously described by our group [27]. The NP number concentration was calculated from the mass concentration, the particle density (1.3 g/cm^3) [28] and the NP size assuming a spherical particle shape [29].

2.6   Conjugation of OVA

Maleimide thiol chemistry was used to couple Mal-OVA to the cysteine residue of CatS subs on the particle surface. For this purpose, freshly prepared CatS subs NPs were reduced with TCEP (50 equiv relative to CatS subs). After 2 h incubation and purification *via* ultracentrifugation at 1400 g with an Amicon® Ultra-15 MWCO 100 kDa centrifugal filter (Merck KGaA, Darmstadt, Germany), the particles were resuspended in LT-PBS, Mal-OVA was added and left reacting for 4 h at room temperature. Mal-OVA amount was calculated based on the NP surface area and protein size, and corresponds to the amount forming a protein monolayer on the surface. Finally, OVA NPs were washed with 0.1X LT-PBS by ultracentrifugation as described above.

Hydrodynamic diameter, PDI and NP concentration were determined as described above. The amount of OVA conjugated to the NPs was determined using a Pierce™ BCA protein assay kit according to the manufacturer's instructions. OVA was used as standard and the absorbance was measured with a FLUOstar Omega microplate reader (BMG Labtech, Ortenberg, Germany). OVA amount was calculated by subtracting the absorbance of CatS subs NPs from the absorbance of OVA NPs.

2.7 Protein release

In order to determine pH-dependent decomposition of the triazoline structure with subsequent OVA release, a protein release assay was performed. OVA NPs were diluted with PSF at various pH values (5.0-8.0) to a final concentration of 4 mg/ml (175 µl) and incubated for 2 h at room temperature with shaking. Afterwards, NPs were washed three times with Millipore water by ultracentrifugation with an Amicon® Ultra-15 MWCO 100 kDa centrifugal filter (Merck KGaA, Darmstadt, Germany) at 2200 g. Finally, NP size and PDI as well as particle concentration and OVA amount were determined as described above. Untreated OVA NPs served as control. Released OVA was calculated as the difference in the OVA amount of untreated and treated NPs relative to the initial OVA amount (corresponds to the OVA amount of untreated NPs).

3 Results

3.1 Synthesis and characterization of H_2N-BC7

Since the mild light-induced click reaction developed by Singh *et al.* should be used to couple CatS subs to the NP-forming polymer, the aminobenzocycloheptene (H_2N-BC7) was synthesized first. This is the strain-loadable alkene required for the light-induced click reaction with azides, with an integrated amine group which in turn was needed for conjugation to the polymer. H_2N-BC7 was synthesized in three steps and both the intermediates and the final product were extensively characterized (Figure 1).

The first synthesis step was the nitration of 1-benzosuberone with KNO_3-H_2SO_4 at low temperature (Figure 1A), resulting in a white to yellow solid with a molecular weight of 205.22 g/mol and a melting point at 94.03 °C (Figure 1B). UV-vis spectrum of this compound (Figure 1C) displayed a characteristic maximum at 270 nm, which is attributed to the nitro-substituted benzene ring of the molecule [30]. The identity of this first intermediate was determined by ^{1}H-NMR and IR. As shown in Figure 1D, the ^{1}H-NMR spectrum displayed peaks at δ 1.85, 2.76 and 3.00 assigned to the aliphatic protons of the cycloheptanone and at δ 7.35, 8.21 and 8.15 attributed to the aromatic protons of the benzene. The IR data (Table 1 and Figure 1E) exhibited bands characteristic for this molecule at 1673 cm^{-1}, corresponding to C=O stretching vibrations, and at 1521 cm^{-1} and 1342 cm^{-1}, which were assigned to N-O stretching vibrations.

In the second synthesis step, the 3-nitrobenzosuberone was reduced using $NaBH_4$ as reducing agent, thereby reducing the ketone to an alcohol and the nitro group to an

amine (Figure 1F). The product obtained was again a white to yellow solid and had a molecular weight of 177.25 g/mol. The melting point was measured as 163.93 °C (Figure 1G).The maximum visible in the UV-vis spectrum (Figure 1H) at 290 nm was assigned to the aniline structure in the molecule [30]. Again, ^{1}H-NMR and IR revealed the structure of synthesis product. The peaks at δ 1.17, 1.47, 1.65, 1.85, 2.50 and 4.56 in the ^{1}H-NMR spectrum (Figure 1I) were attributed to the aliphatic protons, peaks at δ 6.26, 6.68 and 6.72 corresponded to the aromatic protons and peaks at δ 5.00 were assigned to the amine and the alcohol. IR spectrum and absorptions of the second intermediate are shown in Figure 1J and Table 1. Compared to the IR spectrum of the educt, the C=O and N-O stretching bands disappeared, while characteristic absorption bands at 3362 cm^{-1} corresponding to N-H stretching vibrations, 3295 cm^{-1} assigned to O-H stretching vibrations, 1439 cm^{-1} attributed to C-N stretching vibrations, and 1297 cm^{-1} which were from C-O stretching vibrations were found.

Finally, as the last synthesis step, aminobenzocycloheptanol was heated in the presence of hydrochloric acid, which led to dehydration of the alcohol and formation of a double bond (Figure 1K). The resulting yellow to brown oil (M = 159.23 g/mol) with a melting point at -46.74 °C (Figure 1L) displayed a right-shifted maximum at 308 nm in the UV-vis spectrum (Figure 1M) compared to the educt, due to the double bond extending the conjugated system. ^{1}H-NMR spectrum (Figure 1N) exhibited characteristic peaks confirming the successful synthesis of aminobenzocycloheptene. The proton peaks at δ 1.92, 2.39 and 2.75 were attributed to the aliphatic protons, whereas the peak at δ 4.08 corresponded to the amine. Proton peaks at δ 5.88 and 6.59 were assigned to the double bond and peaks at δ 6.29, 6.53 and 6.90 were from aromatic protons. IR data (Figure 1O and Table 1) was used to uniquely identify the compound. Here the O-H and C-O stretching bands were no longer detectable, while additional stretching vibrations for the double bond were detectable in the region of the aromatic vibrations.

Table 1. IR data of 3-nitrobenzosuberone, aminobenzocycloheptanol and aminobenzocycloheptene.

Compound	IR ν (cm^{-1})
3-Nitrobenzosuberone	3093, 1610, 1521 (aromatics); 2993, 2866 (aliphatics); 1673 (C=O); 1521, 1342 (NO$_2$)
Aminobenzocycloheptanol	3362 (NH$_2$); 3295 (OH); 3112, 1610, 1584 (aromatics); 2930, 2851 (aliphatics); 1439 (C-N); 1297 (C-O)
Aminobenzocycloheptene	3422, 3347 (NH$_2$); 3213, 3008, 1610, 1502 (aromatics, olefins); 2922, 2855 (aliphatics); 1446 (C-N)

Figure 1. Synthesis and characterization of 3-nitrobenzosuberone, aminobenzocycloheptanol and aminobenzocycloheptene. (A, F, K) Synthesis steps, (B, G, L) appearance, molecular weight and melting point, (C, H, M) UV-vis spectra, (D, I, N) ^{1}H-NMR spectra and (E, J, O) IR spectra of each compound.

3.2 Development of NPs with click-chemistry conjugated proteins

In order to create NPs with surface-conjugated proteins using light-induced click-chemistry, the synthesized H_2N-BC7 was first coupled to HOOC-PEG-PLGA by EDC/NHS reaction (Figure 2A). The degree of functionalization was approximately 93% as determined by measuring molar content of polymer and BC7 *via* polymer mass and BC7 absorbance, respectively (Figure 2B).
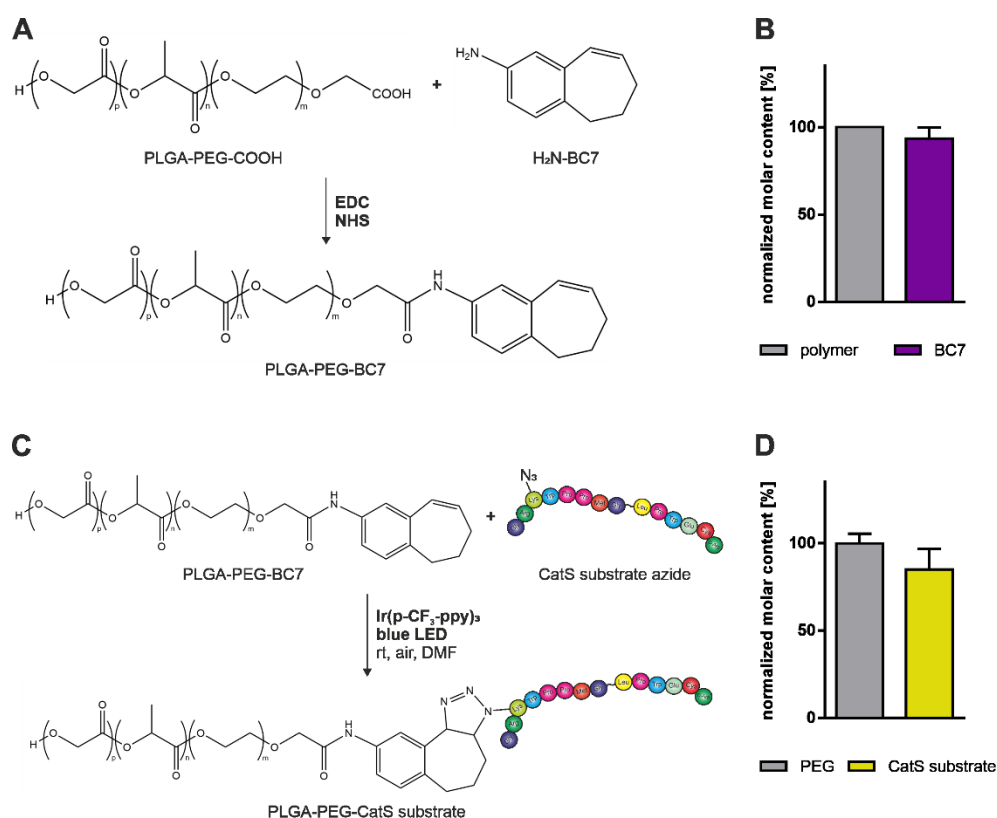
Figure 2. Coupling of peptide linker to PEG-PLGA using click chemistry. (A) Conjugation of H_2N-BC7 to block copolymer using EDC/NHS chemistry. (B) Molar content of polymer and BC7 normalized to polymer content. (C) Light-induced click reaction of PLGA-PEG-BC7 with CatS subs azide. (D) Molar content of PEG and CatS subs normalized to PEG content. Results represent mean ± SD of n = 3 measurements.

Then the peptide linker CatS subs azide was conjugated to BC7-PEG-PLGA *via* a light-induced click reaction (Figure 2C). Beforehand, optimization studies were performed with cRGDfK(N_3) as azide to find the best reaction conditions for click reaction (please refer to supplementary methods for detailed description). First, the correlation between the light intensity settable on the lamp, with which the light bath for the reaction was generated, and the final irradiance, which was measured with a radiometer, was

determined. As shown in Figure S2, there is a linear correlation between set light intensity and emitted irradiance from 10% to 90% light intensity. Below 10% no irradiance was measurable and above 90% light intensity no further increase in irradiance was detectable. For this reason, it was decided to test three light intensities, 30, 60 and 90%, in the optimization studies. Furthermore, different reaction times (1-24 h) and various molar ratios of azide to BC7 (2:1-1:3) were investigated. Regarding the reaction times, 2 h showed the best results (Figure S3A). The content of conjugated cRGDfK was 2- to 4- fold higher than for the other reaction times. For the molar ratio of azide to BC7, the two-fold molar excess of azide led to the highest amount of coupled cRGDfK (Figure S3B), while in terms of light intensity the best result was achieved with 60% (Figure S3C).

Then CatS subs azide was conjugated to BC7-PEG-PLGA using the ideal reaction conditions (2 h reaction time, 2:1 azide:BC7, 60% light intensity) (Figure 2C). The overall coupling efficiency, determined by measuring PEG content and CatS subs content of CatS subs NPs by iodine complexing assay BCA assay, was 85%. Accordingly, coupling efficiency of the click reaction alone was ~91%.

Next, CatS Subs NPs were prepared through nanoprecipitation in 0.1X PBS and OVA was conjugated to the particle surface by maleimide thiol conjugation in PBS, where maleimide-activated OVA reacted with the thiol in the cysteine of CatS subs and formed a covalent thioether bond (Figure 3A). As shown in Figure 3B, NP size increased after conjugation of OVA, and both protein-free and protein-bearing NPs had a narrow size distribution (PDI ~0.1). The amount of OVA was determined to be 65 µg per mg NP, corresponding to 231 OVA molecules per NP (Figure 3C).
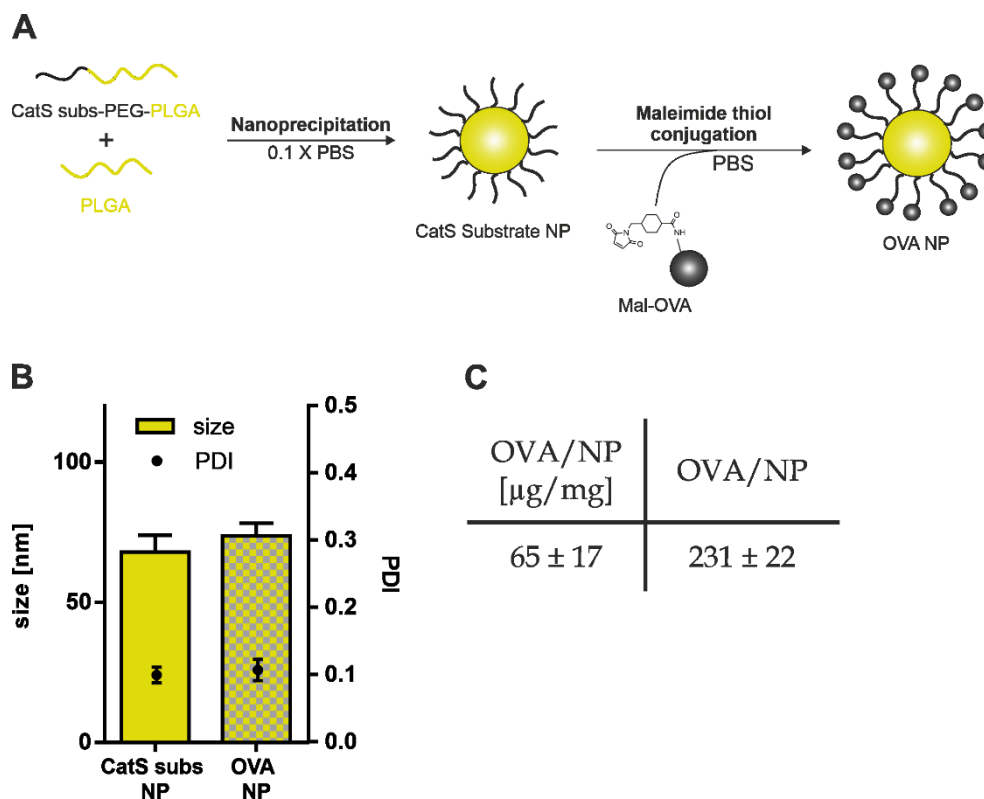
Figure 3. NP preparation and characterization. (A) Manufacturing of CatS subs NPs *via* nanoprecipitation and subsequent conjugation of OVA by maleimide thiol conjugation. (B) Size and PDI of the prepared NPs. (C) Amount and number of OVA on OVA-NPs. Results represent mean ± SD of n = 3 measurements.

3.3   pH-sensitive protein release from NPs

Finally, in order to study OVA release from NPs as a result of decomposition of the triazoline structure in acidic environment, OVA NPs were incubated at different pH values and particle size as well as the amount of released protein were determined. DLS measurements revealed no changes in NP size and PDI when comparing control NPs and incubated particles (Figure 4A). As shown in Figure 4B, protein was released from NPs after incubation at pH 7.5-6.0, while only slight release was detectable at pH 8.0. At more acidic pH values (5.5 and 5.0), OVA release decreased again.
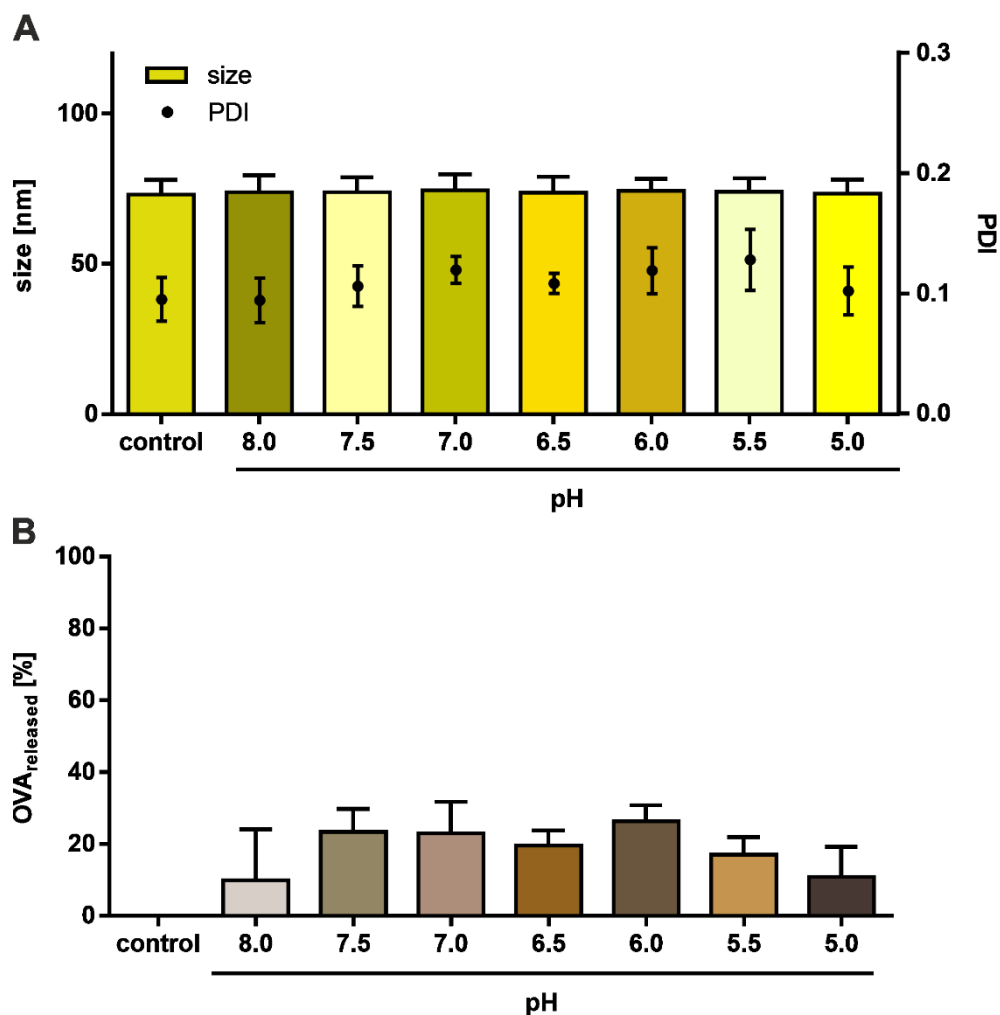
Figure 4. OVA release from NPs at different pH values. (A) NP size and PDI of OVA NPs and (B) percentage of OVA released after incubation at various pH values. Untreated OVA NPs were used as control. Results represent mean ± SD of n = 3 measurements.

4   Discussion

NPs with proteins and/or peptides on the surface have become indispensable for many medical applications. For example, proteins/peptides can be used to increase the stability of particles *in vivo* so that they reach the site of action intact [31]. Protein/peptide coatings can influence the formation of the protein corona by either preventing the adsorption of opsonins and subsequent recognition and clearance of the NPs by phagocytes, or by promoting the adsorption of dysopsonins, which inhibit recognition and elimination. Furthermore, peptides can be conjugated to the surface offering stealth properties similar to PEG, and 'self-peptides' can also be coupled,

through which the NPs can evade the phagocytes by pretending to be 'self'. [31] Additionally, protein and peptide functionalization is used to improve penetration into target cells or to overcome barriers in the body [31]. For example, conjugation of apolipoprotein E or α2-macroglobulin can improve transport across the blood-brain barrier [32, 33], while cell-penetrating peptides enhance uptake into cells in general [34]. In tumors, the penetration of NPs is often very poor due to dense cell growth and abnormal angiogenesis. Here, peptide/protein functionalization is very popular to increase the tumor penetration of drug-carrying NPs and thus improve the therapeutic effect and reduce side effects [35]. In addition, proteins and peptides are used for active targeting. There are numerous examples where peptides, proteins, protein domains, or antibodies have been used to target e.g. capillary endothelial cells, hepatocytes, tumors, atherosclerotic plaques and many other tissue and cell types [36, 37]. Another interesting area, in which protein-functionalized NPs are used, is the mimicking of pathogens [37]. On the one hand, this is used for vaccines, where the NPs are designed to mimic the pathogens in order to achieve immunization that closely resembles the natural immune response [38, 39]. On the other hand, biomimetic NPs are used to specifically deliver antiviral and antimicrobial agents to infected cells [39].

When choosing chemical reaction for the conjugation of proteins and peptides to NPs, several factors play an important role. The coupling reaction itself should be fast and selective and go to completion. Click reactions are a promising tool here. However, not all of the countless known click reactions are suitable for bioconjugation. Harsh reaction conditions such as a copper catalyst or high-energy UV light for reaction induction should not be used. The new visible-light induced and copper-free click reaction developed by Singh *et al.* [14] offers great potential to modify nanoparticles in a mild manner.

In addition to the coupling reaction, the resulting covalent bond plays an important role for later application. For example, NP vaccines used to induce a B cell response should offer a stable, unbreakable bond, since rigid highly repetitive antigens facilitate cross-linking of B cell receptors, resulting in a superior antibody response [40]. For other applications in turn, it is important that the payload is released again, i.e. the covalent bond can be broken again. This is crucial for therapeutics against cancer and inflammation, but also when the cargo is to be released in a specific cell organelle. The pH value is particularly popular as a release mechanism here, because the pH is altered in many pathophysiological processes [15, 16] and, as already mentioned, different cell

organelles have varying pH values [19]. Creating a covalent bond that is breakable at certain pH values has been part of NP research for a long time [41]. Here again, click reaction of Singh *et al.* is very interesting, since the formed triazoline structure is cleavable in acidic environment [14].

In this study, a polymeric NP system was developed with proteins conjugated to the surface *via* a peptide linker using, among others, the click reaction from Singh *et al.* [14]. It was shown that the mild visible-light induced and copper-free click reaction is suitable for bioconjugation. Contrary to expectations, protein release as a result of triazoline structure destruction was observed not only at acidic pH, but also at neutral, physiological pH.

First, aminobenzocycloheptene (H$_2$N-BC7), the strain-loadable alkene required for the click reaction, was successfully synthesized. Both the final product and the intermediates corresponded to the desired molecules, as confirmed by ^{1}H-NMR and IR measurements. Singh *et al.* [14] described the formation of a major regioisomer (3-nitrobenzosuberone) and a minor regioisomer (1-nitrobenzosuberone) in the first synthesis step. Therefore it was decided to separate the regioisomers using column chromatography and only proceed with the major isomer. The absence of additional, unassignable peaks and bands in the ^{1}H-NMR and IR spectra verified successful isolation of the major isomer. The final product H$_2$N-BC7 was also purified by chromatography. Here too, ^{1}H-NMR and IR measurements confirmed the successful removal of all by-products, excess reactants and solvents. The right shift of the maxima in the UV-vis spectra further proved successful synthesis. Finally, melting point, appearance and molecular weight were determined to fulfill a comprehensive chemical characterization of the intermediates and final product. Subsequently, the strain-loadable alkene was successfully integrated into the NPs. The block copolymers were almost completely functionalized with H$_2$N-BC7 by EDC/NHS reaction.

Due to the good controllability of the reaction and the mild reaction conditions with nevertheless high selectivity, fast reaction kinetics, and high yield, the visible-light induced copper-free click reaction described by Singh *et al.* [14] offered a very attractive tool for bioconjugation of proteins/peptides and polymer particles. However, the reaction first had to be adjusted and optimized, since Singh *et al.* did not test the coupling of polymers and peptides/proteins. The group only worked with small molecules, which often behave quite differently from macromolecules in chemical reactions. Indeed, they have shown the functionalization of insulin with biotin by the new click

reaction, which most closely resembles the reaction setup used here, but they used different reaction conditions than previously postulated for the small molecules, and the reaction of a 5 kDa insulin with a 0.2 kDa biotin is not readily transferrable to the coupling of 2 kDa CatS subs to a 20 kDa block co-polymer. Factors such as steric hindrance, viscosity or solubility are fundamentally different and have a major impact on the progress of the reaction. Therefore, it was decided to first optimize the click reaction for the coupling of polymers and peptides in terms of reaction time, molar ratios and light intensity using cRGDfK as model peptide (please refer to supporting information for optimization studies). Regarding rection time, 2 h achieved the best results. The shorter time of 1 h was probably too short to allow the reaction to go to completion, while longer reaction times likely led to decomposition of the product, which in turn reduced the yields. In contrast to Singh *et al.*, who always used an excess of BC7 [14], the best coupling efficiencies were obtained with a two-fold molar excess of azide to alkene. In terms of light intensities, 60% turned out to be best. At 30%, the irradiation was probably too low to induce alkene isomerization and thus the reaction, while at 90% likely product destruction occurred. For subsequent coupling of the peptide linker CatS subs to BC7-PEG-PLGA, a coupling efficiency of 91% was achieved for the click reaction alone. Here, further optimizations would be necessary for a 100% conversion.

After NP preparation through nanoprecipitation, model protein OVA was coupled to the particle surface by maleimide thiol conjugation. From the large number of possible conjugation strategies [42] it was decided to use maleimide thiol conjugation as it offers several advantageous. First, reaction works under mild conditions, that is, at room temperature, in aqueous buffers and at physiological pH [43]. This ensured protein and particle stability during the reaction, as PEG-PLGA NPs show good colloidal stability under these conditions and proteins, in turn, exist in their native from in aqueous media under physiological conditions [44, 45]. In addition, maleimides show the best selectivity towards thiols at physiological pH values between 6.5 and 7.5 [46], which further increases the attractiveness of the reaction since little or no side reactions occur. Finally, the thioether formed represents a covalent and relatively stable bond [43]. This allows the protein release to be controlled, since the triazoline formed in the click reaction is the only instable structure in the particle. Moreover, the maleimide thiol reaction is well-established, so numerous good working protocols can be found in literature that save the time-consuming establishment of the conjugation reaction. An established protocol was used to couple maleimide-activated OVA to the thiols on the particles surface and

an increase in size after coupling was observed, indicating successful protein conjugation.

Finally, the pH-sensitive release of the conjugated proteins was examined. It was investigated whether OVA is released from the particles at acidic pH values as a result of cleavage of the triazoline structure formed in the click reaction. The size measurements revealed that the hydrodynamic diameter and PDI of the particles remained the same before and after incubation at each pH, indicating that the NPs were stable and did not aggregate or degrade. Results of the release experiment showed that the proteins are released in acidic environments at pH < 7. However, OVA delivery was also detected at neutral pH levels of 7.0-8.0. At pH 5.5 and 5.0 the release of the proteins decreased again. The decreased release at more acidic pH is likely due to electrostatic interactions between OVA and PLGA. At lower pH values, the positive partial charges in OVA increase while PLGA with its pK_a of 3.85 is negatively charged [47]. Thus, protein release is presumably hindered since OVA adsorbed to PLGA *via* electrostatic interactions. Overall, the protein is released in slightly acidic environments, useful for delivery in cancerous tissues or for controlled release in the early endosomes. However, the release already at physiological pH values is problematic, since the proteins are probably already delivered in the blood during *in vivo* applications. Thus, the cargo cannot yet be released in an acid-controlled manner and further investigations are urgently required to optimize the release.

5 Conclusion

Taken together, in this study it was shown that the visible-light harvesting copper-free click reaction by Singh *et al.* is suitable for bioconjugations. The reaction was successfully adapted for the coupling of peptides to polymers. This advanced click reaction offers a new interesting conjugation strategy for selective, fast, and mild NP functionalization with biomolecules. Furthermore, the pH-sensitive release of the conjugated proteins was demonstrated. Although further studies and optimizations regarding the release are needed, the particle developed here represents a promising delivery platform for acid-controlled cargo release, which is particularly advantageous for use in cancer, inflammation or immunization. A possibly potentiating effect on the cross-presentation of the coupled proteins by dendritic cells through the acid-induced release also has to be investigated in further *in vitro* and *in vivo* tests.

References

1. Lutz J-F. 1,3-dipolar cycloadditions of azides and alkynes: a universal ligation tool in polymer and materials science. *Angew. Chem. Int. Ed.* 2007; 46: 1018–1025.

2. Kolb HC, Finn MG, Sharpless KB. Click Chemistry: Diverse Chemical Function from a Few Good Reactions. *Angew. Chem. Int. Ed.* 2001; 40: 2004–2021.

3. Hawker CJ, Wooley KL. The convergence of synthetic organic and polymer chemistries. *Science*. 2005; 309: 1200–1205.

4. Geest BG de, van Camp W, Du Prez FE, Smedt SC de, Demeester J, Hennink WE. Biodegradable microcapsules designed via 'click' chemistry. *Chem Commun (Camb)*. 2008: 190–192.

5. Hein CD, Liu X-M, Wang D. Click chemistry, a powerful tool for pharmaceutical sciences. *Pharm Res*. 2008; 25: 2216–2230.

6. Yi G, Son J, Yoo J, Park C, Koo H. Application of click chemistry in nanoparticle modification and its targeted delivery. *Biomater Res*. 2018; 22: 13.

7. Li N, Binder WH. Click-chemistry for nanoparticle-modification. *J. Mater. Chem.* 2011; 21: 16717.

8. Yáñez-Sedeño P, González-Cortés A, Campuzano S, Pingarrón JM. Copper(I)-Catalyzed Click Chemistry as a Tool for the Functionalization of Nanomaterials and the Preparation of Electrochemical (Bio)Sensors. *Sensors (Basel)*. 2019; 19.

9. Pickens CJ, Johnson SN, Pressnall MM, Leon MA, Berkland CJ. Practical Considerations, Challenges, and Limitations of Bioconjugation via Azide-Alkyne Cycloaddition. *Bioconjug Chem*. 2018; 29: 686–701.

10. Baskin JM, Bertozzi CR. Copper-Free Click Chemistry. In: Lahann J, ed. *Click Chemistry for Biotechnology and Materials Science*. Chichester, UK: John Wiley & Sons, Ltd; 2009: 29–51.

11. van Geel R, Pruijn GJM, van Delft FL, Boelens WC. Preventing thiol-yne addition improves the specificity of strain-promoted azide-alkyne cycloaddition. *Bioconjug Chem*. 2012; 23: 392–398.

12. Arumugam S, Orski SV, Mbua NE, et al. Photo-click chemistry strategies for spatiotemporal control of metal-free ligation, labeling, and surface derivatization. *Pure and Applied Chemistry*. 2013; 85: 1499–1513.

13. Teresa M, Petersen S, Prakash G. UV Light Effects on Proteins: From Photochemistry to Nanomedicine. In: Saha S, ed. *Molecular Photochemistry - Various Aspects*. InTech; 2012.

14. Singh K, Fennell CJ, Coutsias EA, Latifi R, Hartson S, Weaver JD. Light Harvesting for Rapid and Selective Reactions: Click Chemistry with Strain-Loadable Alkenes. *Chem*. 2018; 4: 124–137.

15. Zhuo S, Zhang F, Yu J, Zhang X, Yang G, Liu X. pH-Sensitive Biomaterials for Drug Delivery. *Molecules*. 2020; 25.

16. Riemann A, Ihling A, Thomas J, Schneider B, Thews O, Gekle M. Acidic environment activates inflammatory programs in fibroblasts via a cAMP-MAPK pathway. *Biochim Biophys Acta*. 2015; 1853: 299–307.

17. Liu Y, Wang W, Yang J, Zhou C, Sun J. pH-sensitive polymeric micelles triggered drug release for extracellular and intracellular drug targeting delivery. *Asian Journal of Pharmaceutical Sciences*. 2013; 8: 159–167.

18. Libánská A, Randárová E, Lager F, Renault G, Scherman D, Etrych T. Polymer Nanomedicines with Ph-Sensitive Release of Dexamethasone for the Localized Treatment of Inflammation. *Pharmaceutics*. 2020; 12.

19. Hu Y-B, Dammer EB, Ren R-J, Wang G. The endosomal-lysosomal system: from acidification and cargo sorting to neurodegeneration. *Transl Neurodegener*. 2015; 4: 18.

20. Roche PA, Cresswell P. Antigen Processing and Presentation Mechanisms in Myeloid Cells. *Microbiol Spectr*. 2016; 4.

21. Joffre OP, Segura E, Savina A, Amigorena S. Cross-presentation by dendritic cells. *Nat Rev Immunol*. 2012; 12: 557–569.

22. Liu Z, Huang L, Xue W. pH-responsive vaccine delivery systems for improving cellular immunity. *Progress in Natural Science: Materials International*. 2020; 30: 609–617.

23. Stahl M, Holzinger J, Bülow S, Goepferich AM. Enzyme-triggered antigen release enhances cross-presentation by dendritic cells. *Nanomedicine*. 2022; 42: 102545.

24. Stefaniak AB, Guilmette RA, Day GA, Hoover MD, Breysse PN, Scripsick RC. Characterization of phagolysosomal simulant fluid for study of beryllium aerosol particle dissolution. *Toxicol In Vitro*. 2005; 19: 123–134.

25. Qian H, Wohl AR, Crow JT, Macosko CW, Hoye TR. A Strategy for Control of "Random" Copolymerization of Lactide and Glycolide: Application to Synthesis of PEG-b-PLGA Block Polymers Having Narrow Dispersity. *Macromolecules*. 2011; 44: 7132–7140.

26. Childs CE. The determination of polyethylene glycol in gamma globulin solutions. *Microchemical Journal*. 1975; 20: 190–192.

27. Abstiens K, Gregoritza M, Goepferich AM. Ligand Density and Linker Length are Critical Factors for Multivalent Nanoparticle-Receptor Interactions. *ACS Appl Mater Interfaces*. 2019; 11: 1311–1320.

28. Gholizadeh S, Kamps JAAM, Hennink WE, Kok RJ. PLGA-PEG nanoparticles for targeted delivery of the mTOR/PI3kinase inhibitor dactolisib to inflamed endothelium. *Int J Pharm*. 2018; 548: 747–758.

29. Wen C-Y, Tang M, Hu J, et al. Determination of the Absolute Number Concentration of Nanoparticles and the Active Affinity Sites on Their Surfaces. *Anal Chem*. 2016; 88: 10134–10142.

30. Ehlers E. *Kurzlehrbuch: Quantitative und instrumentelle pharmazeutische Analytik ; mit 42 Tabellen*. 10th ed. Stuttgart: Dt. Apotheker-Verl.; 2002.

31. Spicer CD, Jumeaux C, Gupta B, Stevens MM. Peptide and protein nanoparticle conjugates: versatile platforms for biomedical applications. *Chem Soc Rev*. 2018; 47: 3574–3620.

32. Hartl N, Adams F, Merkel OM. From adsorption to covalent bonding: Apolipoprotein E functionalization of polymeric nanoparticles for drug delivery across the blood-brain barrier. *Adv Ther (Weinh)*. 2021; 4.

33. Cox A, Vinciguerra D, Re F, et al. Protein-functionalized nanoparticles derived from end-functional polymers and polymer prodrugs for crossing the blood-brain barrier. *Eur J Pharm Biopharm*. 2019; 142: 70–82.

34. Chiarpotti MV, Longo GS, Del Pópolo MG. Nanoparticles modified with cell penetrating peptides: Assessing adsorption on membranes containing acidic lipids. *Colloids Surf B Biointerfaces*. 2021; 197: 111373.

35. Su Y-L, Hu S-H. Functional Nanoparticles for Tumor Penetration of Therapeutics. *Pharmaceutics*. 2018; 10.

36. Friedman AD, Claypool SE, Liu R. The smart targeting of nanoparticles. *Curr Pharm Des*. 2013; 19: 6315–6329.

37. Valetti S, Maione F, Mura S, et al. Peptide-functionalized nanoparticles for selective targeting of pancreatic tumor. *J Control Release*. 2014; 192: 29–39.

38. Lee C, Jeong J, Lee T, et al. Virus-mimetic polymer nanoparticles displaying hemagglutinin as an adjuvant-free influenza vaccine. *Biomaterials*. 2018; 183: 234–242.

39. Yang G, Chen S, Zhang J. Bioinspired and Biomimetic Nanotherapies for the Treatment of Infectious Diseases. *Front Pharmacol*. 2019; 10: 751.

40. Bachmann MF, Jennings GT. Vaccine delivery: A matter of size, geometry, kinetics and molecular patterns. *Nat Rev Immunol*. 2010; 10: 787–796.

41. Gao W, Chan JM, Farokhzad OC. pH-Responsive nanoparticles for drug delivery. *Mol Pharm*. 2010; 7: 1913–1920.

42. Hermanson GT. *Bioconjugate techniques*. Amsterdam: Academic Press; 2008.

43. Martínez-Jothar L, Doulkeridou S, Schiffelers RM, et al. Insights into maleimide-thiol conjugation chemistry: Conditions for efficient surface functionalization of nanoparticles for receptor targeting. *J Control Release*. 2018; 282: 101–109.

44. Yasuda S, Oshima H, Kinoshita M. Structural stability of proteins in aqueous and nonpolar environments. *J Chem Phys*. 2012; 137: 135103.

45. Vij N, Min T, Marasigan R, et al. Development of PEGylated PLGA nanoparticle for controlled and sustained drug delivery in cystic fibrosis. *J Nanobiotechnology*. 2010; 8: 22.

46. Sornay C, Vaur V, Wagner A, Chaubet G. An overview of chemo- and site-selectivity aspects in the chemical conjugation of proteins. *R Soc Open Sci*. 2022; 9: 211563.

47. Yoo J-W, Mitragotri S. Polymer particles that switch shape in response to a stimulus. *Proc Natl Acad Sci U S A*. 2010; 107: 11205–11210.

Chapter 5 – Supporting Information

pH-sensitive release of
click chemistry-conjugated proteins
from nanoparticles

1   Click reaction
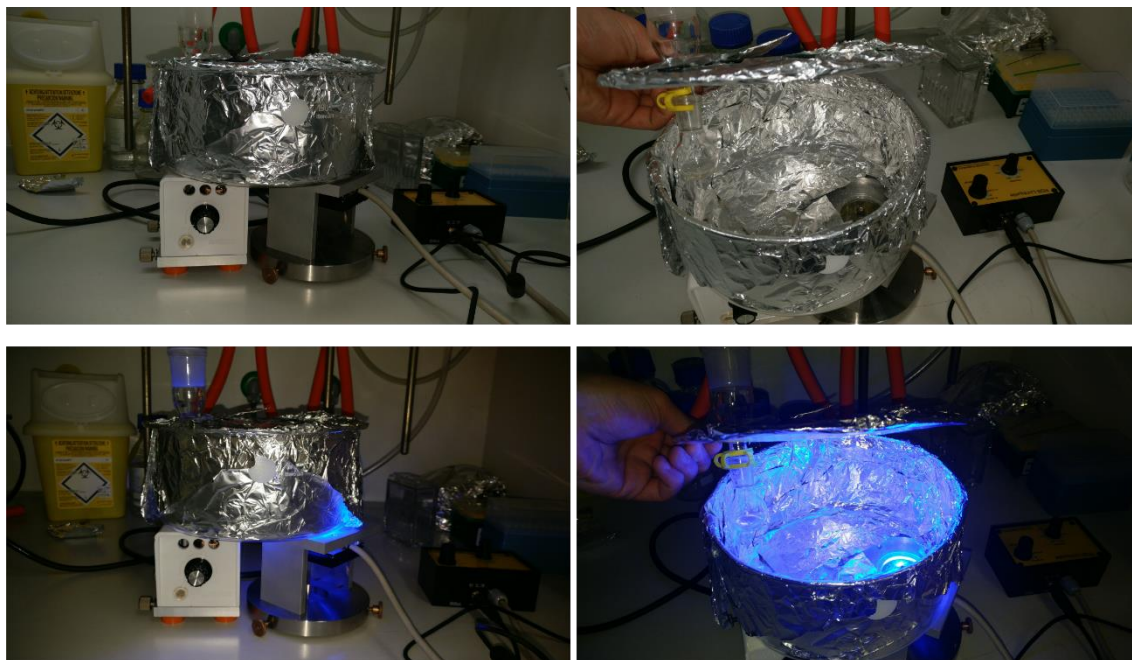
Figure S1. Experimental setup for click reaction.

2   Correlation of lamp irradiance and light intensity
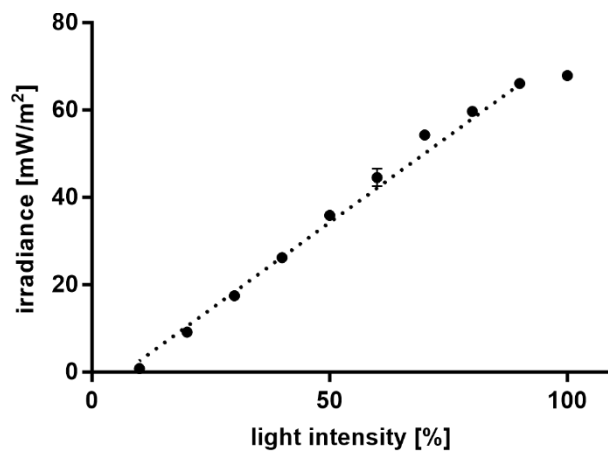
Figure S2. Correlation between the lamp irradiance determined with a radiometer and the light intensity set on the lamp with which the light bath for click reaction was generated. Results represent mean ± SD of n = 3 measurements.

3   Optimization of click reaction
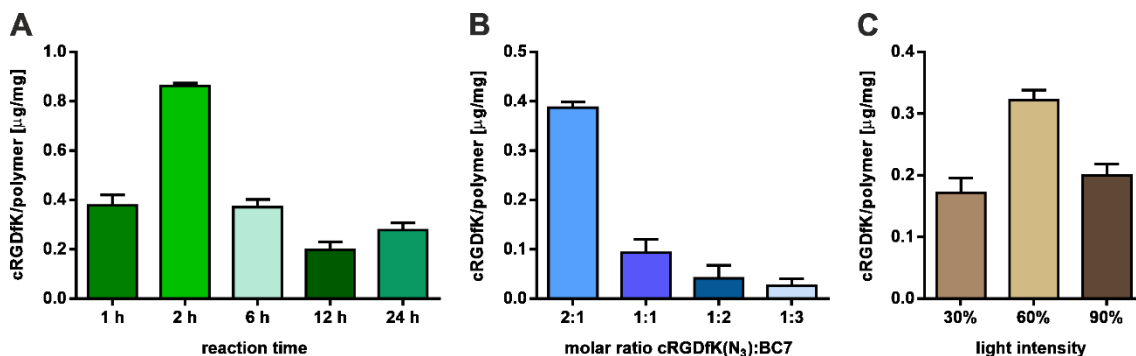
Figure S3. Optimization of click reaction. Amount of cRGDfK per mg polymer after reaction (A) at various reaction times, (B) with different molar ratios of cRGDfK(N_3) to BC7-PEG-PLGA and (C) varying light intensities. Results represent mean ± SD of n = 3 measurements.

4   Supplementary methods

4.1   Optimization of click reaction

In order to optimize the click reaction conditions to maximize coupling efficiency, cRGDfK(N_3) (Peptides International Inc., Louisville, KY, USA) was reacted with BC7-PEG-PGLA at different parameters. Basically, BC7-PEG-PLGA and cRGDfK(N_3) were dissolved in DMF and mixed with the photocatalyst Ir(p-CF_3-ppy)$_3$ (1.2 mol%). The reaction was initiated by irradiation with blue light in a light bath (Figure S1). After the reaction, the product was precipitated in diethyl ether and purified by dialysis against Millipore water using a 3.5 kDa molecular weight cut-off regenerated cellulose dialysis membrane (Spectrum Laboratories Inc., Rancho Dominguez, CA, USA) over 34 h. Different reaction times (1, 2, 6, 12, and 24 h), molar ratios of azide to BC7-PEG-PLGA (2:1, 1:1, 1:2, and 1:3) and light intensities (90, 60, and 30%) were tested to find optimal reaction conditions. Additionally, lamp irradiance was determined using an ILT1400 Portable Radiometer (International Light Technologies Inc., Peabody, MA, USA).

4.2   Quantification of cRGDfK

The level of cRGDfK conjugated to the polymer was assessed using a fluorescence assay previously described by Graf *et al.* [1]. For this purpose, polymers were dissolved in a mixture of ACN and ethanol (2:8 v/v). Polymer samples (100 µl) were mixed with

working solution (350 µl) consisting of 6 parts 9,10-phenanthrenequinone (150 µM in ethanol) and 1 part 2 N NaOH and incubated at 60 °C for 3 h. Afterwards, the samples (125 µl) were mixed with 1 N HCl (125 µl) and incubated for 1 h at room temperature with the exclusion of light. Fluorescence was measured at λ_{ex}=312 nm and λ_{em}=395 nm using a Synergy™ Neo2 Multi-Mode Microplate Reader (BioTek Instrument Inc., Winooski, VT, USA). Dilutions of cRGDfK (0-40 µg/ml; Synpeptide Co. Ltd., Shanghai, China) were used for calibration.

5 References

1. Graf N, Bielenberg DR, Kolishetti N, et al. α(V)β(3) integrin-targeted PLGA-PEG nanoparticles for enhanced anti-tumor efficacy of a Pt(IV) prodrug. *ACS Nano*. 2012; 6: 4530–4539.

[99m]Tc-labelled MeO-PEG-PLGA nanoparticles for sentinel lymph node imaging

Abstract

Sentinel lymph node (SLN) biopsy is one of the most frequently used diagnostic methods in everyday clinical work. SLN examination determines the choice of treatment in the therapy of many cancer diseases. Therefore, the need for good SLN detection agents with a high accuracy is enormous. [99mTc]Tc-Human serum albumin, [99mTc]Tc-sulfur colloids and [99mTc]Tc-tilmanocept are the most commonly used products at the moment, but they all have disadvantages such as time-consuming handling, poor detection accuracy due to wide size distribution, and high costs, respectively. The present study focused on the development of a new SLN detection agent based on polymeric nanoparticles to overcome the limitations of the currently used radiotracers. Methoxy-terminated poly(ethylene glycol)-poly(lactic-co-glycolic acid) (MeO-PEG-PLGA) nanoparticles were synthesized using microfluidics. We optimized the preparation parameters to finally obtain nanoparticles with a diameter between 10 and 50 nm – with the majority smaller than 30 nm – as these are ideal size characteristics for SLN imaging. Subsequent radioactive labelling with 99mTc was possible by a direct method without complexing agent. We evaluated optimal conditions for the labelling reaction in terms of stannous chloride amount and pH and finally obtained a product with 100% radiochemical purity. Overall, the developed [99mTc]Tc-MeO-PEG-PLGA nanoparticle system is an attractive alternative radiotracer that offers ideal size distribution, is not categorized as blood product, is inexpensive and, moreover, does not contain a chelating agent, thereby overcoming the major drawbacks of the current SLN detection agents.

1   Introduction

In case of breast and prostate carcinoma, skin tumors and many other types of cancer, the removal and histological examination of the first lymph nodes in the lymphatic drainage area of the primary tumor, the so-called sentinel lymph nodes (SLNs), is essential for precise diagnosis of the disease and correct choice of the therapy. SLN biopsy is used to investigate whether or not tumor cells are already present in the first lymph nodes, which in turn provides information about the metastatic stage of the tumor. The SLNs are localized and removed during surgery, often at the same time the primary tumor is removed. For this, a radiotracer – a radiolabelled colloid or macromolecule – is injected into the area surrounding the tumor, which then drains to the SLNs and is detected using a hand-held gamma probe. The ideal SLN detection agent has the following properties: 1) rapid clearance from injection site, 2) selective uptake into the lymphatic system and high retention in sentinel lymph nodes, 3) low uptake in distal lymph nodes, 4) easily detectable signal intensity and 5) biodegradation/elimination after signal detection [1, 2]. A radiotracer combining all these properties enables high accuracy of SLN detection with minimal surgical burden and gamma-ray exposure for patients and medical staff. Points 1) – 3) can be controlled by the size and size distribution of the radiotracer. Particles between 10 and 50 nm in size are perfect for SLN imaging as they rapidly leave the injection site and are taken up into the lymphatic system and then are strongly retained in the first lymph nodes. Particles larger than 50 nm remain at the injection site while smaller radiotracers (< 10 nm) continue to flow to distal lymph nodes [3]. Additionally to size, retention in the SLNs can also be increased by incorporating targeting ligands into the radiotracer. Point 4), the sufficient signal intensity, relies on a high labelling efficiency and can be achieved with the right labelling protocol and point 5), finally, depends on the material of the tracer.

Various radiotracers labelled with technetium-99m (^{99m}Tc) are currently used for SLN biopsy. ^{99m}Tc offers many advantages in terms of use in lymphoscintigraphy. The nuclide has a short half-life of 6.02 hours, is relatively cheap and readily available, shows low absorbed-dose burden to patients, and finally has almost no influence on the biochemical properties of the carrier [4]. [^{99m}Tc]Tc-sulfur colloid ([^{99m}Tc]Tc-SC), [^{99m}Tc]Tc-human serum albumin ([^{99m}Tc]Tc-HSA) and [^{99m}Tc]Tc-diethylenetriaminepentaacetic acid (DTPA)-mannosyl-dextran ([^{99m}Tc]Tc-tilmanocept) are the most commonly used diagnostic agents for SLN imaging at the moment [5].

However, each of them has disadvantages. For example, [⁹⁹ᵐTc]Tc-SCs show a wide size distribution with many large particles over 100 nm [6], making them unsuitable for SLN detection as they remain at the injection site. Therefore, the [⁹⁹ᵐTc]Tc-sulfur colloids are filtered after labelling to achieve the appropriate size und size distribution, but this in turn leads to the loss of a significant amount of radioactive label [7]. [⁹⁹ᵐTc]Tc-HSA is problematic due to its allergenic potential and its classification as a blood product, which implies time-consuming regulatory obligations such as patient information and batch documentation. Finally, [⁹⁹ᵐTc]Tc-tilmanocept is a very expensive radiotracer and DTPA is required as chelating agent to achieve sufficient labelling efficiency.

The use of polymeric NPs composed of block copolymer poly(ethylene glycol)-poly(lactic-co-glycolic acid) (PEG-PLGA) with a poly(lactic-co-glycolic acid) (PLGA)-stabilized core offers a promising alternative approach to the current radiotracers. PLGA and PEG are biocompatible polymers and already approved by the Food and Drug Administration (FDA) [8]. They are not categorized as blood products, making their handling significantly easier compared to [⁹⁹ᵐTc]Tc-HSA colloids. Furthermore, both polymers are completely eliminated from the body. PLGA is biodegraded in aqueous medium to lactic and glycolic acids, which are then further metabolized to carbon dioxide and water and eliminated through the kidneys. PEG, in turn, is excreted unchanged *via* the kidneys [9]. Moreover, using PEG-PLGA block copolymer as material for the NPs leads to a faster uptake into the lymphatic system and SLNs, since the PEG layer on the NP surface reduces interaction with the interstitium at the injection site [10]. Production of the NPs using microfluidics enables a controlled synthesis of the polymeric particles with a defined size and a narrow size distribution [11]. Microfluidic systems contain cartridges with microchannels. Due to their small dimensions, injected polymer solution and aqueous antisolvent are mixed very fast through diffusion resulting in supersaturation of the polymers, which in turn leads to nucleation and particle growth [12]. By using a microfluidic device for particle preparation, critical process steps such as mixing and supersaturation can be influenced by changing the total flow rate, the aqueous to organic solvent flow rate ratio, and the polymer concentration, thereby enabling precise control of NP size and polydispersity index (PDI) [13]. Additionally to the well controllable NP manufacturing, microfluidics offers a high batch-to-batch reproducibility and the possibility to easily scale-up the preparation which is advantageous for later clinical use [14, 15]. Thus, when preparing the carrier particles with a microfluidic device, NPs with a low PDI can be produced, overcoming the poor size distribution of [⁹⁹ᵐTc]Tc-sulfur colloids. Finally, He *et al.* have

demonstrated that PEG-PLGA NPs can be directly labelled with [99mTc] using stannous chloride as reducing agent without the need for a chelating agent [4]. This, in combination with the cheap raw materials, sets the alternative polymeric particulate radiotracer apart from [99mTc]Tc-tilmanocept.

The [99mTc]-labelling of the SLN detection agent with stannous chloride as reducing agent is a well-known and simple procedure. However, labelling efficiency highly depends on the reaction conditions. The pH of the reaction mixture and the amount of stannous chloride are the main factors determining completion of the reaction, i.e. no free technetium remains, as well as avoiding the formation of unwanted radiocolloids as by-product [16].

The goal of this study was to develop a particulate radiotracer based on polymeric NPs as an alternative to the existing SLN detection agents (Scheme 1). We prepared PEG-PLGA NPs with a PLGA-stabilized core using microfluidics and tested various process parameters to finally obtain small particles with a narrow size distribution that are ideally suited for SLN imaging. Additionally, we optimized [99mTc]-labelling of the particles by testing different stannous chloride amounts and pH values. Finally, the stability of the labelled product was tested by challenging with DTPA and cysteine.
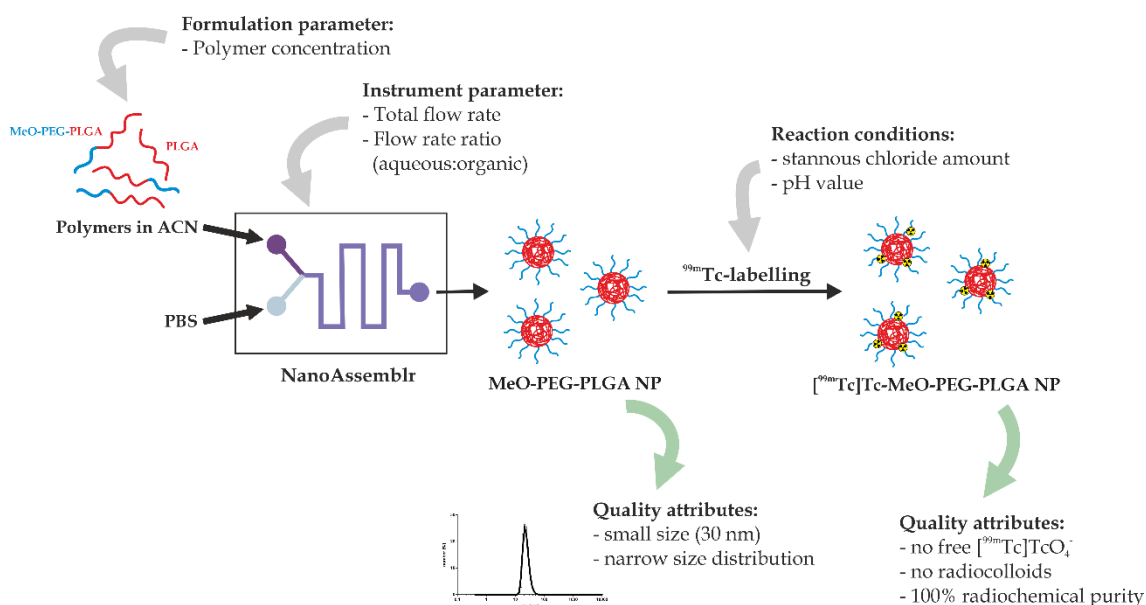
Scheme 1. Illustration of radiotracer development. MeO-PEG-PLGA NPs were prepared using microfluidics and subsequently [99mTc]-labelled by a direct method.

2 Materials and Methods

2.1 Materials

Methoxy-terminated poly(ethylene glycol)-poly(lactic-co-glycolic acid) (MeO-PEG$_{5k}$-PLGA$_{13k}$) with a PEG molecular weight of 5,065 Da and a PLGA molecular weight of 12,771 Da was synthesized by JenKem Technology USA Inc. (Allen, TX, USA). Acetonitrile (for DNA synthesis, max. 10 ppm H$_2$O) and stannous chloride dihydrate (SnCl$_2$·2H$_2$O) was obtained from Merck KGaA (Darmstadt, Germany). L-Cysteine hydrochloride monohydrate, diethylenetriaminepentaacetic acid (DTPA) and Gibco™ Dulbecco´s phosphate buffered saline (DPBS) were purchased from Thermo Fisher Scientific (Waltham, MA, USA). 0.9% saline and water for injection (WFI) were obtained from B. Braun (Melsungen, Germany). Expansorb® DLG 75-2A (PLGA) and all other materials and reagents were purchased from Sigma Aldrich (Taufkirchen, Germany).

2.2 NP preparation and characterization

NPs were prepared by microfluidics using the NanoAssemblr™ Benchtop (Precision NanoSystems Inc, Vancouver, Canada). NanoAssemblr™ controller software (v1.09) was used to control the process parameters. The organic phase containing MeO-PEG-PLGA and PLGA in acetonitrile (ACN) at a 7/3 mass ratio was injected into the first inlet port and DPBS as aqueous phase into the second inlet port of the instrument. In order to find optimal instrument and formulation parameters, different total flow rates (TFR), flow rate ratios (FRR) and polymer concentrations were tested. Their influence on particle size and PDI was checked by varying the TFR from 8 to 16 ml/min and FRR (aqueous:organic) from 10:1–1:1 at polymer concentrations of 10 and 20 mg/ml. NP solution was collected and hydrodynamic diameter as well as PDI of the freshly prepared undiluted samples were determined by dynamic light scattering (DLS) using a Malvern ZetaSizer Nano ZS (Malvern Instruments GmbH, Lappersdorf, Germany) with a 633 nm He-Ne laser (173° backscatter angle). Measurements were performed at 25 °C in disposable microcuvettes (Brand, Wertheim, Germany).

For all further experiments, NPs were prepared at a TFR of 16 ml/min and a FRR of 7:1 aqueous to organic phase with a polymer concentration of 20 mg/ml. 2 ml of the NP dispersion were collected in a 100 kDa molecular weight cut-off Microsep advance centrifugal device (Pall corporation, Port Washington, NY, USA) already containing 2

ml of DPBS. To remove the ACN, NPs were centrifuged in the 100 kDa molecular weight cut-off Microsep advance centrifugal device at 1000 g, then diluted with 4 ml DPBS and finally centrifuged again as before. Size and PDI were measured in DPBS (1 mg/ml) as described above.

NP mass concentration was determined as previously described [17]. In brief, PEG content in NPs was quantified using a colorimetric iodine complexing assay [18] and correlated with the exact particle mass determined through lyophilization. NP number concentration c_N was calculated assuming a spherical particle shape after equation 1 [19], where c_m is the particle mass concentration, ρ_{NP} is the density of the NPs (1.3 g/cm³) [20] and d_{NP} is the hydrodynamic diameter of the NPs measured by DLS.

$$c_N = \frac{c_m}{\rho_{NP} \cdot \frac{4}{3} \pi \left(\frac{d_{NP}}{2}\right)^3} \quad (1)$$

2.3 Sterile filtration

In order to test the sterile filterability of the particles prepared, NP dispersions were sterile filtered through a 0.2 µm Corning® PES syringe filter (Corning Inc., Corning, NY, USA). Particle size and PDI were determined before and after filtration using DLS as described above.

2.4 Colloidal stability at different pH values

Stability tests were performed to assess whether pH, that needs to be adjusted for labelling reaction, had any effect on colloidal stability of NPs. To this end, 450 µl of NPs (0.5 mg) were incubated with 450 µl of 0.9% saline and 100 µl of 10 mM HCl at pH 5, 6 or 7 (adjusted with 0.1N HCl, 1N HCl and 1N NaOH) to mimic later labelling reaction conditions. Afterwards, particle size distribution was determined by DLS as described above.

2.5 99mTc-labelling of NPs and optimization studies

MeO-PEG-PLGA NPs were radiolabelled with 99mTc by a direct method using stannous chloride as reducing agent. Briefly, 0.5 mg NPs (in 450 µl DPBS) were mixed with 0.1 N HCl, 1 N HCl or 1 N NaOH for pH adjustment. Afterwards, 450 µl of [99mTc]NaTcO₄

solution (0.49-1.01 GBq), eluted with 0.9% saline from a ^{99}Mo-^{99m}Tc generator (Ultra Technekow™ FM, Curium, Petten, Netherlands; Tekcis radionuclide generator, CIS Bio International, Saclay, France), was added to the NP dispersion. Finally, reaction was initiated by adding stannous chloride dihydrate. Labelling was carried out in a PYROVAC® vial (Acila AG, Weiterstadt, Germany) under argon atmosphere at room temperature for 1.5-3 h. To evaluate the effect of stannous chloride amount and pH on labelling efficiency, various amounts of $SnCl_2 \cdot 2H_2O$ (40, 120 and 200 µg) were tested at different pH values (5, 6 and 7). If not noted otherwise, reaction was performed with 200 µg $SnCl_2 \cdot 2H_2O$ at pH 5.

2.6 Determination of labelling efficiency

Labelling efficiency was assessed by ascending instant thin layer chromatography (ITLC). Two separate runs were performed for each reaction [21]: For the first run, 1 µl of the reaction mixture was spotted 1 cm above the bottom of a polysilica acid gel impregnated glass fiber sheet (ITLC-SA; Gelman Sciences Inc., Ann Arbor, MI, USA) and developed with methyl ethyl ketone (MEK) as mobile phase to determine free $[^{99m}Tc]TcO_4^-$. For run two, 1 µl of the reaction mixture was spotted 1 cm above the bottom of a silica gel coated glass microfiber chromatography paper (ITLC-SG, Agilent Technologies, Folsom, CA, USA) and developed with Acid-Citrate-Dextrose (ACD) solution (0.068 M citrate, 0.074 M dextrose, pH = 5) to determine hydrolyzed-reduced (H-R) ^{99m}Tc ($[^{99m}Tc]$Tc-Sn colloid and $[^{99m}Tc]TcO_2$). The radioactivity of the sheets was measured with a MiniGITA radiometric TLC scanner (Elysia-raytest GmbH, Straubenhardt, Germany). When using MEK as mobile phase, free $[^{99m}Tc]TcO_4^-$ migrated to the top of the ITLC strip and labelled NPs as well as radiocolloids (H-R ^{99m}Tc) remained at the application point. On the other hand, when using ACD solution, free $[^{99m}Tc]TcO_4^-$ and H-R ^{99m}Tc migrated with the solvent front, while labelled NPs remained at the beginning. Citric acid in the ACD solution is a weak complexing agent that can solubilize the radiocolloids, causing them to migrate with the mobile phase. However, the $[^{99m}Tc]$Tc-NP complexes are stronger and remain intact and are thus too large to migrate and therefore remain at the starting point [21]. The amount of free $[^{99m}Tc]TcO_4^-$ corresponds to the amount (%) migrated in MEK, the amount of radiocolloids was calculated by subtracting the percentage migrated in MEK from the percentage migrated in ACD. The amount of labelled NPs (= labelling efficiency) corresponds to the amount (%) not migrated in ACD.

2.7 DTPA and cysteine challenge

In order to check the binding strength of our NPs with [99mTc], the radiolabelled NPs were challenged with DTPA and cysteine. In short, solutions of 10 mM DTPA or 40 mM cysteine in WFI were prepared. 200 – 300 µl labelled NPs were mixed with 500 µl DTPA and cysteine solution, respectively. After 1.5-6 h incubation at room temperature, the effect of DTPA and cysteine on labelling efficiency was evaluated by ITLC with ACD solution as mobile phase, as described above. In this system, free $[^{99m}Tc]TcO_4^-$ and all known chemical forms of $[^{99m}Tc]Tc$-DPTA and $[^{99m}Tc]Tc$-cysteine migrated upward and labelled NPs remained at the point of application.

3 Results

3.1 Formulation optimization studies

For the manufacturing of our MeO-PEG-PLGA NPs, we used microfluidics. Polymers dissolved in ACN (organic phase) and DPBS (aqueous phase) were injected in the microfluidic cartridge of the NanoAssemblr™ Benchtop and the NP preparation was optimized by changing TFR, FRR and polymer concentration. As displayed in Figure 1, polymer concentration had minimal effect on particle size. The hydrodynamic diameter of the NPs was 32.0-45.5 nm at 10 mg/ml (Figure 1A) and 30.8-42.0 nm at 20 mg/ml (Figure 1B). A higher polymer concentration thus resulted in minimally smaller particles. Furthermore, the NPs prepared at 10 mg/ml showed a multimodal size distribution with aggregates in five approaches, while particles manufactured at 20 mg/ml always had a unimodal size distribution. This is also reflected in the higher PDI (0.037-0.199) for the lower concentration compared to the PDI of 0.025-0.104 for the higher concentration.

Regarding the different FRRs, a decrease in particle size with increasing aqueous fraction was detected at both polymer concentrations.

Finally, for almost all polymer concentration-FRR combinations, higher TFR resulted in smaller NPs. The batches produced at FRR 1:1 and 10 mg/ml showed an inverse correlation and also the particles prepared at polymer concentration 10 mg/ml, FRR 7:1 and TFR 16 ml/min were out of the line.

Since the approach synthesized at a polymer concentration of 20 mg/ml, a FRR of 7:1 and a TFR of 16 ml/min exhibited a small size (32.9±0.0 nm) and a narrow size

distribution (PDI 0.046±0.020) combined with a sufficient particle yield, we decided to use these parameters for future preparations.
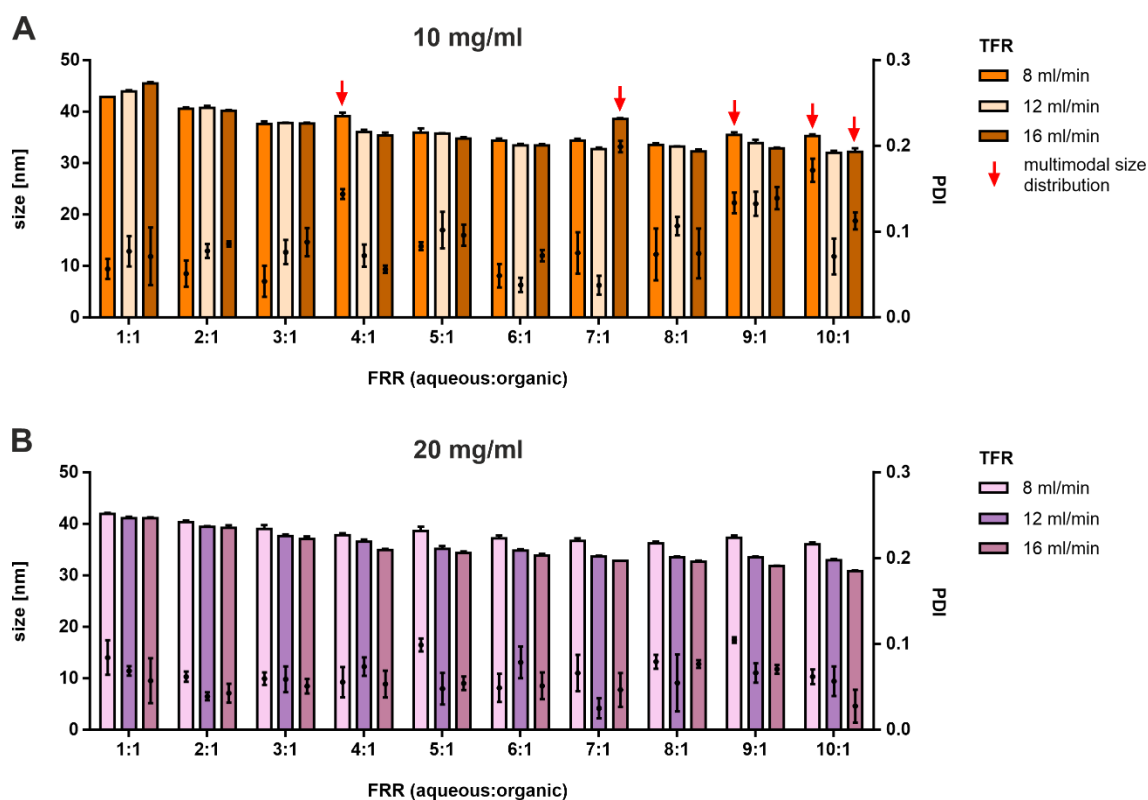
Figure 1. DLS measurements. Size and PDI of MeO-PEG-PLGA NPs prepared at an initial polymer concentration of either (A) 10 mg/ml or (B) 20 mg/ml using different total flow rates (TFR) and flow rate ratios (FRR). Red arrows indicate multimodal size distribution. Results represent mean ± SD of n = 3 measurements.

Next, we evaluated whether the washing procedure *via* ultracentrifugation affects particle size. DLS measurements of three batches revealed no changes in hydrodynamic diameter and a slight decrease in PDI after purification (Figure 2).
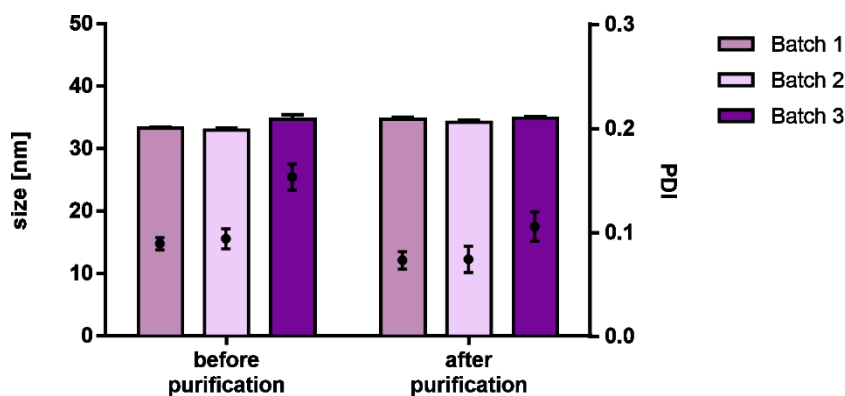
Figure 2. NP purification. Size and PDI of three batches of particles before and after purification *via* ultracentrifugation. Results represent mean ± SD of n = 3 measurements.

Finally, we investigated the sterile filterability of the NPs by determining the size and size distribution before and after filtration through a 0.2 µm PES filter. Figure 3 A-C shows that aggregates were removed by filtration and that the particles depicted no changes in size as the particle peaks of the size distribution curves were congruent. Additionally, the post-filtration NP size (S_f) relative to the pre-filtration NP size (S_i) was approximately 1.0 for all three batches, confirming that sterile filtration did not change size.
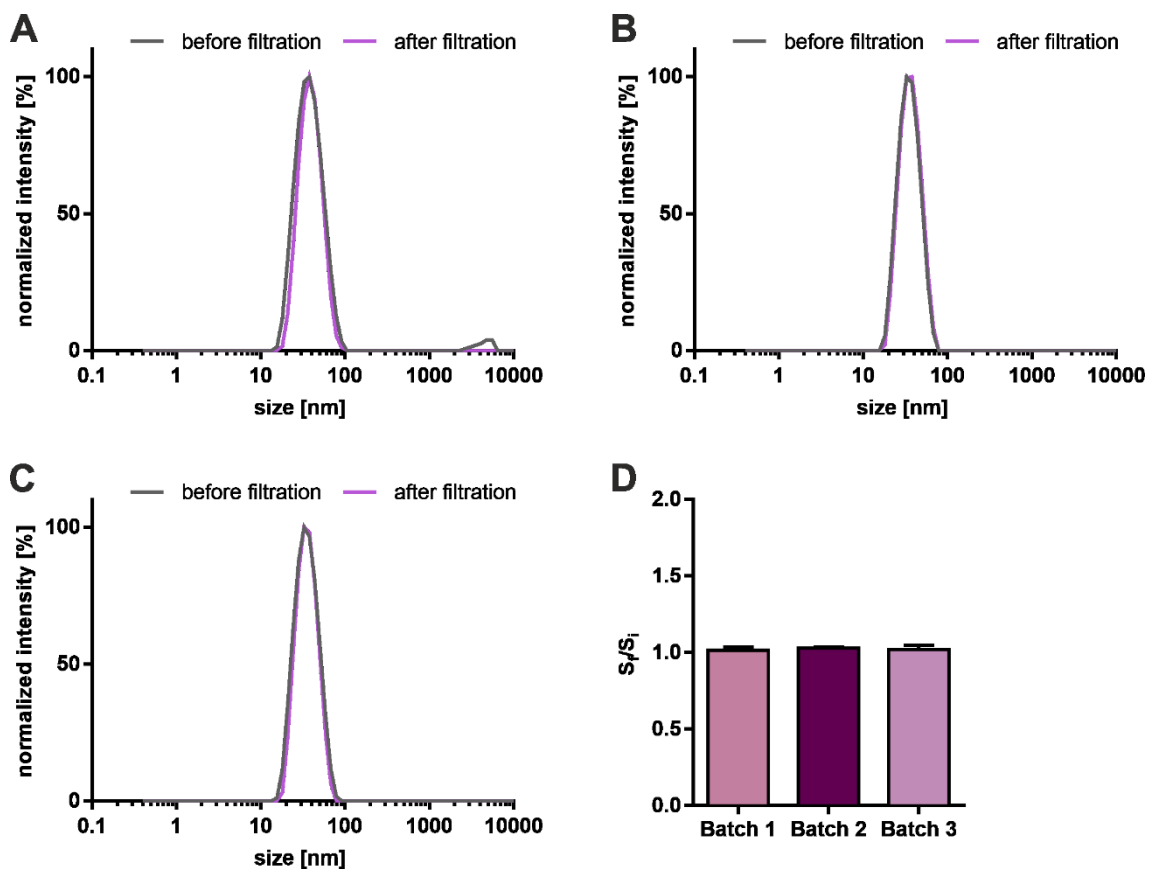
Figure 3. Sterile filterability of MeO-PEG-PLGA NPs. (A-C) Size distribution of NPs before and after sterile filtration. (D) Ratio of NP size after (S_f) and before (S_i) filtration of three batches. Results represent mean (A-C) or mean ± SD (D) of n = 3 measurements.

3.2 ^{99m}Tc-labelling optimization studies

We labelled MeO-PEG-PLGA NPs with ^{99m}Tc by a direct method using stannous chloride as reducing agent. Since the pH and the amount of stannous chloride strongly affect the formation of radiocolloids (H-R ^{99m}Tc) and the labelling efficiency, we tested various amounts of $SnCl_2 \cdot 2H_2O$ and different pH values. As shown in Table 1, free $[^{99m}Tc]TcO_4^-$ was only detectable at pH 7 in combination with the lowest stannous chloride amount (40 µg). No free pertechnetate was found for any of the other approaches.

Table 1. Influence of pH value and amount of stannous chloride on labelling efficiency. Results represent mean ± SD of n = 3 experiments.

	40 µg SnCl$_2$·2H$_2$O		
	%labelled NPs	%radiocolloids	%free [^{99m}Tc]TcO$_4^-$
pH 5	99.1 ± 1.3	0.9 ± 1.3	0.0 ± 0.0
pH 6	43.1 ± 25.6	56.9 ± 25.6	0.0 ± 0.0
pH 7	1.6 ± 0.8	96.8 ± 2.9	1.6 ± 2.3
	120 µg SnCl$_2$·2H$_2$O		
	%labelled NPs	%radiocolloids	%free [^{99m}Tc]TcO$_4^-$
pH 5	72.7 ± 19.5	27.3 ± 19.5	0.0 ± 0.0
pH 6	38.8 ± 40.3	61.2 ± 40.3	0.0 ± 0.0
pH 7	10.7 ± 7.4	89.3 ± 7.4	0.0 ± 0.0
	200 µg SnCl$_2$·2H$_2$O		
	%labelled NPs	%radiocolloids	%free [^{99m}Tc]TcO$_4^-$
pH 5	100.0 ± 0.0	0.0 ± 0.0	0.0 ± 0.0
pH 6	82.9 ± 18.2	17.1 ± 18.2	0.0 ± 0.0
pH 7	23.0 ± 20.7	77.0 ± 20.7	0.0 ± 0.0

Additionally, we saw that higher pH values and also lower amounts of SnCl$_2$·2H$_2$O led to the formation of more H-R ^{99m}Tc and thus poorer labelling efficiency (Table 1 and Figure 4). The optimum reaction conditions resulting in 100% radiochemical purity were found to be pH 5 and 200 µg stannous chloride dihydrate. Finally, pH stability tests revealed that our NPs showed the best stability at pH 5, since the ratio of NP size after and before treatment was unequal to 1.0 at pH 6 and 7, and also aggregates were detected in two batches at these pH values (Table S1 and Figure S2). At pH 5 the size ratio was 1.0 and no aggregates were visible in all three batches.
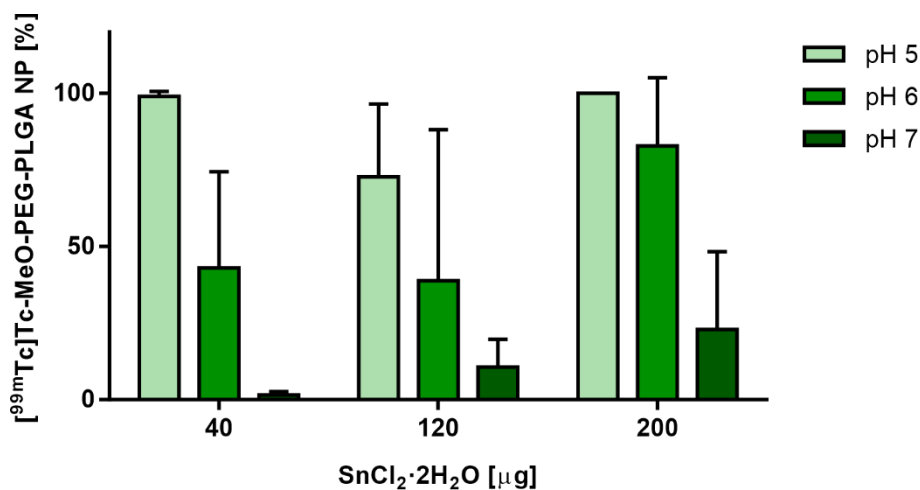
Figure 4. Amount of [^{99m}Tc]Tc-MeO-PEG-PLGA NPs after radiolabelling using 40, 120 or 200 µg stannous chloride dihydrate at pH 5, 6 or 7. Results represent mean ± SD of n = 3 experiments.

3.3 Stability of labelled NPs

To obtain information about the transchelation of our ^{99m}Tc-labelled NPs, which is a measure for the strength of the complex bond, we performed DTPA and cysteine challenge studies. As shown in Figure 5, cysteine did not alter much the labelling efficiency of the radiolabelled particles (1% transchelation). In the presence of DTPA, in turn, higher transchelation was observed (16%).
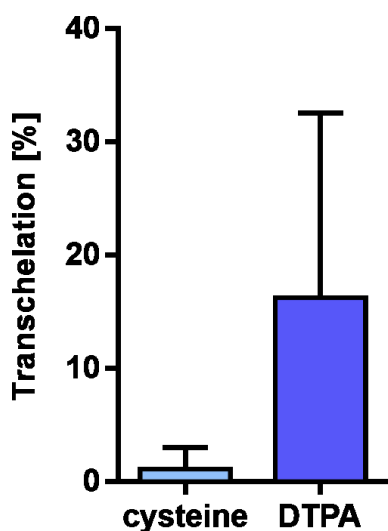
Figure 5. Effect of cysteine and DTPA on complex stability. Percentage of transchelation after challenge of [^{99m}Tc]Tc-PEG-PLGA NPs with 40 mM cysteine or 10 mM DTPA. Results represent mean ± SD of n = 3 experiments.

4   Discussion

SLN biopsy is the gold standard in diagnosis and therapy decisions for a variety of tumors [22]. In Germany alone, the number of probe-based SLN detections doubled between 2009 and 2015 [23]. Despite this immense need, the currently used and approved radiotracers have many disadvantages. For example, the [99mTc]Tc-HSA, most commonly used in Europe, is categorized as a blood product, which requires an immense effort in documentation and information. The [99mTc]Tc-sulfur colloids, which are approved in the USA, have a very wide size distribution, resulting in bad accuracy of SLN imaging [6]. Finally, the newest product [99mTc]Tc-Tilamanocept is perfect for imaging because with its size of 7 nm it drains very quickly from the injection site into the lymphatic system and due to the integrated mannose ligand it is strongly retained in the SLNs, however, it is extremely expensive and DTPA as a chelator is required [2, 24].

In this study, we developed a new radiotracer consisting of 99mTc-labelled MeO-PEG-PLGA NPs that is ideally suited for SLN biopsy and represents a promising alternative to currently approved detection agents. We manufactured particles with a mean diameter of about 33 nm and a narrow size distribution using microfluidics. Additionally, we optimized the labelling reaction with 99mTc in terms of stannous chloride amount and pH, resulting in a product with 100% radiochemical purity. Finally, we showed that the [99mTc]Tc-NP complex has good stability towards cysteine, which indicates very good complex stability *in vivo*.

We used MeO-PEG-PLGA block copolymer and PLGA as materials for our carrier NPs because they are excellently biocompatible, biodegradable, non-toxic [9] and moreover, they are not categorized as blood product. We prepared the NPs by nanoprecipitation using a microfluidic device (NanoAssemblr™ Benchtop). Additional PLGA was mixed with the PEG-PLGA polymers, forming a hydrophobic NP core to avoid disassembly in aqueous media [25]. Polymers dissolved in ACN, a water-miscible organic solvent, and DPBS as antisolvent were injected into the microfluidic cartridge. The small dimensions of the microchannels allowed rapid mixing of organic and aqueous phase through diffusion, resulting in reduced solubility and thus supersaturation of the polymers, whereupon they self-assemble into NPs. The particle formation process takes place in three stages (Scheme 2). First, single polymers form nuclei due to altered solubility after phase mixing. In the second stage, the nuclei grow through aggregation of further monomers to the nuclei. The final stage III is reached when NPs are sufficiently large and no more unimers can aggregate to the NPs since a polymer brush layer has formed

on the surface. The particles are kinetically locked. During the third stage, the NPs are in an equilibrium where only a slow exchange of single polymers occurs without any change in size. [11, 14, 26]
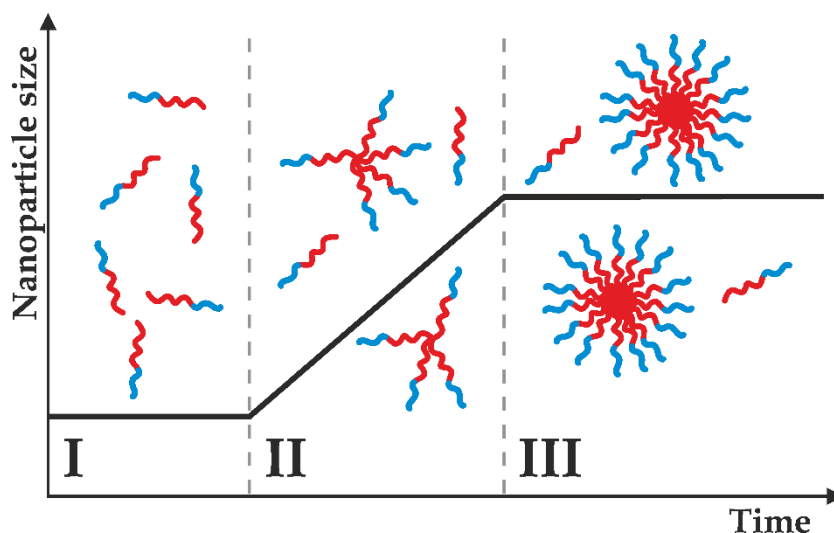
Scheme 2. Three stages of nanoprecipitation of MeO-PEG-PLGA NPs. Nucleation of monomers (stage I), followed by nuclei growth through aggregation of further polymers to the nuclei (stage II), resulting in kinetically locked NPs with slow exchange of monomers (stage III).

The final size of the NPs strongly depends on the mixing time of the organic and aqueous phases. The faster the mixing, the more homogenous the supersaturation of the polymers and the more polymer nuclei are formed initially, resulting in more and smaller NPs. Slower mixing, in turn, results in the local presence of higher levels of organic solvent, leading to poorer nucleation and hence growth of larger particles [14]. Additionally, the degree of supersaturation affects NP size. Higher supersaturation leads to smaller particles since more nuclei precipitate in stage I. On the other hand, at low supersaturation, less nuclei appear initially, increasing the final NP size [27].

In order to synthesize ideal carriers for SLN biopsy with small size and low polydispersity, we optimized particle preparation by changing instrument parameters such as TFR and FRR and testing different polymer concentrations. Generally, we observed a decrease in particle sizes with higher TFRs, consistent with the results of previous studies [11, 28, 29]. Total flow rate directly affects mixing time of organic and aqueous phases. Higher TFRs ensures faster mixing leading to smaller particles as discussed above. Furthermore, influence of FRR on NP size was detectable, as higher aqueous fraction resulted in smaller particles, which was also seen by others [27, 30].

With higher ratios of nonsolvent to solvent, polymer solubility in the final mixture decreases, resulting in a high supersaturation.

As already explained, high supersaturation leads to smaller particles. Furthermore, high organic solvent fraction facilitates the adsorption of polymers on the NP surface or their insertion into the particles, leading to an increase in size [11]. In contrast to previous studies [15, 31], that reported larger particle diameters at higher polymer concentrations, we observed an inverse trend with decreasing size at higher concentrations. We think, that the higher polymer concentration led to higher supersaturation and hence smaller particles. In addition, we saw an increase in PDI at lower concentrations, indicating that the low supersaturation led to secondary nucleation resulting in a broader size distribution [32, 33].

NPs prepared at polymer concentration of 20 mg/ml, FRR of 7:1 and TFR of 16 ml/min depicted the best properties in terms of size and PDI for later use as radiotracers. Their mean size was about 33 nm (Figure S1). Howard *et al.* showed that only PEG-PLGA NPs with a diameter below 33 nm are effectively drained to the lymph nodes [34]. Our particles therefore have ideal dimensions for SLN detection. The narrow size distribution, reflected in the PDI around 0.05, suggests high accuracy in SLN imaging. The particle sizes were between 13.5 and 58.8 nm, with 85% being below 30 nm. Thus, the NPs are not likely to drain to distal lymph nodes since they are larger than 10 nm, nor do they remain at the injection site or in the lymph ducts, but presumably accumulate rapidly in SLNs since the majority (99.5 %) is smaller than 50 nm [3].

Moreover, the unchanged particle size before and after ultracentrifugation showed that this purification method is suitable for our particles. The decrease in PDI suggests that remaining polymers and micelles were removed by washing.

Finally, we examined the sterile-filterability of our particles. For later clinical use, the NPs has to meet the pharmacopoeial sterility requirements. However, conventional sterilization by autoclaving, heat, gases or γ-irradiation is not possible for polymer NPs due to instability and toxicity aspects [35]. Our results showed that the particle size did not change through the filtration process. This indicates that filtration through a 0.22 μm membrane filter is well suited to sterilize these particles.

MeO-PEG-PLGA NPs were directly labelled with ^{99m}Tc using stannous chloride as reducing agent without the need for a chelating agent. [^{99m}Tc]TcO$_4^-$ was reduced from the heptavalent oxidation state to a lower valence state, which then formed a complex with carboxyl and carbonyl groups of PLGA in the NP core [36]. Efficiency of labelling reaction is strongly influenced by the amount of SnCl$_2$·2H$_2$O and the pH. Unsuitable

conditions lead to the formation of radiocolloids (H-R ^{99m}Tc) and residual free pertechnetate [16]. Free pertechnetate is problematic because, after s.c. administration, it distributes throughout the blood vessels and interstitium, thus reducing accuracy of SLN imaging [37]. Radiocolloids, on the other hand, are unwanted by-products as their size of 30–130 nm [38] negatively affects the narrow size distribution of our NPs and therefore the accuracy of SLN detection. By testing different stannous chloride amounts and pH values, we found optimal reaction conditions where neither free [^{99m}Tc]TcO$_4$⁻ nor radiocolloids were present. At pH 5 and 200 µg SnCl$_2$·2H$_2$O, radiochemical purity was 100%, which will most likely lead to very high accuracy in SLN biopsy. The successful labelling of polymeric NPs by a direct method has been previously reported by other groups [4, 7, 39]. However, none of them were able to optimize reaction to achieve 100% labelling efficiency. In case of the PLGA NPs developed by Subramanian *et al.* for SLN detection, integration of chelating agent was even necessary to obtain sufficient radiolabel [40]. Here our NPs are superior to the reported approaches as they can be easily ^{99m}Tc-labelled with maximum efficiency. Additionally, the excellent radiochemical purity allows it to be used without further purification, which is an advantage for the later clinical use.

The stability of the labelled NPs is of immense importance for later application, because *in vivo* decomposition negatively affects the biodistribution of radioactivity and thus the accuracy of SLN biopsy. Since thiols are ubiquitous in proteins, cysteines and glutathione, they are the main competing ligand for ^{99m}Tc *in vivo*. Thus, the lack of transchelation after cysteine challenge of the ^{99m}Tc-labelled NPs suggests good complex stability of our developed radiotracer in physiological environments. Transchelation after DTPA challenge is of minor importance as it only indicates that our complex is weaker than a [^{99m}Tc]Tc-DTPA complex. However, this is not surprising since DTPA is one of the most powerful complexing agents available [41].

5   Conclusion

In summary, our study is the first important step towards the development of a new SLN detection agent. We were able to develop polymeric NPs that were ideally sized for drainage in the lymph system and retention in SLNs and had a narrow size distribution promising high accuracy of SLN imaging. In addition, our protocol allows ^{99m}Tc-labelling without a chelating agent and with 100% radiochemical purity. The minimal

transchelation in the presence of cysteine suggests that the tracer is very stable *in vivo*. Further investigations, such as *in vivo* stability and distribution studies, have yet to be carried out. Apart from the advantages already mentioned, the MeO-PEG-PLGA NPs offer a number of other options for improving the handling and functionality of this new radiotracer. The polymer NPs can be easily lyophilized, which offers the possibility of developing a kit where the unlabelled carrier can be stored in its lyophilized form for a long time and radioactive labelling is carried out just before use. Moreover, a lymph node-targeting ligand can be integrated to further enhance SLN retention. In conclusion, the polymeric NPs developed here are a very promising SLN detection agent that could overcome all drawbacks of the current products.

References

1. Persico MG, Lodola L, Buroni FE, Morandotti M, Pallavicini P, Aprile C. (99m)Tc-human serum albumin nanocolloids: particle sizing and radioactivity distribution. *J Labelled Comp Radiopharm*. 2015; 58: 376–382.

2. Surasi DS, O'Malley J, Bhambhvani P. 99mTc-Tilmanocept: A Novel Molecular Agent for Lymphatic Mapping and Sentinel Lymph Node Localization. *J Nucl Med Technol*. 2015; 43: 87–91.

3. Soni KS, Desale SS, Bronich TK. Nanogels: An overview of properties, biomedical applications and obstacles to clinical translation. *J Control Release*. 2016; 240: 109–126.

4. He Z, Zhang X, Huang J, et al. Immune activity and biodistribution of polypeptide K237 and folic acid conjugated amphiphilic PEG-PLGA copolymer nanoparticles radiolabeled with 99mTc. *Oncotarget*. 2016; 7: 76635–76646.

5. Quartuccio N, Siracusa M, Pappalardo M, Arnone A, Arnone G. Sentinel Node Identification in Melanoma: Current Clinical Impact, New Emerging SPECT Radiotracers and Technological Advancements. An Update of the Last Decade. *Curr Radiopharm*. 2020; 13: 32–41.

6. Eshima S, Fauconnier T, Eshima L, Thornback JR. Radiopharmaceuticals for Lymphoscintigraphy: Including dusimetry and radiation considerations. *Seminars in Nuclear Medicine*. 2000; 30: 25–32.

7. Subramanian S, Dandekar P, Jain R, et al. Technetium-99m-labeled poly(DL-lactide-co-glycolide) nanoparticles as an alternative for sentinel lymph node imaging. *Cancer Biother Radiopharm*. 2010; 25: 637–644.

8. Jusu SM, Obayemi JD, Salifu AA, et al. Drug-encapsulated blend of PLGA-PEG microspheres: in vitro and in vivo study of the effects of localized/targeted drug delivery on the treatment of triple-negative breast cancer. *Sci Rep*. 2020; 10: 14188.

9. Locatelli E, Comes Franchini M. Biodegradable PLGA-b-PEG polymeric nanoparticles: synthesis, properties, and nanomedical applications as drug delivery system. *J Nanopart Res*. 2012; 14: 3582.

10. Singh I, Swami R, Khan W, Sistla R. Delivery Systems for Lymphatic Targeting. In: Domb AJ, Khan W, eds. *Focal Controlled Drug Delivery*. Boston, MA: Springer US; 2014: 429–458.

11. Karnik R, Gu F, Basto P, et al. Microfluidic platform for controlled synthesis of polymeric nanoparticles. *Nano Lett*. 2008; 8: 2906–2912.

12. Cruz-Acuña M, Kakwere H, Lewis JS. The roadmap to micro: Generation of micron-sized polymeric particles using a commercial microfluidic system. *J Biomed Mater Res A*. 2022; 110: 1121–1133.

13. Operti MC, Dölen Y, Keulen J, van Dinther EAW, Figdor CG, Tagit O. Microfluidics-Assisted Size Tuning and Biological Evaluation of PLGA Particles. *Pharmaceutics*. 2019; 11.

14. Mares AG, Pacassoni G, Marti JS, Pujals S, Albertazzi L. Formulation of tunable size PLGA-PEG nanoparticles for drug delivery using microfluidic technology. *PLoS ONE*. 2021; 16: e0251821.

15. Gdowski A, Johnson K, Shah S, Gryczynski I, Vishwanatha J, Ranjan A. Optimization and scale up of microfluidic nanolipomer production method for preclinical and potential clinical trials. *J Nanobiotechnology*. 2018; 16: 12.

16. Zolle I, ed. *Technetium-99m Pharmaceuticals: Preparation and Quality Control in Nuclear Medicine*. Berlin, Heidelberg: Springer Berlin Heidelberg; 2007.

17. Abstiens K, Gregoritza M, Goepferich AM. Ligand Density and Linker Length are Critical Factors for Multivalent Nanoparticle-Receptor Interactions. *ACS Appl Mater Interfaces*. 2019; 11: 1311–1320.

18. Childs CE. The determination of polyethylene glycol in gamma globulin solutions. *Microchemical Journal*. 1975; 20: 190–192.

19. Wen C-Y, Tang M, Hu J, et al. Determination of the Absolute Number Concentration of Nanoparticles and the Active Affinity Sites on Their Surfaces. *Anal Chem*. 2016; 88: 10134–10142.

20. Gholizadeh S, Kamps JAAM, Hennink WE, Kok RJ. PLGA-PEG nanoparticles for targeted delivery of the mTOR/PI3kinase inhibitor dactolisib to inflamed endothelium. *Int J Pharm*. 2018; 548: 747–758.

21. Ercan MT. Rapid determination of hydrolyzed-reduced technetium-99m in particulate radiopharmaceuticals. *International Journal of Radiation Applications and Instrumentation. Part A. Applied Radiation and Isotopes*. 1992; 43: 1175–1177.

22. Dogan NU, Dogan S, Favero G, Köhler C, Dursun P. The Basics of Sentinel Lymph Node Biopsy: Anatomical and Pathophysiological Considerations and Clinical Aspects. *J Oncol*. 2019; 2019: 3415630.

23. Hellwig D, Marienhagen J, Menhart K, Grosse J. Nuklearmedizin in Deutschland. Aktualisierte Kennzahlen und Trends aus offiziellen Statistiken. *Nuklearmedizin*. 2017; 56: 55–68.

24. Vera DR, Wallace AM, Hoh CK, Mattrey RF. A synthetic macromolecule for sentinel node detection: (99m)Tc-DTPA-mannosyl-dextran. *J Nucl Med*. 2001; 42: 951–959.

25. Owen SC, Chan DPY, Shoichet MS. Polymeric micelle stability. *Nano Today*. 2012; 7: 53–65.

26. Baby T, Liu Y, Middelberg APJ, Zhao C-X. Fundamental studies on throughput capacities of hydrodynamic flow-focusing microfluidics for producing monodisperse polymer nanoparticles. *Chemical Engineering Science*. 2017; 169: 128–139.

27. Bally F, Garg DK, Serra CA, et al. Improved size-tunable preparation of polymeric nanoparticles by microfluidic nanoprecipitation. *Polymer*. 2012; 53: 5045–5051.

28. Garg SM, Thomas A, Heuck G, et al. PLGA Nanoparticles: Tuning Particle Size Using The NanoAssemblr®Benchtop Instrument. Available at https://www.precisionnanosystems.com/docs/default-source/pni-files/app-notes/plga-particle-size-tuning-(pni-app-bt-008-ext)-e211de1b15aac4bc284d0873c4e09055c.pdf?sfvrsn=57dff234_0.

29. Amoyav B, Benny O. Controlled and tunable polymer particles' production using a single microfluidic device. *Appl Nanosci*. 2018; 8: 905–914.

30. Li X, Jiang X. Microfluidics for producing poly (lactic-co-glycolic acid)-based pharmaceutical nanoparticles. *Adv Drug Deliv Rev*. 2018; 128: 101–114.

31. Xu J, Zhang S, Machado A, et al. Controllable Microfluidic Production of Drug-Loaded PLGA Nanoparticles Using Partially Water-Miscible Mixed Solvent Microdroplets as a Precursor. *Sci Rep*. 2017; 7: 4794.

32. Pustulka KM, Wohl AR, Lee HS, et al. Flash nanoprecipitation: particle structure and stability. *Mol Pharm*. 2013; 10: 4367–4377.

33. Abstiens K, Goepferich AM. Microfluidic manufacturing improves polydispersity of multicomponent polymeric nanoparticles. *Journal of Drug Delivery Science and Technology*. 2019; 49: 433–439.

34. Howard GP, Verma G, Ke X, et al. Critical Size Limit of Biodegradable Nanoparticles for Enhanced Lymph Node Trafficking and Paracortex Penetration. *Nano Res*. 2019; 12: 837–844.

35. Konan YN, Gurny R, Allémann E. Preparation and characterization of sterile and freeze-dried sub-200 nm nanoparticles. *Int J Pharm*. 2002; 233: 239–252.

36. Psimadas D, Bouziotis P, Georgoulias P, Valotassiou V, Tsotakos T, Loudos G. Radiolabeling approaches of nanoparticles with (99m) Tc. *Contrast Media Mol Imaging*. 2013; 8: 333–339.

37. Ponto JA. Preparation and Dispensing Problems Associated with Technetium Tc-99m Radiopharmaceuticals. Available at https://pharmacyce.unm.edu/nuclear_program/freelessonfiles/vol11lesson1.pdf.

38. Zakir M, Sekine T, Takayama T, Kudo H, Lin M, Katsumura Y. Technetium (IV) Oxide Colloids and the Precursor Produced by Bremsstrahlung Irradiation of Aqueous Pertechnetate Solution. *J. Nucl. Radiochem. Sci*. 2005; 6: 243–247.

39. Yadav AK, Agarwal A, Rai G, et al. Development and characterization of hyaluronic acid decorated PLGA nanoparticles for delivery of 5-fluorouracil. *Drug Deliv*. 2010; 17: 561–572.

40. Subramanian S, Pandey U, Gugulothu D, Patravale V, Samuel G. Modification of PLGA nanoparticles for improved properties as a 99mTc-labeled agent in sentinel lymph node detection. *Cancer Biother Radiopharm*. 2013; 28: 598–606.

41. Eivazihollagh A. *Metal-chelate complexes in alkaline solution: On recovery techniques and cellulose-based hybrid material synthesis*. Sundsvall: Mid Sweden University; 2018.

Chapter 6 – Supporting Information

^{99m}Tc-labelled MeO-PEG-PLGA nanoparticles for sentinel lymph node imaging

1 NP preparation by microfluidics
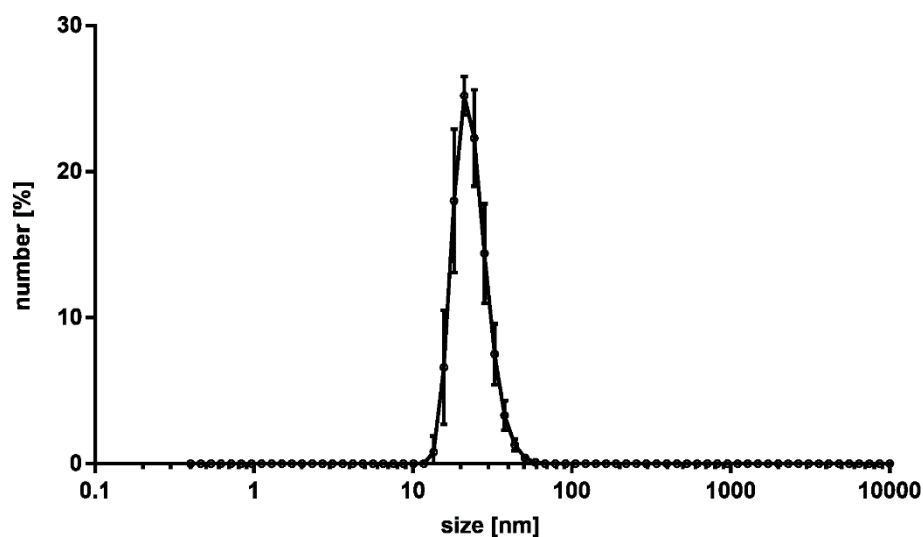
Figure S1. Number-weighted size distribution of MeO-PEG-PLGA NPs. NPs were prepared using microfluidics at a polymer concentration of 20 mg/ml, a FRR of 7:1 and a TFR of 16 ml/min (optimized parameters). Result represent mean ± SD of n = 3 NP batches.

2 pH stability of the NPs

Table S1. Determined pH in stability studies. Results represent mean ± SD of n = 3 experiments.

pH 5	pH 6	pH 7
5.09 ± 0.07	6.09 ± 0.02	6.90 ± 0.02
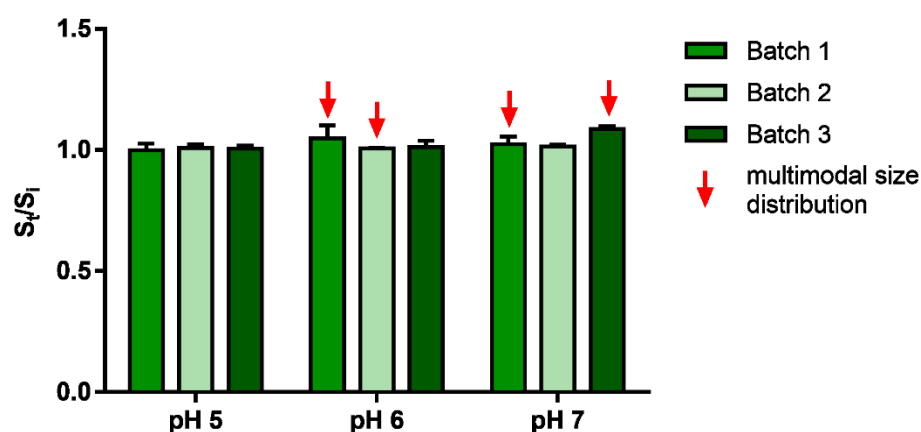
Figure S2. Colloidal stability of NPs at different pH values. Ratio of NP size after (S_t) and before (S_i) treatment at pH 5, 6 or 7 of three NP batches. Size changes are indicated by a ratio unequal to 1.0. Red arrows indicate multimodal size distribution. Results represent mean ± SD of n = 3 measurements.

3 ^{99m}Tc-labelling optimization studies

Table S2. Table S3. Determined pH in labelling experiments. Results represent mean ± SD of n = 3 experiments.

	40 µg $SnCl_2$	120 µg $SnCl_2$	200 µg $SnCl_2$
pH 5	5.15 ± 0.21	5.55 ± 0.29	4.71 ± 0.23
pH 6	6.11 ± 0.07	6.23 ± 0.11	5.99 ± 0.09
pH 7	6.86 ± 0.04	6.99 ± 0.06	6.85 ± 0.05

Chapter 7

Summary and Conclusion

1   Summary

Vaccines based on nanoparticles (NPs) show a number of advantages over classic vaccines such as killed whole organisms, live attenuated microorganisms or subunit vaccinations (**Chapter 1**). NP vaccines can induce both a cellular response (CD4$^+$ and CD8$^+$ T cell response) and a humoral immune response (B cell response with antibodies), while classic vaccines usually lack the cytotoxic CD8$^+$ T cell response. In addition, the NP-based vaccines have a defined and simple structure, giving them a better safety profile. And finally, their incredible variety of design strategies makes them very attractive. For example, nanoparticles can target dendritic cells (DCs) *via* their size or by integration of targeting ligands, they can act as self-adjuvants or adjuvants can be integrated, antigens can be protected from premature degradation *in vivo* by encapsulating in the core, and their pathogen-mimicking size and shape are ideal for immune activation. DC targeting vaccines with controlled intracellular trafficking have received increasing attention in recent years. Numerous design approaches have been explored that trigger a specific intracellular pathway of the NPs and incorporated antigen in DCs, thereby directing the mode of antigen presentation, i.e. MHC-I or MHC-II. The use of materials or linkers that are degradable in the early endosome to encapsulate or attach antigens to NPs enables antigen release in the early endosome and thus escape into the cytosol, which leads to a cytotoxic T cell response, while with stable NPs and linkers, antigen degradation occurs in the lysosome and leads to a CD4$^+$ T cell response. Although the few enzymes that are active in the slightly acidic environment in early endosomes of DCs provide a specific release mechanism for this compartment, finally leading to MHC-I presentation, no NP-based vaccines with enzyme-triggered antigen release have been developed to date.

The aim of this thesis was the development of an antigen delivery platform consisting of poly(ethylene glycol)-poly(lactic-co-glycolic acid) (PEG-PLGA) NPs, which releases their antigens in the early endosome of DCs and thus induces a cytotoxic T cell response due to antigen cross-presentation. For this purpose, acid and enzyme-cleavable motifs that were used for antigen release were integrated into the particle system.

First, the vaccine platform with the enzyme-cleavable linker was developed. Ovalbumin (OVA) as a model antigen was covalently conjugated to the PEG-PLGA NP surface *via* a peptide linker cleavable by early endosomal protease cathepsin S. A production method was developed where the antigen was exclusively covalently conjugated and no adsorbed OVA was present. Particle characterization showed ideal virus-sized

dimensions. Stability tests exhibited good storage stability in phosphate buffered saline at 4 °C and no aggregation in culture medium. Additionally, it was shown that the particles form a negligible protein corona after incubation in serum. Furthermore, a functionalization protocol for proteins was established allowing conjugation of any antigen to the developed particle system (**Chapter 3**).

In the next step, the antigen delivery platform was tested in cell experiments with DCs to examine whether the enzyme-triggered antigen release can enhance cross-presentation as postulated (**Chapter 4**). It was shown that the enzyme substrate used as linker is still cleavable by cathepsin S after integration into the NPs. Moreover, it was demonstrated that the particles are non-cytotoxic and internalized by DCs. Tracing the intracellular fate of the conjugated antigens in DCs revealed that OVA released from the particle system with the enzyme-cleavable linker was more located outside the endo-lysosomal compartments, while OVA on similar particles with a stable linker remained in the endosomes and lysosomes. Combined with the results that DCs stimulated with OVA NPs with cleavable linker activated CD8$^+$ T cells more than DCs stimulated with OVA NPs with a stable linker, it was hypothesized that the enzymatic release of the antigen in the early endosome resulted in endosomal escape and subsequent proteasomal degradation and MHC-I presentation.

Since the early endosome offers a slightly acidic environment, acid-triggered antigen release may also enable the transfer of released antigens from endosome to cytosol, thus enhancing cross-presentation. Visible light-induced copper-free click chemistry was used to integrate an acid-cleavable triazoline structure into the particle system consisting of polymeric core, peptide linker and ovalbumin (**Chapter 5**). The benzocycloheptene required for the click reaction was synthesized and extensively characterized by various analytical methods. Then the click reaction was optimized for the bioconjugation of the peptide linker to block copolymers and finally the release studies at different pH values revealed that the proteins are released in acidic environments. However, OVA was also released at neutral pH values. Therefore, further improvements are needed for this system.

In **Chapter 6**, an alternative radiotracer for sentinel lymph node diagnosis was developed that overcomes all disadvantages of the currently used detection agents. PEG-PLGA NPs were prepared using microfluidics and by optimizing process parameters such as total flow rate, flow rate ratio and polymer concentration, particles with diameters of 10-50 nm and the majority below 30 nm were produced, which is the ideal

size for sentinel lymph node biopsy. For radioactive labelling with ^{99m}Tc, a direct method with stannous chloride as reducing agent was used. Reaction conditions (pH and amount of stannous chloride) were optimized that finally ^{99m}Tc-labelled NPs with 100% radiochemical purity were obtained. Cysteine challenge tests indicated good complex stability *in vivo*.

2 Conclusion

In this work, two new promising nanoparticle systems were developed. The OVA NPs with enzyme-triggered antigen release offer great potential for use as T cell inducing vaccines against viral infections or cancer. Controlled production and comprehensive characterization enabled the development of an antigen release platform with a defined and known composition. It could be shown that an enzyme-triggered antigen release leads to endosomal escape in dendritic cells and consequently to an increased MHC-I presentation. The developed particle system was designed in such a way that individual components can be easily exchanged. This highly versatile system thus offers the possibility of using any antigens and linkers and thus opens it for use against a large number of pathogens and diseases. The second NP system developed, the [^{99m}Tc]Tc-PEG-PLGA NPs, represents a promising radiotracer for sentinel lymph node diagnostics. Due to the controllable production using microfluidics and the simple ^{99m}Tc-labelling without complexing agents, a very simple system could be created that could surpass all previously approved diagnostic agents.

Appendix

2-ME	2-Mercaptoethanol
7-AAD	7-Aminoactinomycin D
AA	acrylic acid
ACD	Acid-Citrate-Dextrose
ACN	Acetonitrile
ANOVA	Analysis of variance
APC	Allophycocyanin
APCs	Antigen presenting cells
ApoA4	Apolipoprotein A4
ApoH	Apolipoprotein H
BC7	Benzocycloheptene
BCA	Bicinchoninic acid
BMDCs	Bone marrow-derived dendritic cells
BSA	Bovine serum albumin
CatS	Cathepsin S
CatS subs	Cathepsin S substrate
CD	Cluster of differentiation
CDCl3	Deuterated chloroform
CLEC4K	C-type lectin domain family 4 member K
CLEC4L	C-type lectin domain family 4 member L
CLEC9A	C-type lectin domain family 9 member A
CLRs	C-type lectin receptors
CLSM	Confocal laser scanning microscopy
CpG	5'-Cytosine-phosphate-guanine-3'
cRGDfK	Cyclo[arginyl- glycyl- aspartyl- D-phenylalanyl- lysine]

cRGDfK(N$_3$)	Cyclo[arginyl- glycyl- aspartyl- D-phenylalanyl- azido-lysine]
CTG	CellTracker™ green
CVR	Conversion rate
d$_6$-DMSO	Deuterated dimethyl sulfoxide
Dabcyl-GRKWPPMGLPWEC-DArg-Glu(EDANS)	N-[4-[[4-(Dimethylamino)phenyl]azo]benzoyl]- glycyl-arginyl- lysyl- tryptophyl- prolyl- prolyl- methionyl-glycyl- leucyl- prolyl- tryptophyl- glutamyl- cysteinyl- D-arginyl- N-[2-[(5-sulfo-1-naphthalenyl)amino]ethyl]-glutamic amide
DAPI	4′,6-Diamidine-2′-phenylindole dihydrochloride
DBU	1,8-Diazabicyclo[5.4.0]undec-7-ene
DCM	Dichloromethane
DCs	Dendritic cells
DC-SIGN	Dendritic cell-specific intercellular adhesion molecule-3-grabbing non-integrin
DIPEA	N,N-Diisopropylethylamine
DLS	Dynamic light scattering
DMF	N,N-Dimethylformamide
DNA	Deoxyribonucleic acid
DNGR-1	Dendritic cell natural killer lectin group receptor-1
DPBS	Dulbecco´s phosphate buffered saline
DTNB	5,5-Dithio-bis-(2-nitrobenzoic acid)
DTPA	Diethylenetriaminepentaacetic acid
DTT	Dithiothreitol
EDC	Ethyl-3-(3-dimethylaminopropyl)carbodiimide
EDTA	Ethylenediaminetetraacetic acid
EEA1	Early endosome antigen 1
EtOAc	Ethyl acetate
EtOH	Ethanol
FACS	Fluorescence-activated cell sorting

FCS	Fetal calf serum
FDA	Food and Drug Administration
FITC	Fluorescein isothiocyanate
FRET	Fluorescence resonance energy transfer
FRR	Flow rate ratio
GA	glycolic unit
GRKWPLPWPMGEC-DArg-NH2	Glycyl- arginyl- lysyl- tryptophyl- prolyl- leucyl- prolyl- tryptophyl- prolyl- methionyl- glycyl- glutamyl- cysteinyl- D-arginine amide
GRKWPPMGLPWEC-DArg-NH$_2$	Glycyl- arginyl- lysyl- tryptophyl- prolyl- prolyl- methionyl- glycyl- leucyl- prolyl- tryptophyl- glutamyl- cysteinyl- D-arginine amide
GR-Lys(N$_3$)-WPPMGLPWEC-DArg-NH$_2$	Glycyl- arginyl- azido-lysyl- tryptophyl- prolyl- prolyl- methionyl- glycyl- leucyl- prolyl- tryptophyl- glutamyl- cysteinyl- D-arginine amide
HA	Hyaluronic acid
H-NMR	Proton nuclear magnetic resonance
HOOC-PEG-OH	Acid-terminated poly(ethylene glycol)
HPLC	High-performance liquid chromatography
HPV	Human papilloma virus
HSA	Human serum albumin
IgG	Immunoglobulin G
IgM	Immunoglobulin M
Ii	Invariant chain
IR	Infrared
ITLC	Instant thin layer chromatography
KLH	Keyhole limpet hemocyanin
LA	lactic unit
LAF	Laminar air flow
LED	Light emitting diode
LNs	Lymph nodes

LPS	Lipopolysaccharide
LTG	LysoTracker™ green
LT-PBS	Low-endotoxin Dulbecco's phosphate-buffered saline
Mal	Maleimide
Mca-GRWPPMGLPWE-Lys(Dnp)-DArg-NH2	(7-Methoxycoumarin-4-yl)acetyl- glycyl- arginyl- tryptophyl- prolyl- prolyl- methionyl- glycyl- leucyl- prolyl- tryptophyl- glutamyl- [Nε– (2,4-dinitrophenyl)-L-lysyl]- D-arginine amide
MEK	Methyl ethyl ketone
MGL	Macrophage galactose-type lectin
MHC	Major histocompatibility complex
MPL	Monophosphoryl lipid A
MR	Mannose receptor
MWCO	Molecular weight cut-off
N_A	Avogadro number
NADPH	Nicotinamide adenine dinucleotide phosphate
NHS	N-Hydroxysuccinimide
NPs	Nanoparticles
ODN	Oligodeoxynucleotide
OVA	Ovalbumin
PDI	Polydispersity index
PEG	polyethylene glycol
PEG-PLGA	Poly(ethylene glycol)-poly(lactic-co-glycolic acid)
PEI	polyethyleneimine
PES	Polyethersulfone
PFA	Paraformaldehyde
PGA	Polyglycolic acid
PLA	Polylactic acid
PLGA	Poly(lactic-co-glycolic acid)
ppm	Parts per million

PPS	Polypropylene sulfide
PRRs	Pattern recognition receptors
PS	Polystyrene
P-S	Penicillin-streptomycin
PSF	Phagolysosomal simulant fluid
RNA	Ribonucleic acid
R_T	Retention times
SC	Sulfur colloid
SD	Standard deviation
SDS-PAGE	Sodium dodecyl sulfate polyacrylamide gel electrophoresis
SEC	Size exclusion chromatography
SLN	Sentinel lymph node
SR	Scavenger receptor
stL	stable linker
Sulfo-SMCC	Sulfosuccinimidyl 4-[N-maleimidomethyl]cyclohexane-1-carboxylate
TCEP	Tris(2-carboxyethyl)phosphine
TFR	Total flow rate
THF	Tetrahydrofuran
TLRs	Toll like receptors
T_m	Melting point
UV	Ultraviolet
V-ATPase	Vacuolar adenosine triphosphatase
WHO	World Health Organization
XCR1	X-C motif chemokine receptor 1

Curriculum Vitae

Name:	Monika Christine Juliane Stahl
Date of birth:	22th of July 1994
Place of birth:	Weiden i. d. Opf. (Germany)
Nationality:	German

Scientific education and work experience

since 05/2022	**Pharmacist** NM Vital Apotheke, Neumarkt i. d. Opf.
01/2018 – 02/2022	**PhD Candidate/Research Assistant** Department of Pharmaceutical Technology University of Regensburg
01/2018 – 02/2022	**Structured doctorate program** Graduate school ChemPharm Faculty of Chemistry and Pharmacy University of Regensburg
12/2017	**Licensure as Pharmacist**
05/2017 – 10/2017	**Practical Training** Haupt Pharma Amareg GmbH, Regensburg
11/2016 – 04/2017	**Practical Training** Paracelsus Apotheke, Weiden i. d. Opf.
10/2012 – 10/2016	**Study of Pharmacy** Friedrich-Alexander-Universität, Erlangen-Nürnberg

School education

06/2012	**Abitur/A levels**
09/2004 – 06/2012	**Grammar School** Kepler-Gymnasium, Weiden i. d. Opf.

Peer-reviewed publications

1. <u>Stahl Monika</u>, Holzinger Jonas, Bülow Sigrid and Goepferich Achim. Enzyme-triggered antigen release enhances cross-presentation by dendritic cells. *Nanomedicine: Nanotechnology, Biology, and Medicine* 2022, 42, 102545 (**Chapter 4**)

Conference abstracts

1. <u>Stahl Monika,</u> Goepferich Achim. Visible-Light-Induced Click Chemistry for Nanoparticle Modification. *World Meeting on Pharmaceutics, Biopharmaceutics and Pharmaceutical Technology*, Virtual Meeting, 2021

2. <u>Stahl Monika,</u> Goepferich Achim. Polymer nanoparticles for delivering a model antigen to dendritic cells. *European and Global CLINAM-Summit*, Virtual Meeting, 2020

Acknowledgments

Declaration in lieu of an oath

I hereby declare that I have completed the dissertation presented without the impermissible help of third parties, without the use of resources other than those indicated, and that any data and concepts stemming directly or indirectly from other sources are indicated with citations to the literature.

No further persons were involved with the creation of the contents of the dissertation presented. In particular, I have not made use of the assistance of a doctoral consultant or other person in return for payment. No-one has received payment in kind either directly or indirectly for work which is associated with the content of the dissertation submitted.

The dissertation has not been submitted in the same or similar form to another examining authority, neither in Germany nor abroad.

Regensburg, 31.08.2022   _____

(Monika Stahl)